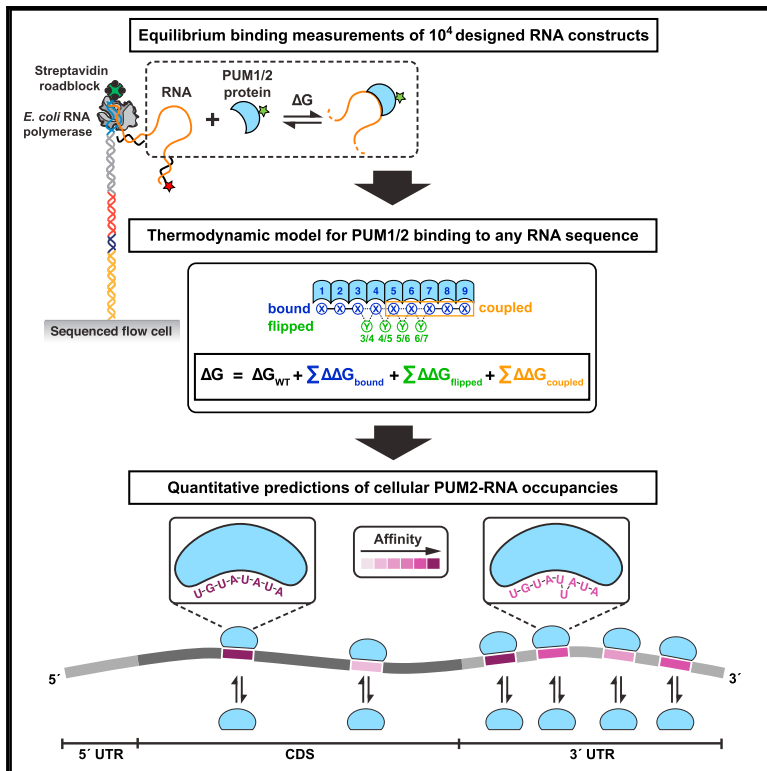


# Molecular Cell

## A Quantitative and Predictive Model for RNA Binding by Human Pumilio Proteins

### Graphical Abstract



### Authors

Inga Jarmoskaite, Sarah K. Denny, Pavanapuresan P. Vaidyanathan, ..., Rhiju Das, William J. Greenleaf, Daniel Herschlag

### Correspondence

wjg@stanford.edu (W.J.G.), herschla@stanford.edu (D.H.)

### In Brief

As RNA-binding proteins play key roles in cellular regulation, quantitative approaches are needed to capture RNA-protein interaction landscapes. Jarmoskaite et al. establish a quantitative model that predicts human PUM1/2 protein-RNA affinities and cellular PUM2-RNA occupancies, suggesting a continuous binding landscape negligibly affected by RNA structure and kinetic factors.

### Highlights

- A thermodynamic model quantitatively predicts PUM1/2 binding to any RNA sequence
- Factors beyond simple recognition of consecutive residues influence binding
- Comparison to X-linking data reveals thermodynamic control of PUM2 binding in cells
- Analysis of RNA structure effects suggests disruption of RNA structure in cells



# A Quantitative and Predictive Model for RNA Binding by Human Pumilio Proteins

Inga Jarmoskaite,<sup>1,14</sup> Sarah K. Denny,<sup>2,10,14</sup> Pavanapuresan P. Vaidyanathan,<sup>1,11,14</sup> Winston R. Becker,<sup>2,14</sup> Johan O.L. Andreasson,<sup>3,12</sup> Curtis J. Layton,<sup>3</sup> Kalli Kappel,<sup>2</sup> Varun Shivashankar,<sup>4</sup> Raashi Sreenivasan,<sup>1,13</sup> Rhiju Das,<sup>1</sup> William J. Greenleaf,<sup>3,5,6,\*</sup> and Daniel Herschlag<sup>1,7,8,9,15,\*</sup>

<sup>1</sup>Department of Biochemistry, Stanford University School of Medicine, Stanford, CA 94305, USA

<sup>2</sup>Biophysics Program, Stanford University School of Medicine, Stanford, CA 94305, USA

<sup>3</sup>Department of Genetics, Stanford University School of Medicine, Stanford, CA 94305, USA

<sup>4</sup>Novartis Institutes for BioMedical Research, Cambridge, MA 02139, USA

<sup>5</sup>Department of Applied Physics, Stanford University, Stanford, CA 94305, USA

<sup>6</sup>Chan Zuckerberg Biohub, San Francisco, CA 94158, USA

<sup>7</sup>Department of Chemistry, Stanford University, Stanford, CA 94305, USA

<sup>8</sup>Department of Chemical Engineering, Stanford University, Stanford, CA 94305, USA

<sup>9</sup>ChEM-H Institute, Stanford University, Stanford, CA 94305, USA

<sup>10</sup>Scribe Therapeutics, Berkeley, CA, 94704, USA

<sup>11</sup>Present address: Clear Labs, Menlo Park, CA 94025, USA

<sup>12</sup>Present address: Airity Technologies, Inc., Redwood City, CA 94061, USA

<sup>13</sup>Present address: FLX Bio, Inc., South San Francisco, CA 94080, USA

<sup>14</sup>These authors contributed equally

<sup>15</sup>Lead Contact

\*Correspondence: [wjg@stanford.edu](mailto:wjg@stanford.edu) (W.J.G.), [herschla@stanford.edu](mailto:herschla@stanford.edu) (D.H.)

<https://doi.org/10.1016/j.molcel.2019.04.012>

## SUMMARY

High-throughput methodologies have enabled routine generation of RNA target sets and sequence motifs for RNA-binding proteins (RBPs). Nevertheless, quantitative approaches are needed to capture the landscape of RNA-RBP interactions responsible for cellular regulation. We have used the RNA-MaP platform to directly measure equilibrium binding for thousands of designed RNAs and to construct a predictive model for RNA recognition by the human Pumilio proteins PUM1 and PUM2. Despite prior findings of linear sequence motifs, our measurements revealed widespread residue flipping and instances of positional coupling. Application of our thermodynamic model to published *in vivo* crosslinking data reveals quantitative agreement between predicted affinities and *in vivo* occupancies. Our analyses suggest a thermodynamically driven, continuous Pumilio-binding landscape that is negligibly affected by RNA structure or kinetic factors, such as displacement by ribosomes. This work provides a quantitative foundation for dissecting the cellular behavior of RBPs and cellular features that impact their occupancies.

## INTRODUCTION

A grand challenge in biology is to understand, predict, and ultimately control gene expression programs that allow cells to

function. RNA processing is central to regulation of gene expression, and each processing step, from splicing and end-processing to translation and decay, is regulated by a suite of RNA-binding proteins (RBPs), which constitute >5% of the eukaryotic proteome (Mitchell and Parker, 2014; Müller-McNicoll and Neugebauer, 2013; Singh et al., 2015). By binding specific sequence or structure elements, RBPs can provide coordinated regulation of sets of functionally related RNAs, as shown, for example, for iron regulatory proteins, PUF (Pumilio and FBF) proteins, and the Nova RBP (Gerber et al., 2004; Keene and Tenenbaum, 2002; Rouault, 2006; Ule et al., 2003).

Given the central importance of RBPs, defining and predicting RBP interactions has been a major research focus, and transcriptome-wide RNA target sets have been identified for hundreds of RBPs, facilitating elucidation of RBP roles in regulatory processes (e.g., Darnell, 2010; Dominguez et al., 2018; Gerber et al., 2004; Hogan et al., 2008; Ray et al., 2013; Ule et al., 2003; Wheeler et al., 2018; Xue et al., 2009). While the RNA target databases provide immense value, several critical limitations to our current knowledge remain.

First, RBP targets are commonly defined in a binary manner, with RNA molecules considered either “targets” or “non-targets” of a given RBP. However, binding is a continuum, determined by RBP affinities, RBP and target concentrations, and other cellular factors. Therefore, quantitative affinity measurements are needed to define and predict RBP binding occupancies across the RNA sequences present in a cell—i.e., the RBP binding landscape—and the subsequent regulation. A second limitation is that most current approaches are optimized for identifying RBP targets rather than for quantitative determination of RBP affinities or occupancies. Third, current models of RBP specificity are limited to short, linear sequence logos and motifs,



which assume energetic additivity (Schneider and Stephens, 1990; Stormo, 2000). Yet, the accuracy of such models remains to be quantitatively and comprehensively tested.

The above limitations and the importance of regulation by RBPs have sparked a growing interest in developing quantitative genomic-scale approaches for measuring RBP-RNA interactions and affinities. Methods such as MITOMI (mechanically induced trapping of molecular interactions), HiTS-EQ (high-throughput sequencing equilibrium), HiTS-RAP (high-throughput sequencing–RNA affinity profiling), RNA Bind-n-Seq, and RNA-MaP (RNA on a massively parallel array) can provide equilibrium binding constants or apparent affinities (Buenrostro et al., 2014; Jain et al., 2017; Jankowsky and Harris, 2017; Lambert et al., 2014; Martin et al., 2012; Tome et al., 2014). Of these, RNA-MaP and HiTS-RAP, two related techniques that utilize a modified sequencing platform and an array of  $\sim 10^5$  unique immobilized RNA species, eliminate an intermediate capture step that can alter binding occupancies, thereby allowing highly accurate direct thermodynamic and kinetic binding measurements via fluorescence readout (Buenrostro et al., 2014; Tome et al., 2014 and *vide infra*). Recent studies have demonstrated the utility of RNA-MaP for systematic investigation of RNA-protein and RNA-RNA interactions and for generation of quantitative thermodynamic models (Buenrostro et al., 2014; Denny et al., 2018; She et al., 2017).

We used the RNA-MaP platform to interrogate the sequence preferences of the human PUF family proteins PUM1 and PUM2 across a diverse designed RNA library. PUF family proteins (Figure 1A) are universal in eukaryotes and have been implicated in regulation of mRNA turnover, transport, translation, and localization; in mammals, PUF proteins play important roles in brain and germline development, regulation of innate immunity, and other processes (Goldstrohm et al., 2018; Miller and Olivas, 2011). Extensive prior biochemical, structural, evolutionary, and *in vivo* studies of PUF proteins provide a powerful starting point for our quantitative and systematic dissection of specificity (Figure S1A and references therein) and allow us to pose specific biological, engineering, and biophysical questions.

PUF proteins have a modular structure of eight conserved tandem repeats that recognize RNA in a sequence-specific manner (Figure 1A), and this modularity provides a best-case scenario for building a simple predictive thermodynamic binding model (Wang et al., 2002). However, we show that the simplest, energetically additive model breaks down and that tight-binding RNA sequences exist that are not represented by previously defined motifs. Our large, quantitative RNA-MaP dataset enabled the generation of a predictive model for PUM1 and PUM2 binding that includes residue flipping and coupling terms. The model can also be applied to an engineered PUM1 variant, after changing a single parameter to account for the local specificity change. Remarkably, our *in-vitro*-derived binding model quantitatively explains median *in vivo* occupancies in prior PUM2 crosslinking data, demonstrating that RNA binding sites *in vivo* exhibit, on average, thermodynamically driven occupancies (Van Nostrand et al., 2016). Further analysis indicates that predicted RNA secondary structures do not lead to decreased PUM2 occupancy *in vivo*, suggesting that these structures are strongly disfavored in cells. Our thermodynamic

model provides a quantitative foundation for dissecting the cellular behavior of RBPs and represents a step toward a quantitative and predictive understanding of the complex networks of RBP-RNA interactions and their regulatory consequences.

## RESULTS

### Library Design

Starting with the PUM2 consensus motif, which has been determined by pull-down, cross-linking, and *in vitro* selection experiments (Figures 1A and S1A), we designed an oligonucleotide library to systematically address the factors that determine binding specificity (Figure S1B). A designed (versus randomized) library allowed us to maximize the information content by leveraging prior specificity information. We introduced single and multiple mutations into the PUM2 consensus site, focusing on sequence variants outside the UGUA core to avoid preponderance of non-binders (Figure S1B). We also varied the flanking sequences and included insertions to test the potential for noncontiguous binding sites; finally, we included variants of sequence motifs of related PUF proteins to provide additional sequence variation for testing PUM2 binding models (Figure S1B). To control for structural and context effects, each sequence variant was embedded in two to four scaffolds (Figure 1B).

### Massively Parallel Measurements of PUM2-Binding Affinities

Using RNA-MaP, we determined PUM2 protein binding affinities for >20,000 distinct RNAs, and we report on >5,000 herein; sequences designed to address distinct questions will be reported separately. The DNA library was sequenced on an Illumina MiSeq flow cell, followed by *in situ* transcription in a custom-built imaging and fluidics setup (Figure 1C; Buenrostro et al., 2014; She et al., 2017). RNA transcripts were immobilized by stalling the RNA polymerase at the end of the DNA template, and RNA-protein association was measured by equilibrating the RNA with increasing concentrations of fluorescently labeled protein and by imaging binding to each cluster (comprising  $\sim 1,000$  copies of an RNA variant) (Buenrostro et al., 2014) (Figure 1C). The resulting binding curves were used to obtain the dissociation constant ( $K_D$ ) and the corresponding  $\Delta G$  value ( $= RT \ln K_D$ ) of the protein for each RNA variant.

Figure 1D shows representative binding curves for a consensus sequence (UGUAUUA, “WT”) and a mutated sequence (UGUAGCGC, “mut”) that exhibit divergent affinities ( $K_D = 0.17$  nM and >340 nM, respectively). For most protein concentrations, protein binding to the consensus sequence followed a canonical binding curve (Figure 1D, WT). At the highest protein concentrations, modest additional increase in fluorescence was observed only for sequences that significantly bound PUM2. This signal was well fit by a model in which a second PUM2 weakly binds to the RNA/PUM2 complex (Figure 1D, WT vs mut), and was accounted for by including a nonspecific binding term (STAR Methods), which led to somewhat greater uncertainty in  $K_D$  values for weakly bound RNAs (Figure S1C).

Because our RNA array contained multiple clusters for each sequence variant, numerous binding curves were determined

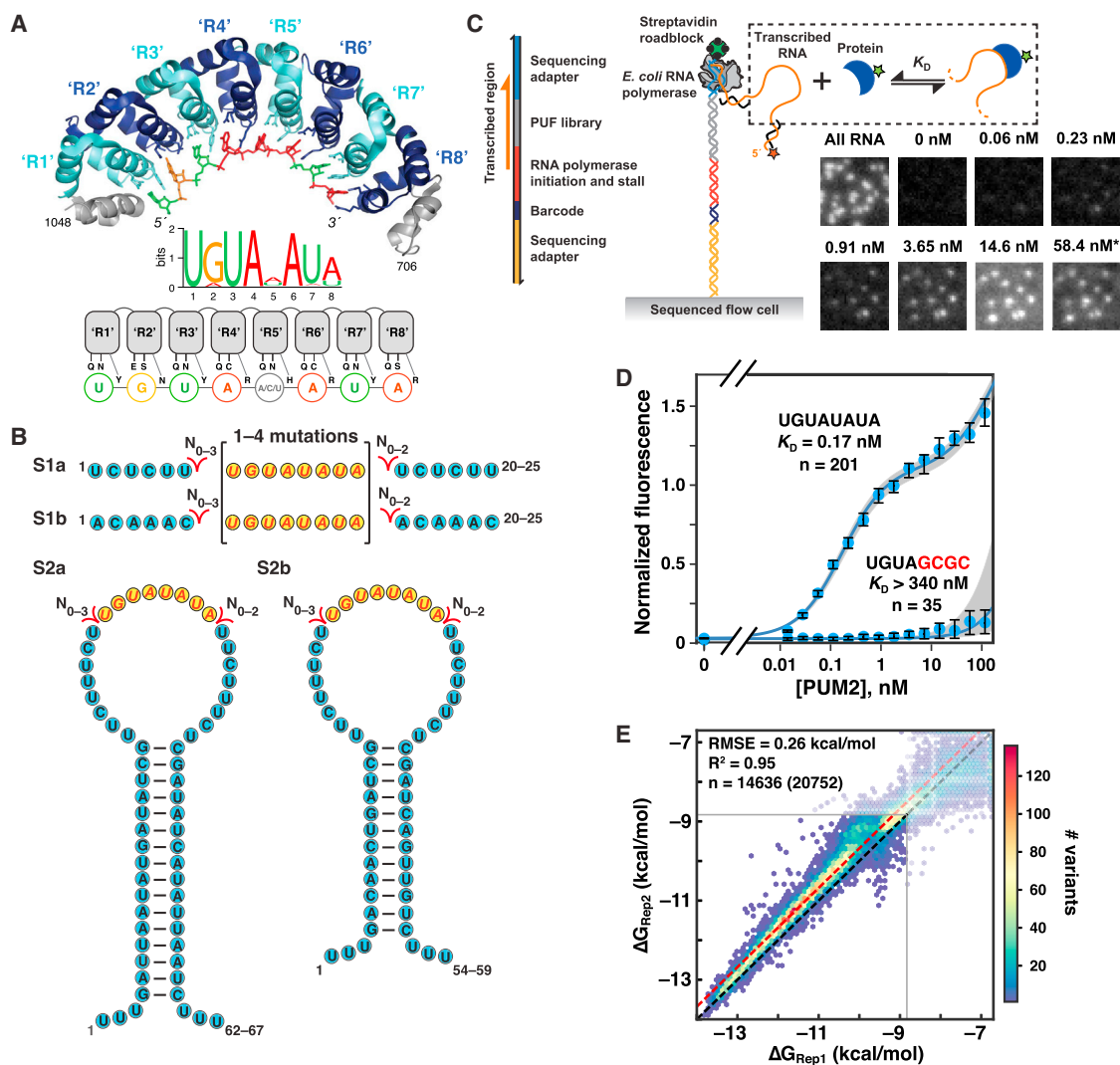


**Figure 1. Quantitative High-Throughput Measurements of RNA Binding to PUM2**

(A) Top: crystal structure of the RNA-binding domain of human PUM2 bound to UGUAAUA RNA (PDB: 3Q0Q; Lu and Hall, 2011). For simplicity, the eight RNA-binding sites (R1–R8) are numbered in the 5' to 3' order of bound RNA residues, the reverse of the order in protein primary sequence. Center: representative PUM2 sequence motif (based on Hafner et al., 2010). Bottom: schematic representation of PUM2 residues involved in base-specific interactions (Wang et al., 2002).

(B) Scaffolds for studying RNA sequence specificity. Yellow circles indicate the variable region (see Figure S1B).

(C) Left: schematic representation of an RNA-MaP experiment (Buenrostro et al., 2014). Right: representative images of a subset of RNA clusters after incubation with increasing PUM2 concentrations. Asterisk at 58.4 nM indicates adjusted contrast relative to other images, due to increased background fluorescence.

(D) Representative binding curves for the consensus sequence (UGUAUUA, S2b scaffold) and a mutated sequence (UGUAGCGC, S1a scaffold). The number of clusters containing the indicated sequence ( $n$ ) is noted. Circles indicate the fluorescence in the protein channel normalized by the fluorescence in the RNA channel. Medians and 95% confidence intervals (CIs) across the clusters are shown. Blue lines indicate the fits to the binding model, which includes a nonspecific term for PUM2 binding to the PUM2-RNA complex, and the gray area indicates the 95% CI of the fit ( $K_D(\text{consensus}) = 0.17$  nM,  $CI_{95\%} = (0.10; 0.35)$ ;  $K_D(\text{mutant}) > 340$  nM, corresponding to the upper limit for binding affinities that could be confidently distinguished from background).

(E) Comparison of technical replicates performed on two different flow cells. Data with at least five clusters per experiment and with  $\Delta G$  error less than 1 kcal/mol (95% CI) are shown. Transparent tiles correspond to  $\Delta G$  values greater than reliably distinguishable from background (STAR Methods);  $n$  corresponds to the number of variants within the high-confidence affinity range, with the total number indicated in parentheses. The black dashed line indicates a slope of 1, and the red line is offset by the mean difference between replicates 1 and 2 (0.32 kcal/mol) that accounts for small differences in protein activity and/or dilution. The RMSE value was calculated after accounting for this offset (RMSE = 0.42 kcal/mol without accounting for the offset). See also Figure S1.

in parallel for each construct. The median number of independent clusters per sequence variant was 23 and 42 in experiment replicate 1 and 2, respectively. Molecular variants were included in downstream analysis when measured in at least five clusters per experiment (Figure S1C), with additional quality filters described in STAR Methods. Independent binding experiments using distinct RNA chips indicated quantitative agreement ( $R^2 = 0.95$ ; Figure 1E), with average reproducibility within less than 2-fold (RMSE = 0.26 kcal/mol) after accounting for a small systematic shift.

### Dissecting and Defining PUM2 Specificity

PUM2 and related Puf3-type PUF proteins appear to recognize RNA in a modular fashion, with each base contacted by one of the eight PUF repeats (Figure 1A; Wang et al., 2002). Thus, independent energetic contributions might be expected from consecutive RNA bases bound at each of the eight PUF repeats, as assumed in motif descriptions (Schneider and Stephens, 1990; Stormo, 2000). In this section, we test this and other thermodynamic models.

#### Comprehensive Analysis of Single-Mutant Variants

We first assessed the binding of all single mutants of the 8-mer consensus UGUUAUA in two to four scaffolds (Figure 2A). At all positions, we see the strongest binding for the consensus residue (circled), with very low discrimination at position 5, consistent with prior results (Dominguez et al., 2018; Galgano et al., 2008; Hafner et al., 2010; Lu and Hall, 2011).

Surprisingly, while the effects of single mutations generally agreed across scaffolds, the spread of deviations was considerably greater than expected from error (Figure 2B; 25°C, “Observed” versus dashed line; Figure S2A). Significant deviations between scaffolds occurred in 13 of the 25 sequence variants, at a 10% false discovery rate (FDR; Figure 2A, “\*\*\*”). We considered several potential origins for how scaffolds might influence single mutant effects.

First, we assessed if RNA secondary structure might limit PUM2 access to its site (Figure 2C) to differing extents among scaffolds. If structure affected binding, the differences between scaffolds should decrease at 37°C. Indeed, smaller differences were observed at this higher temperature (Figures 2B and S2A), with only 2 of the 25 sequence variants exhibiting significant deviations between scaffolds (Figure S2C). Accounting for structure effects with stabilities predicted by Vienna RNAfold (Lorenz et al., 2011) also considerably reduced the between-scaffold deviations (Figures 2B and 2D), with only 5 of the initial 13 variants exhibiting significant inter-scaffold deviations at 25°C and none at 37°C (asterisks in Figure 2A versus Figures 2D and S2C). Thus, RNA secondary structure can account for most inter-scaffold variation.

We next investigated whether scaffold differences were associated with alternative binding registers, which would diminish the observed mutational penalty (Figure S2D). We calculated predicted binding affinities in all possible binding registers (scaffold + designed binding site) using a model that assumes independent effects of individual mutations. 18 of the 61 variants in Figures 2A and 2D had an alternative register with a predicted  $K_D$  within 5-fold of the measured value (Table S1). For the 2C mutant, three of the four scaffolds have alternative registers

with affinities matching the observed values (Figure S2E). Thus, in this case the seeming outlier (scaffold S1b) gives the most accurate mutant penalty, underscoring the value of multiple scaffolds and the importance of accounting for alternative binding sites.

Finally, we assessed whether scaffold variation was caused by sequence preferences outside the canonical PUM2 8-mer site. The library included a set of constructs that varied the flanking sequence two bases upstream (−2, −1) and downstream (+1, +2) of the common consensus sequence ( $n = 209$  across four scaffolds; Figure S2F). We found modest effects at position +1, with G(+1) bound most tightly (Figure S2F), with no significant effects at other flanking positions. The G(+1) effect was confirmed in gel shift experiments (Figure S2G). However, since none of our scaffolds contained a G at this position, flanking effects did not impact the observed differences of single mutant measurements between scaffolds.

The above insights enabled us to determine high-confidence single mutant effects for all positions, using values corrected for secondary structure stability (Figure S2D) and using only sequence variants without alternative binding registers. We additionally took advantage of the observation that substituting the uridine at position 5 with A or C residues did not affect the binding affinity (Figure 2D (Lu and Hall, 2011)) and that none of the single mutants in the 5A or 5C backgrounds had stable predicted alternative registers (Figure S3A). Figure 2E summarizes the median single mutant effects across scaffolds and across 5A/C/U backgrounds. We observed excellent agreement between the effects derived from 25°C and 37°C data, with a constant destabilization of binding by  $(20 \pm 10)$ -fold at the higher temperature (Figures S3A–S3E). RNA array measurements also agreed with gel-shift measurements of 14 single mutants (Figures 2F and S3F).

#### Testing an Additive Model for PUM2 Specificity

If binding of RNA residues by consecutive PUF repeats contributed independently to PUM2 affinity, then the affinities for any RNA sequence ought to be predicted from adding the measured single mutant penalties (“additive consecutive model”; Figure 3A, top). To test this model, we calculated the predicted affinities for our entire library using 36 terms, one for each residue at each of the 9 recognition sites (8 canonical PUF repeats and the additional G9 site), determined from our single mutant data (Figure 2E; Table S2). In the predictions, we accounted for all possible binding registers by calculating the ensemble affinity across all possible 9mers (STAR Methods). We then compared the predicted and measured affinities for RNAs predicted to contain little or no structure ( $\Delta\Delta G_{\text{fold}} > -0.5$  kcal/mol;  $n = 5,206$ ). This set included RNAs with mutations or insertions throughout the PUM2 consensus sequence, variation in flanking sequence, and variations of consensus motifs of other PUF proteins (Figure S1B).

While the predicted and observed binding energies strongly correlated ( $R^2 = 0.73$ ), 27% of the observed values deviated from predictions by  $>1.0$  kcal/mol, well beyond our experimental error of 0.14 kcal/mol (Figure 3A). Furthermore, the vast majority of outliers bound tighter than predicted (Figure S4A). We therefore explored additional features that might lead to tighter-than-predicted PUM2 binding.

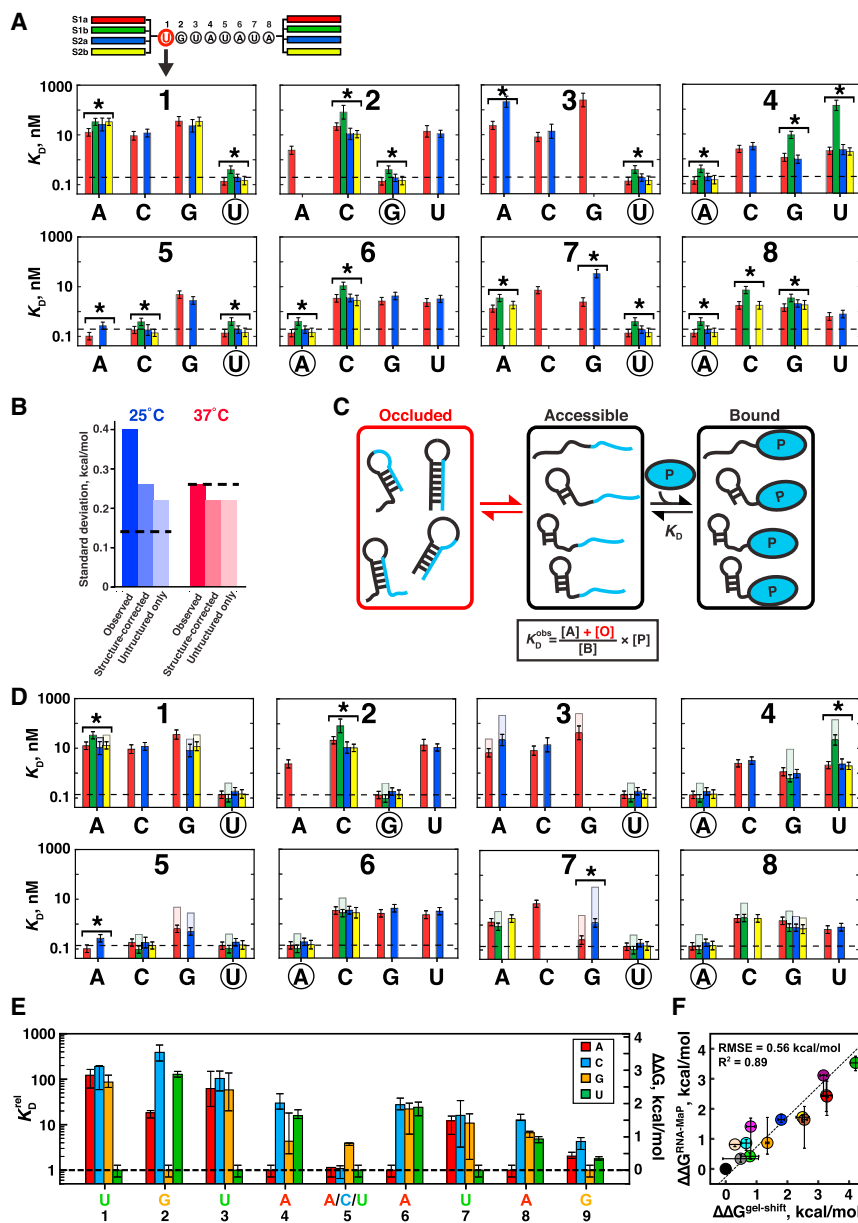


**Figure 2. Analysis of Single-Mutant Variant Binding to PUM2**

(A) Top: color code for the scaffolds in Figure 1B; the arrow points to affinities for each position 1 sequence variant. Bottom:  $K_D$  values of PUM2 for single mutants at each position of the UGUUAUUA consensus. Bars indicate weighted means of two replicate measurements and error bars indicate weighted replicate errors. The dashed line indicates the average affinity for the consensus sequence across the four scaffolds, and the consensus residues are circled. Asterisks indicate variants with significant differences between scaffolds (10% FDR).

(B) Scaffold variance before and after accounting for RNA secondary structure and after excluding sequences with predicted structure. The bars indicate standard deviations of the distribution of differences between each measured value (part A) and the scaffold mean for the respective sequence variant; see also Figure S2A and STAR Methods. Dashed lines indicate the standard deviation of measurement error. The experimental standard deviation was higher at 37°C than 25°C because of weaker binding and the absence of an independent duplicate experiment.

(C) Model for RNA structure effects on PUM2 binding. Occluded RNA molecules increase the observed dissociation constant (weaken binding) by stabilizing the unbound state (see also Figure S2B and STAR Methods).

(D) Single-mutant affinities after accounting for structure effects predicted by RNAfold (solid bars; Lorenz et al., 2011); the transparent region indicates the structure correction. Error bars indicate weighted replicate errors. Asterisks indicate variants with significant scaffold differences after accounting for structure effects.

(E) Median effects of each single mutation (residues 1–8) across scaffolds and across 5A/C/U backgrounds at 25°C, after excluding variants with alternative binding registers and after accounting for structure. Error bars indicate 95% CIs of the median. Mutational effects were calculated relative to the weighted mean affinity for the UGUA[A/C/U]AUA consensus across scaffolds. Position 9 specificity was derived as shown in Figure S2F and the mutational effect was calculated relative to the most tightly bound residue (G).

(F) Comparison of single-mutant affinities measured by RNA-MaP (Figure 2E) and by gel shift. 1C, purple; 2A, yellow; 2C, green; 3A, white; 3G, red; 4G, orange; 4U, blue; 5G, wheat; 7C, brown; 7G, magenta; 9A, lime; 9C, cyan; 9U, gray. The gel-shift values are averages and 95% CIs from two to four measurements. See also Figures S2 and S3.

### Residue Flipping Accounts for Most Deviations from the Additive Consecutive Model

Several PUF proteins bind RNAs with residues “flipped out” to yield longer, nonconsecutive binding motifs (Gupta et al., 2008; Miller et al., 2008; Valley et al., 2012; Wang et al., 2009; Wilinski et al., 2015). Human PUM1 protein, which has >90% sequence identity to PUM2 in its RNA-binding domain, has two X-ray structures with bound RNA sequences each with one residue flipped out (Gupta et al., 2008). To assess whether base flipping significantly contributes to RNA binding to PUM2, we had included in our library a set of RNAs with C insertions throughout the

UGUAUUA consensus sequence (Figure 3B), with C insertions chosen, because none of the PUM2 repeats preferentially bind C. In the absence of base flipping, a C insertion would cause one or more mismatches in the PUM2 binding site, leading to a large penalty (Figure 3C). Instead, at four positions within the PUM2 motif, insertion of the C residue had a much smaller effect than predicted by the additive consecutive model, consistent with base flipping (Figures 3C and 3D). For example, the insertion between residues 5 and 6 leads to binding that is 3.4 kcal/mol stronger than predicted (Figure 3C), and the 0.9 kcal/mol observed destabilization relative to the consensus sequence

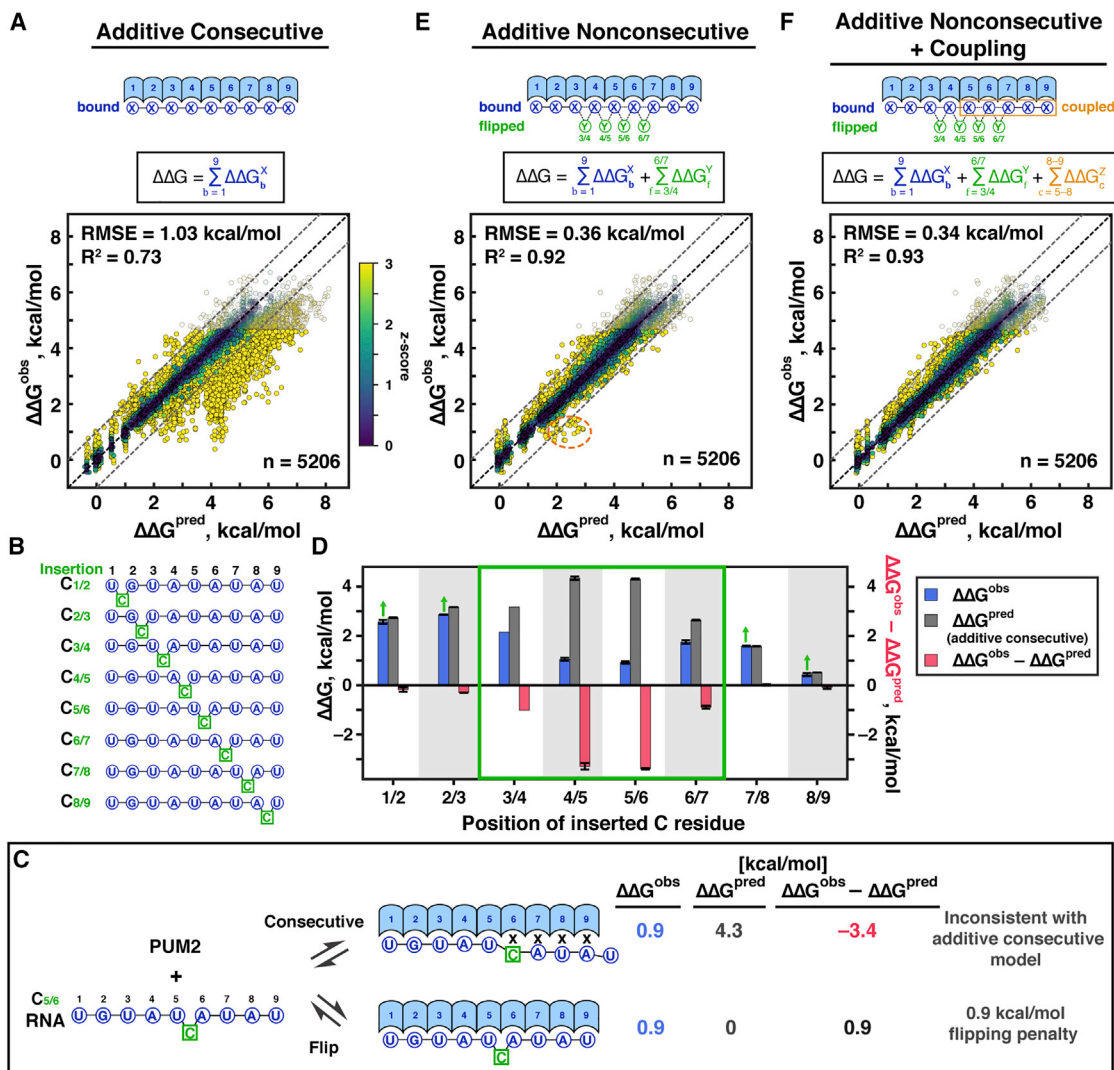


**Figure 3. Development of a Predictive Model for PUM2 Specificity**

(A) Top: schematic representation and test of the additive consecutive model.  $b$  is the position of bound base, and  $X$  is the base at position  $b$ .  $\Delta\Delta G_b^X$  values correspond to the measured single mutation penalties at 25°C (Figure 2E; Table S2). Bottom: predicted versus observed  $\Delta\Delta G$  values relative to the UGUUAUAU consensus sequence for all unstructured variants in the library. Predicted  $\Delta\Delta G$  values account for the ensemble of all possible registers along the RNA sequence (STAR Methods). Transparent symbols indicate variants bound more weakly than the threshold for high-confidence affinity determination; these variants were excluded from determining the  $R^2$  and RMSE values and from global fitting in parts E and F. Points are colored based on the deviation from predicted affinity, divided by the uncertainty of the measurement ( $z = |\Delta\Delta G_{\text{obs}} - \Delta\Delta G_{\text{pred}}| / \sigma_{\Delta\Delta G}$ ; capped at  $z = 3$  for visualization). The black dashed line is the unity line and the dashed gray lines denote 1 kcal/mol deviation from the predicted value.

(B) C-insertion library for base-flipping analysis.

(C) Example of an insertion that gives binding tighter than predicted by the additive consecutive binding model and provides evidence for base flipping.  $X$  indicates a mismatch.  $\Delta\Delta G^{\text{pred}}$  corresponds to the prediction from additive consecutive model (Figure 3A). With flipping,  $\Delta\Delta G^{\text{pred}}$  indicates the prediction accounting for bound positions only, which is 0 as the consensus residues are in each site.

(D) Summary of observed and predicted  $\Delta\Delta G$  values for each of the C insertions in part B. Green box indicates positions at which the observed  $\Delta\Delta G$  values are smaller than predicted, suggesting base flipping. Arrows indicate that the observed affinities are lower limits for base flipping penalties. Averages and standard errors for library variants containing the consensus sequence with the indicated insertion and lacking stable alternative registers are shown (Table S3).

(E) Additive nonconsecutive model.  $Y$  indicates the residue(s) flipped at position  $f$ . Numbering of flipped residues is based on the flanking bound residues; 3/4–6/7. The dashed orange outline indicates a cluster of outliers with residue coupling.

(F) Final model including binding, flipping, and coupling terms.  $c$  indicates the positions of coupled residues, and  $Z$  is the identity of coupled residues. Final model parameters are provided in Table 1.

See also Figures S4–S6 and Tables S2, S3, S4, and S5.

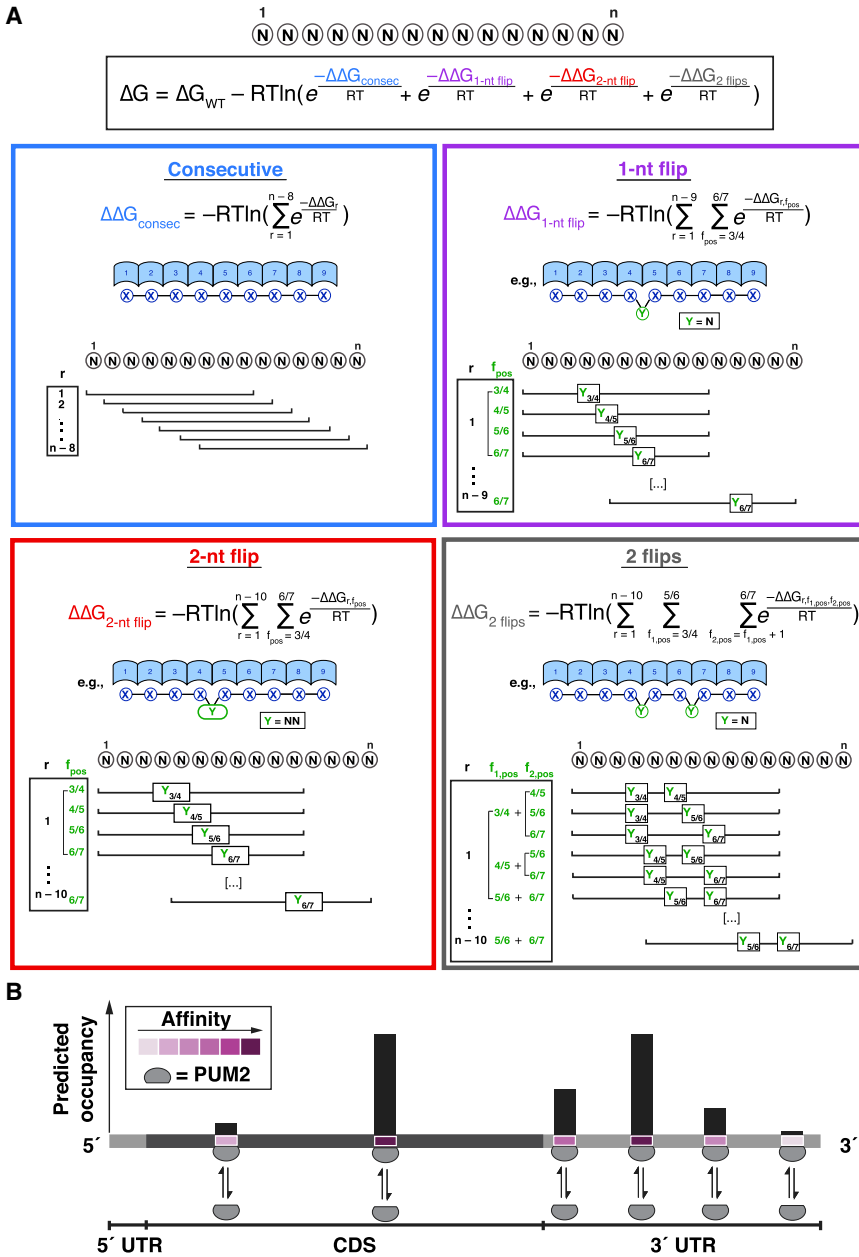


**Figure 4. Thermodynamic Model for PUM2 Binding Integrating Binding Modes and Registers**

(A) An RNA sequence of length  $n$  can be bound in a series of 9- to 11-mer registers ( $r$ ), within which the RNA residues are variably distributed between bound and flipped positions. Representative subsets of binding registers and base arrangements are shown for each of the four binding modes included in the model: consecutive, 1-nt, and 2-nt flips (at a single position) and two flips at different positions. The equations indicate integration of predicted  $\Delta \Delta G$  values for all possible binding sites to obtain the final affinity. The  $\Delta \Delta G$  values for predicting individual binding site configurations are given in Table 1.  $\Delta G_{WT}$  is the affinity for the consensus sequence.

(B) Schematic representation of a predictive model of PUM2 occupancies on an mRNA target (see STAR Methods).

from 1.03 to 0.36 kcal/mol and  $R^2$  increased from 0.73 to 0.92 (Figure 3E versus Figure 3A). This large improvement is not a consequence of allowing the single-mutant values to vary in global fit, as a global fit to the additive consecutive model with variable single-mutant values gave considerably poorer predictions (Figures S4B and S4C). Despite the overall improvement observed with the additive nonconsecutive model, there remained a subset of significant outliers (Figure 3E) that led us to carry out additional analyses for energetic coupling.

**Energetic Coupling between Neighboring Residues**

Inspection of the cluster of variants that bound tighter than predicted even after accounting for flipping (Figure 3E, dashed outline) revealed an enrichment for variants with a G mutation at position 7 accompanied by mutations at position 8, suggesting potential coupling between

suggests an energetic penalty for flipping a C residue at this position of 0.9 kcal/mol. Thus, our data suggest that PUM2 can bind RNAs with flipped out residues in certain positions, and we modeled this behavior in an extended “additive nonconsecutive model.”

The additive nonconsecutive model combines independent energetic contributions from each of the 9 bound residues with the ability to flip up to two residues (Figure 3E, top). To determine the associated energetic penalties, this model was fit to our 5206 measured binding affinities, accounting for all possible binding modes and registers (STAR Methods; see Figure 4A). The additive nonconsecutive model gave improved agreement with the data, with the root mean square error (RMSE) reduced

these neighboring mutations. For an unbiased assessment of coupling at all positions, we considered all double mutants of the PUM2 consensus site, which revealed that coupling between positions 7 and 8 was the strongest, and deviations from additive predictions at all other positions were  $<0.5$  kcal/mol (Figure S4D). Further analysis revealed that (1) coupling between positions 7 and 8 occurred with G or C at position 7; (2) for 7G, coupling occurred only when position 6 was the consensus residue (A) and a pyrimidine was present at position 5 (Figure S4E), and these variants fully explained the cluster of outliers observed in Figure 3E (Figure S4E, top); and (3) for 7C, the deviations from additivity were greatest when position 6 was mutated (not A) (Figure S4F).



**Table 1. Thermodynamic Parameter Values for the Additive Nonconsecutive Coupling Model**

Term I	$\Delta\Delta G_b^X$ (kcal/mol)									
	X =									
Bound Residue Position b =	A	C	G	U						
1	3.08	2.91	3.04	0.00						
2	1.93	3.14	0.00	3.14						
3	2.39	2.49	2.92	0.00						
4	0.00	1.92	1.71	1.46						
5	-0.03	0.17	0.79	0.00						
6	0.00	1.83	1.82	1.49						
7	1.55	1.78	1.59	0.00						
8	0.00	1.57	1.52	1.01						
9	0.30	0.29	-0.07	0.00						
Term II	$\Delta\Delta G_f^Y$ (kcal/mol)									
	Y =									
Flipped Residue Position f =	A	C	G	U	NN <sup>a</sup>	∅				
3/4	>2 <sup>b</sup>	1.79	>1.5	1.41	>2.5	0				
4/5	>2	>3	>2.5	>2.5	>2.5	0				
5/6	1.22	1.05	1.57	0.81	2.18	0				
6/7	>2	1.77	>2	2.02	2.04	0				
Term III	$\Delta\Delta G_c^Z$ (kcal/mol) <sup>c</sup>									
	Z =									
Coupled Residue Positions c =	<u>5</u>	<u>6</u>	<u>7</u>	<u>8</u>	<u>6</u>	<u>7</u>	<u>8</u>	<u>8</u>	<u>9</u>	all other
	C/U	A	G	C/G/U	C/G/U	C	C/G/U	C/G/U	X	
5-8	-1.53				-			-		0
6-8					-0.91			-		0
8-9								- $\Delta\Delta G_9^X$ <sup>d</sup>		0

<sup>a</sup>2-nt flip of any sequence.

<sup>b</sup>">" indicates a lower limit (see Figure S6A).

<sup>c</sup>Coupling terms are defined as combinations of residues that meet all of the indicated conditions at the indicated sets of positions. For example, the coupling term  $\Delta\Delta G_c^{6-8}$  has the value of -0.91 kcal/mol if position 7 residue is a C and position 6 and 8 residues are not A (C/G/U); for all other combinations of sequences, the value of the coupling term is 0.

<sup>d</sup>Coupling term indicates that the position 9 binding term ( $\Delta\Delta G_9^X$ ; "term I") is only implemented when position 8 is the consensus residue A.

We also observed small deviations from additivity at positions 8 and 9 (Figure S4D). Physically, an absence of stable binding in the PUM2 site "8" would be expected to increase the entropic penalty for forming the site "9" interaction and thus might weaken or eliminate this interaction. Indeed, we found that the modest stabilizing effect of 9G relative to other residues was only present with the consensus A at position 8 (Figure S4G).

Figure 3F shows the global fit to our final model that includes additive terms for bound and flipped residues and the coupling terms described above (Table 1). For 99% of the data, this final model predicted our observations to within 1 kcal/mol and it gave a slight overall improvement relative to the additive nonconsecutive model (Figure 3E versus Figure 3F).

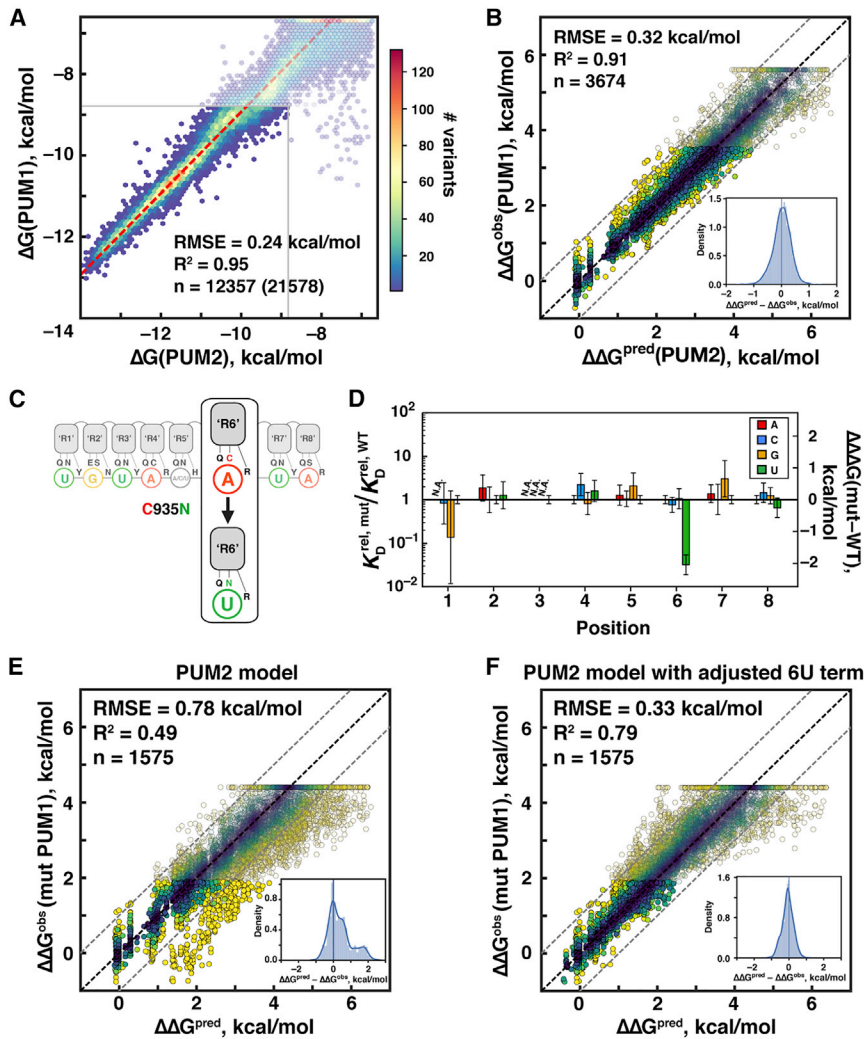
#### Evaluating the Final PUM2-Binding Model

Control fits and analyses demonstrated that the fit model parameters were stable to variation in initial parameter values, data re-sampling, and the use of different fitting methods (STAR Methods). Training and testing sets gave essentially identical R<sup>2</sup> and RMSE values, suggesting that the model was not overfit. Assessment of RMSE sensitivity to individually varying each

model parameter revealed that, as expected, the free energy terms for the consensus residues were most highly constrained, as these residues were present in the majority of the RNAs, while penalties for mismatched bound residues were less well constrained (Figure S5A). Approximately half of the flipping terms in the model were well constrained, while the other half provided lower limits for the free energy penalties, generally because the penalties were sufficiently high that either no binding or binding in an alternative register was observed (Figure S6A). In addition, the lack of specificity for the "bound" base at position 5 limited our ability to distinguish flipping at position "4/5" versus position "5/6" (numbering of flipped residues is based on the flanking bound residues; Figure 3E).

#### Implementation of the Predictive Model of RNA Binding by PUM2

The thermodynamic model for PUM2 binding can be applied to any RNA by calculating the ensemble free energy across each of the possible binding modes (consecutive, one or two residues flipped) and binding registers, as illustrated for a 15-nt RNA example in Figure 4A. The model can be further extended to



predict PUM2 occupancies along larger, physiological RNAs, as illustrated schematically for an mRNA target in Figure 4B, and we provide an algorithm for occupancy predictions (see STAR Methods).

### Evaluating Specificity across Human Pumilio Proteins

Human PUM1 shares 91% sequence identity and 97% sequence similarity in its RNA-binding domain (RBD) with PUM2, and all of the RNA-interacting amino acids are identical between the two proteins. Prior studies revealed nearly identical RNA sequence motifs and considerable overlap in apparent targets, highlighting the question of why humans retain two seemingly redundant proteins (Figure S1A) (Goldstrohm et al., 2018). To test potential quantitative differences in PUM1 and PUM2 sequence specificity and to assess if our PUM2-derived binding model could be extended to predict PUM1 binding, we compared PUM1 and PUM2 binding across our RNA sequence library.

PUM1 and PUM2 binding showed high agreement, indistinguishable from the concordance between PUM2 replicates

cellular localization (Goldstrohm et al., 2018; Kedde et al., 2010; Thul et al., 2017).

### Evaluating the Precision of Pumilio Engineering

The modular structure of PUF proteins has made them attractive platforms for engineering new RNA specificities (Chen and Varani, 2013; Lu et al., 2009). Given our observation of complexity of the PUF protein specificity landscape that is not captured by a simple linear motif, we aimed to comprehensively evaluate the precision of PUF protein engineering using a previously designed PUM1 mutant, in which specificity for position 6 in the RNA was altered from A to U through a single amino-acid substitution in repeat “R6” (Cheong and Hall, 2006) (Figure 5C).

Analysis of single-mutant penalties relative to wild-type PUM1 confirmed a change in mutant PUM1 specificity at position 6, with no significant differences observed for other residues and positions, supporting a local effect from the PUM1 mutation (Figure 5D).

We next asked if our thermodynamic model could be applied to the engineered PUM1 protein. Changing a single term in our

### Figure 5. Comparison of RNA-Binding Specificities of PUM2 and Wild-Type and Engineered PUM1 Proteins

(A) Correlation between PUM1 and PUM2 affinities across the library. The red line has a slope of 1 with an offset of 1.07 kcal/mol, corresponding to weaker observed binding for PUM1 than PUM2; the RMSE value was calculated after accounting for the constant offset.

(B) Predicting PUM1 binding with the PUM2-based model. Inset shows the distribution of deviations from predicted values.

(C) Schematic representation of the single amino-acid change in repeat “R6” of engineered PUM1.

(D) Differences between the single mutant specificities of wild-type and mutant PUM1. Differences between weighted means of single mutant penalties across scaffolds in the UGUUAUUA background are shown, and the error bars indicate propagated weighted errors. N.A. indicates lack of detectable binding by mutant PUM1.

(E) Predicted mutant PUM1 affinities (based on the PUM2 model) versus observed affinities; the  $\Delta\Delta G$  values are relative to the UGUUAUUA consensus. Despite accurate predictions for most variants, 18% of variants deviated by  $>1$  kcal/mol, consistent with altered specificity of mutant PUM1.

(F) Predicted versus observed mutant PUM1 affinities with the altered 6U penalty.

(Figure 5A versus Figure 1E). Therefore, our model derived from PUM2 data can also be used to predict PUM1 binding (Figure 5B). The identical RNA sequence specificities suggest that any functional differences between PUM1 and PUM2 are fully determined by other factors, such as differences in modification patterns, protein interaction partners, or sub-

binding model to account for the altered 6U penalty for mutant PUM1 ( $-0.32$  kcal/mol instead of  $+1.49$  kcal/mol) gave accurate predictions across our library, with 99% of variant affinities predicted to within 1 kcal/mol (Figures 5E and 5F). Thus, our quantitative model can be readily modified and applied to new PUF proteins.

### Assessing the Thermodynamic Model for PUM2-RNA Occupancies *In Vivo*

To assess the extent to which *in vivo* binding is driven thermodynamically, we compared predictions from our thermodynamic binding model to published *in vivo* enhanced UV crosslinking and immunoprecipitation (eCLIP) measurements for PUM2 from the ENCODE project (Consortium, 2012; Van Nostrand et al., 2016). Putative PUM2 binding sites within expressed mRNAs were identified as sites with predicted binding affinities within 4.0 kcal/mol ( $\sim 1,000$ -fold) of the consensus sequence. eCLIP signal was divided by the relative expression of its transcript and evaluated in bins of predicted affinity, because quantification of individual RNA sites is currently limited by low sequencing depths and may be further subject to experimental biases (Darnell, 2010; Sugimoto et al., 2012; Wheeler et al., 2018). Strikingly, we observed quantitative agreement between relative affinities predicted by our thermodynamic model and the median eCLIP enrichment signal across the predicted affinity bins (Figure 6A, points versus dashed line). Close agreement was observed for predicted sites both with and without flipped residues (Figure 6B). Thus, *in vivo* binding data are consistent with thermodynamically driven occupancy, and the binding sequences and modes identified by RNA-MaP are bound, on average, at the levels expected based on their affinities.

Because Pumilio proteins have generally been identified to act via 3' UTRs (Goldstrohm et al., 2018), we wondered whether there might be lower average occupancy in coding sequences (CDSs) and in 5' UTRs (e.g., due to displacement of PUM2 from CDS sites by translating ribosomes). Comparison of the occupancy around PUM2 sites in 3' UTRs and CDSs showed indistinguishable eCLIP enrichments (Figure 6C; 5' UTR sites were not included because of the small number of predicted sites in this region), suggesting that inherent thermodynamic stability of a site is the overarching driver of *in vivo* occupancy rather than the location of the site within the mRNA.

We observed a strong enrichment of PUM2 consensus sites in 3' UTR sequences relative to CDS and 5' UTR regions, with  $\sim 90\%$  of consensus sites located in 3' UTRs, despite 3' UTRs constituting on average only 38% of the mRNA length (Figures 6D and 6E; Consortium, 2012). 3' UTR enrichment was evident, though diminished, for sites with weaker predicted affinities, suggesting that these sites may also play functional roles via 3' UTR binding.

*In vitro* measurements indicated that RNA secondary structure formation can strongly limit the accessibility of PUM2 binding sites and thus decrease PUM2 binding (Figures 2C and 2D) (Becker et al., 2019a). In contrast to the pronounced structure effects observed *in vitro*, comparisons of *in vivo* eCLIP signal around consensus sites with varying predicted structure content revealed no change in median occupancy for predicted structural stability of up to  $\sim 4$  kcal/mol (Figure 6F; 37°C). A rare subset

(<2%) of sites had very high predicted structure stability ( $\Delta\Delta G_{\text{fold}} > 8.6$  kcal/mol) and showed slightly diminished eCLIP signal, suggesting that highly stable structures may lead to decreased binding. However, RNA structure effects on the vast majority of PUM2 sites appear to be negligible *in vivo*.

## DISCUSSION

RNA-protein interactions are integral to regulation of gene expression (Singh et al., 2015). To define and predict the complex networks of RNA-protein interactions, quantitative descriptions of RNA-RBP thermodynamics are needed. Toward this goal, we have built a predictive model for RNA binding by the human PUM1 and PUM2 proteins. This model, along with direct thermodynamic binding measurements for thousands of RNAs, provides testable predictions of *in vivo* RNA interactions and yields biological and biophysical insights.

### Applications to Cellular Interactions and RNA Properties

Comparison of predictions from the thermodynamic binding model to published *in vivo* cross-linking data (Van Nostrand et al., 2016) supports the simple notion that thermodynamics is a prime driver in determining RNA occupancy for PUM2 (Figures 6A and S7B). While it would be surprising if thermodynamic affinities did not influence RNA binding *in vivo*, other models are possible. For example, rapid Pumilio protein dissociation by the action of RNA helicases would level occupancies for all sites above a certain threshold affinity (Figure S7C), and translation by ribosomes that displaces PUM2 proteins faster than equilibration of PUM2 binding would yield CDS occupancies lower than 3' UTR occupancies. However, a close correspondence between thermodynamic predictions and *in vivo* crosslinking provides evidence against these alternate models (Figures 6A and 6C). Ribosomes traverse CDS sites, and presumably displace bound factors, approximately once every 10 s ( $\sim 0.1$  s $^{-1}$ ; Halstead et al., 2015; Schwanhäusser et al., 2013). This rate sets an upper limit for the equilibration time for PUM2 binding—it must occur faster than ribosomal displacement for us to observe no difference in occupancy in CDSs compared to 3' UTRs. This rough lower limit estimate is similar to the rate constant for dissociation of PUM2 from the consensus sequence *in vitro* ( $\sim 0.1$  s $^{-1}$ ; 37°C; unpublished data), suggesting that indeed PUM2 dissociates from consensus sites on the timescale of translation, and faster for nonconsensus sites.

Recent studies have suggested that RNA structure is destabilized in the cellular milieu (Ding et al., 2014; Guo and Bartel, 2016; Rouskin et al., 2014; Spitale et al., 2015). Using published *in vivo* eCLIP data (Van Nostrand et al., 2016), we observed that binding sites predicted to be minimally accessible ( $<0.1\%$ ;  $\Delta\Delta G_{\text{fold}} \geq 4$  kcal/mol) gave PUM2 enrichments essentially indistinguishable from sites predicted to lack structure (Figure 6F). These results provide independent support for structure disruption *in vivo*, which could result from a high density of bound RBPs that outcompete RNA structure formation and/or the action of RNA chaperones. Moving forward, coupling *in vitro* thermodynamic measurements with quantitative *in vivo* analysis will aid in determination of cellular factors responsible for destabilizing RNA structure.

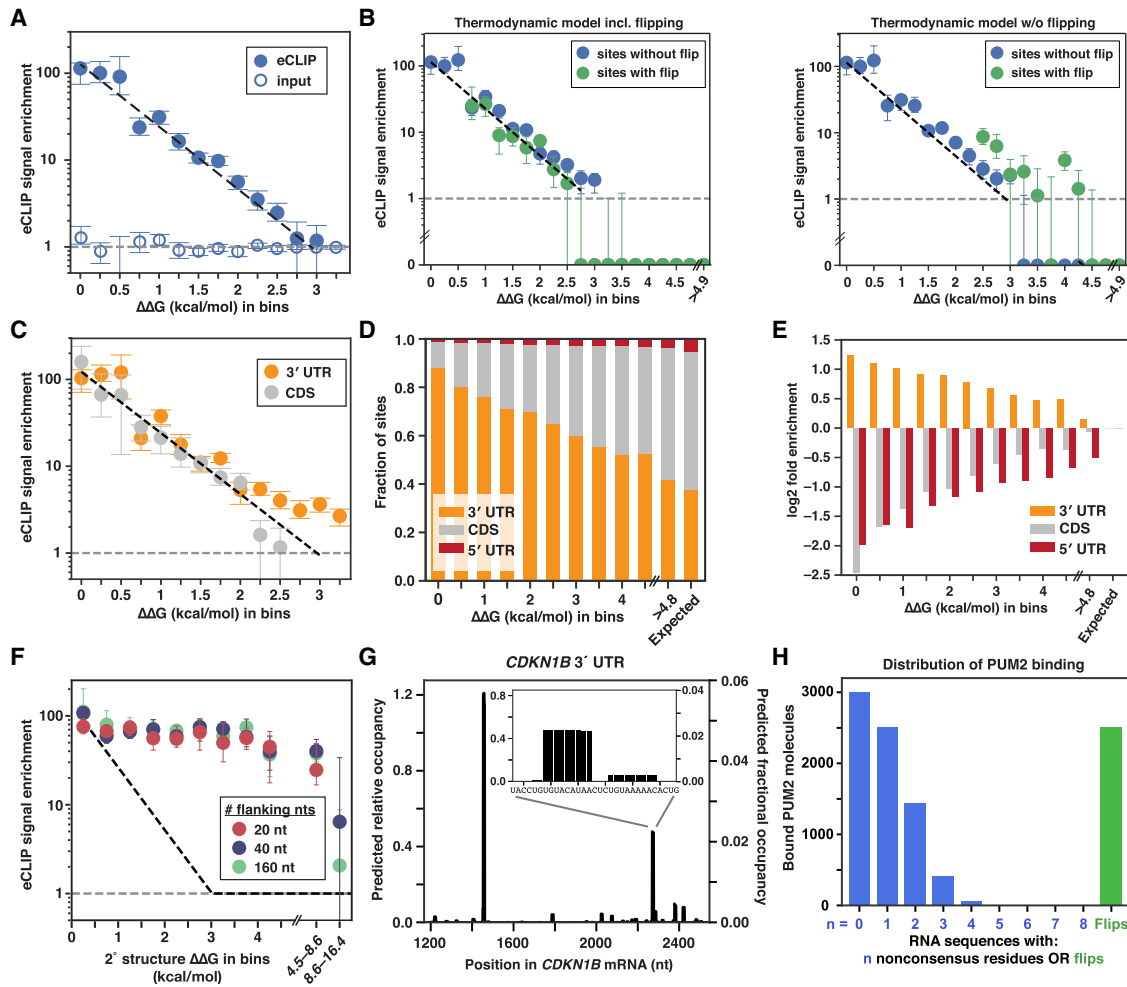


**Figure 6. Testing the Thermodynamic Model in Vivo**

(A) Thermodynamic affinity predictions compared to eCLIP enrichment in K562 cells (Van Nostrand et al., 2016). Median eCLIP enrichments across sites within bins of predicted relative affinities are shown, and error bars indicate 95% CIs on the median. Only sites lacking adjacent UGUA-containing sites (within 100 nt) are shown due to inflation of eCLIP signal observed in the presence of nearby sites (Figure S7A). Black dashed line indicates the predicted change in eCLIP signal with increasing predicted  $\Delta\Delta G$  values, relative to the eCLIP signal in the lowest  $\Delta\Delta G$  bin. eCLIP (closed circles) and input (open circles) correspond to crosslinked samples that were or were not treated with anti-PUM2 antibody, respectively (Van Nostrand et al., 2016). The gray dashed line indicates the eCLIP enrichment for sites with predicted  $\Delta\Delta G$  values greater than 4.5 kcal/mol (expressed transcripts); since eCLIP signal and input were each normalized to this value, this expected enrichment is equal to 1. Numbers of sites per bin range from 97 to 14,787 and are provided in Table S6.

(B) Median eCLIP enrichment and 95% CIs across bins of predicted  $\Delta\Delta G$ , using either the full thermodynamic model (left) or a model that does not take into account flipped residues (right). Only bins with at least 25 sites are shown.

(C) Comparison of eCLIP enrichment for sites within 3' UTR (orange) or CDS (gray) regions of expressed genes in K562 cells. Medians and 95% CIs are shown. Black and gray lines are as in A.

(D) Fractions of sites annotated as 3' UTR, CDS, or 5' UTR within bins of predicted  $\Delta\Delta G$  values.

(E) Fold difference ( $\log_2$ ) of the observed fraction of sites with the given annotation (5' UTR, CDS, and 3' UTR) versus the expected fraction (based on randomly selected sites).

(F) Median eCLIP enrichment of consensus sites across bins of predicted secondary structure stabilities for structures blocking the PUM2 consensus site (Figure 2C; STAR Methods). Colors indicate the number of flanking nucleotides (nt) included in the stability calculations. Dashed line indicates the predicted change in eCLIP signal for increasing secondary structure stability at 37°C. Medians and 95% CIs for bins with at least 20 sites are shown.

(G) Example of thermodynamic occupancy predictions for the 3' UTR region of the human cyclin-dependent kinase inhibitor 1b *CDKN1B* mRNA, a known target of human Pumilio proteins (Kedde et al., 2010). The left axis indicates predicted relative occupancies with respect to the UGUUAUUAU consensus; the right axis indicates predicted fractional occupancies (i.e., fraction of bound versus total *CDKN1B* mRNA) after accounting for cellular PUM2 and RNA abundances (see STAR Methods).

(H) PUM2-binding landscape across the human transcriptome, predicted by our thermodynamic model using *in vivo* PUM2 and mRNA levels (see STAR Methods). Bars indicate the number of bound PUM2 molecules across RNA binding sites with zero to eight nonconsensus residues without flipped residues (blue) or with up to two flipped residues (green). The consensus was defined as UGU[A/CU]AUAN. See Table S6 for numbers of sites of each type.

See also Figure S7 and Table S6.

### Generalizability of the Thermodynamic Model and Potential Improvements

The rational design of our RNA-MaP library ensured high coverage of predicted binding sites; for example, despite measuring only 4.2% of all possible 9mers, the fraction of predicted “binders” (9mers with  $\Delta\Delta G^{\text{pred}} < 4.5$  kcal/mol) in this library was 35%. Comparisons to published RNA Bind-n-Seq (RBNS) data for human PUM1 (Consortium, 2012; Dominguez et al., 2018) confirmed that the model performed indistinguishably for sequences that were or were not represented in the RNA-MaP library ( $R^2$ : 0.74 versus 0.75; Figure S7D), supporting generalizability. In the future, the model may be further improved through more comprehensive measurements of neighboring double and triple mutations, which may identify additional weak coupling terms; additionally, greater sequence coverage of insertions longer than 1 nt would allow full assessment of the sequence dependence of flipping penalties. While we do not expect these improvements to have major effects on the overall accuracy, they may lead to identification of additional stable binders.

### An Algorithm for Predicting PUM1 and PUM2 Occupancies

The thermodynamic binding model, along with estimated *in vivo* PUM1, PUM2, and RNA levels, allows prediction of PUM1 and PUM2 occupancy across the entire transcriptome. We supply a computational algorithm to carry out these predictions, and depict the output of this tool for one transcript in Figure 6G. The algorithm can be used to predict occupancies for individual sites and RNAs and to design future tests for cellular factors that might affect PUM1 and PUM2 binding.

### Implications for Other RBPs

Despite the simple, modular structure of the PUM RNA-binding domain, our data revealed considerable complexity in PUM1 and PUM2 interactions with RNA, due to base flipping, coupling, and binding in multiple modes and registers. These features are likely even more important for RBPs that lack a well-defined modular architecture. In fact, the requirement for more sophisticated models may explain the difficulty in obtaining sequence motifs for many RBPs, and the apparent degeneracy and redundancy of many of the hundreds of motifs that have been determined (e.g., Dominguez et al., 2018; Ray et al., 2013). Building on these motifs as starting points for rational library design and carrying out quantitative equilibrium measurements will be essential for developing predictive models of RBP interactions across all levels of RBP complexity.

### Functional Implications

The connection between PUM2 occupancy and its functional effects on mRNA abundance remains to be fully explored. Recent analysis of transcriptome-wide effects of PUM1 and PUM2 depletion showed that consensus sites located in 3' UTRs were more likely to give significant regulation than CDS sites (Bohn et al., 2018). Using our thermodynamic model to account for all sites (including nonconsensus sites) within each mRNA region supports this conclusion: PUM2 occupancy across 3' UTR sites was moderately predictive of mRNA upregulation in

response to PUM1 and PUM2 knockdown (Figure S7E; area under the curve [AUC], 0.63), whereas PUM2 occupancy across the CDS or 5' UTR regions was less predictive (AUC = 0.57). As a point of comparison, the eCLIP signal in the 3' UTR was similarly predictive of regulation as thermodynamically predicted PUM2 occupancy (AUC = 0.63; Figure S7F). The difference between functional outcomes from binding to 3' UTR versus non-3' UTR sites, despite indistinguishable PUM2 binding occupancies (Figure 6C), indicates the importance of additional cellular factors in determining the extent of PUM1- and PUM2-mediated repression.

The model further allows certain mRNAs to be confidently ruled out as direct PUM1 and PUM2 targets. In their study of global effects of PUM1 and PUM2 depletion on mRNA abundance, Bohn et al. observed a set of 300 mRNAs that were significantly downregulated, indicating a noncanonical role of Pumilio proteins in activating rather than repressing these targets (Bohn et al., 2018). Our thermodynamic model predicts that these mRNAs do not bind PUM1 and PUM2 significantly more than unregulated RNAs, suggesting that their expression is not controlled through direct interactions with Pumilio proteins. These genes may instead be regulated by factors that are themselves repressed by PUM1 and PUM2 (Figure S7G).

### Specificity and Cellular RNA-Protein-Binding Landscapes

Determining quantitative RBP binding landscapes and how these landscapes change with changes in RBP and RNA expression levels is critical for a complete description of the RBP-RNA networks. The shape of the binding landscape—i.e., RBP occupancies across RNA sequences present in a cell—has implications for regulation, evolution, and engineering. We illustrate some of these implications for PUM2.

The thermodynamic model predicts that less than a third of cellular PUM2 is bound to consensus sites and that the majority of the protein is distributed across nonconsensus sequences (Figure 6H; STAR Methods)—a consequence of the large excess of nonconsensus sites (Table S6) and the moderate binding penalties associated with many mutations and insertions (Table 1).

The varied, moderate nonconsensus residue penalties allow for a smooth gradient of PUM2 binding occupancies (Figure 6A; see also Figure 3F), and we speculate that this continuum of occupancies can be used to finely tune regulatory effects that occur through PUM2 binding.

A less obvious influence of RBP specificity on regulation arises because the binding to nonconsensus RNA sites reduces the pool of protein available to bind to consensus sites. Because of this titration effect and because of the much greater number of potential binding sites than the number of PUM2 molecules in cells, only a small fraction of each consensus site (UGUA [ACU]AUAN) is predicted to be occupied by protein (<10%, based on known amounts of cellular PUM2 and mRNA; STAR Methods). Thus, even in the presence of total protein concentration in excess of the consensus affinity ([PUM2] = 10 nM versus  $K_D = 3$  nM at 37°C), binding is decidedly subsaturating. This subsaturating binding renders per-site occupancies highly sensitive to changes in PUM2 levels or affinity, much as observed for

enzymes that operate in a subsaturating regime ( $[\text{substrate}] \sim K_M$ ) to enable greater sensitivity to cellular changes in substrate concentration (Berg and Stryer, 2002).

The near-continuous nature of PUM2 occupancies across mRNA sequences would be expected to render the PUM2-binding landscape highly evolvable. The presence of a large number of sites bound with moderate affinities, and the often-subtle effects of individual substitutions should allow evolution to both tune regulation of existing sites as well as co-opt binding sites for new regulation. Indeed, PUM2 orthologs throughout Eukarya recognize distinct sets of RNAs, and these transitions that occurred multiple times in evolution may have been facilitated by the moderate specificity of PUF proteins (Gerber et al., 2006; Hogan et al., 2015; Jiang et al., 2010).

Given the diversity of RBP properties and abundances (Singh et al., 2015), we expect considerable variation between occupancy landscapes of individual RBPs. For example, in contrast to the PUM2 example above, highly expressed RBPs ( $[\text{RBP}] \gg K_{D, \text{consensus}}$  and  $[\text{RBP}] \gg [\text{RNA}]_{\text{consensus}}$ ) will saturate their consensus sites, rendering binding insensitive to concentration changes and less discriminatory to nonconsensus sites. Quantitatively defining cellular RBP occupancy landscapes across diverse specificity and concentration regimes, their dynamic changes, and the biological consequences of these changes represents an intriguing challenge for future studies.

### Biophysical Insights into Pumilio-RNA Interactions

Our data revealed that the A-recognition modules (“R4”, “R6”, and “R8”; Figure 1A) give highly similar specificities, whereas the U-recognition modules (“R1”, “R3”, “R5”, and “R7”) vary dramatically in their specificities, from no discrimination against A and C at position 5 to  $\sim 10^2$ -fold specificity at positions 1 and 3 (Figures 2E and S7H–S7J). The differential specificity across the U-recognition modules could arise, at least in part, from differences in orientations and constraints imposed by the different neighboring positions, which can allow more or less optimal positioning at each U-recognition module. Similarly, the slightly weaker discrimination by the “R8” module, at the end of the PUM domain, relative to the internal A-recognition modules, may arise because there are fewer RNA conformational restraints 3' of this position, allowing noncognate bases to more readily find alternative bound conformations.

The absence of measurable coupling between most neighboring residues suggests that the orientation of entry of the RNA into a site is not generally affected by the identity of the neighboring residue. This observation suggests that cognate and noncognate residues are bound with similar backbone configurations (or ranges of backbone conformations), consistent with crystallographic observations that backbone trajectories leading into and out of Pumilio repeat sites are similar with cognate and noncognate bases (Gupta et al., 2008; Lu and Hall, 2011; Wang et al., 2009). More generally, the observed energetic independence between most adjacent RNA residues suggests sufficient room in the binding sites and/or sufficient degrees of freedom in the RNA backbone to allow the backbone to “forget” its specific interactions at the adjacent sites. Nevertheless, a subset of positions do exhibit coupling, and coupling is likely more prevalent for at least a subset of other RBPs.

Larger energetic effects are observed in cases of inserted residues that can flip away from the recognition sites (Figure 3D; Table 1). A residue that follows a flipped residue will experience a larger loss in conformational entropy upon docking than a residue that is positionally restricted by a preceding docked residue. Nevertheless, the specificity for neighbors is the same whether or not there is an intervening flipped residue—i.e., the same free energy terms can be used for each bound residue whether or not there is a flipped residue and associated flipping penalty. This constancy suggests that flipped residues do not significantly alter the docked states for neighboring cognate and noncognate residues and that there are no alternative bound states for the neighboring residues that are more favorable energetically than the standard docked state.

These observations are of practical importance for engineering PUF proteins and of broader importance for understanding and modeling RNA recognition by RBPs. Relative to DNA/protein interactions, more diverse conformational broader ensembles are expected for ssRNA, both bound and unbound to RBPs, highlighting the enormous challenge faced in modeling RNA-RBP binding affinities and specificities. Developing models that ultimately predict thermodynamics and binding landscapes for all RBPs we believe will require guidance and testing with large accurate thermodynamic datasets, such as those obtained herein.

### STAR★METHODS

Detailed methods are provided in the online version of this paper and include the following:

- KEY RESOURCES TABLE
- CONTACT FOR REAGENT AND RESOURCE SHARING
- METHOD DETAILS
  - Library design
  - Library preparation and sequencing
  - Protein expression and purification
  - Cy3B-labeling of SNAP-tagged proteins
  - RNA-MaP measurements
  - HPLC purification of RNA oligonucleotides for competition binding measurements
  - $[\gamma\text{-}^{32}\text{P}]$ -labeling of RNA oligonucleotides
  - Gel-shift binding measurements
- QUANTIFICATION AND STATISTICAL ANALYSIS
  - Computational analyses
  - Data filtering
  - Assessing reproducibility and combining experimental replicates
  - Assessing the significance of scaffold differences
  - Accounting for RNA structure
  - Assessing alternative binding registers in single mutant variants
  - Development, testing and evaluation of thermodynamic binding models
  - Analysis of *in vivo* crosslinking data
  - Enrichment of PUM2 sites within 3'UTRs
  - Modeling the cellular PUM2 binding landscape
  - Occupancy prediction algorithm

- Predicting PUM1 and PUM2-mediated regulation
- RNA Bind-n-Seq analysis
- DATA AND SOFTWARE AVAILABILITY

## SUPPLEMENTAL INFORMATION

Supplemental Information can be found online at <https://doi.org/10.1016/j.molcel.2019.04.012>.

## ACKNOWLEDGMENTS

We thank Wipapat Kladwang for outstanding technical assistance with emulsion PCR; Andre Gerber for PUM1 and PUM2 plasmids; Traci Hall for engineered PUM1 plasmid; Namita Bisaria, Greg Hogan, Julia Salzman, Erik Van Nostrand, and members of the Herschlag lab for helpful discussions and comments on the manuscript. This work was funded by NIH grants P01 GM066275 (D.H., R.D., and W.J.G.), R35 GM122579 (R.D.), and R01 GM121487 and R01 GM111990 (W.J.G.) and by the Beckman Center. W.J.G. acknowledges support as a Chan-Zuckerberg Investigator.

## AUTHOR CONTRIBUTIONS

Conceptualization, I.J., P.P.V., S.K.D., W.R.B., K.K., D.H., and W.J.G.; Performing Experiments, P.P.V., I.J., and R.S.; Formal Analysis, S.K.D., W.R.B., P.P.V., I.J., K.K., and V.S.; Resources (imaging station design, maintenance, and analysis tools), J.O.L.A. and C.J.L.; Writing – Original Draft: I.J., S.K.D., W.R.B., P.P.V., D.H., W.J.G.; Writing – Final Draft, I.J., S.K.D., W.R.B., P.P.V., K.K., J.O.L.A., C.J.L., V.S., R.S., R.D., D.H., and W.J.G.; Project Administration, D.H. and W.J.G.; Funding Acquisition, D.H., W.J.G., and R.D.

## DECLARATION OF INTERESTS

The authors declare no competing interests.

Received: September 13, 2018

Revised: January 31, 2019

Accepted: April 5, 2019

Published: May 8, 2019

## SUPPORTING CITATIONS

The following references appear in the Supplemental Information: Campbell et al. (2012), Elemento et al. (2007), Gasch et al. (2000), Kershaw et al. (2015), Lapointe et al. (2015), Morris et al. (2008), Riordan et al. (2011), and Wilinski et al. (2017).

## REFERENCES

Becker, W.R., Jarmoskaite, I., Kappel, K., Vaidyanathan, P.P., Denny, S.K., Das, R., Greenleaf, W.J., and Herschlag, D. (2019a). Quantitative high-throughput tests of ubiquitous RNA secondary structure prediction algorithms via RNA/protein binding. *bioRxiv*. <https://doi.org/10.1101/571588>.

Becker, W.R., Jarmoskaite, I., Vaidyanathan, P.P., Greenleaf, W.J., and Herschlag, D. (2019b). Demonstration of Protein Cooperativity Mediated by RNA Structure Using the Human Protein PUM2. *RNA* **118**, <https://doi.org/10.1261/rna.068585.118>.

Berg, J.M., and Stryer, L. (2002). *Biochemistry*, 5th edition (W H Freeman).

Bohn, J.A., Van Etten, J.L., Schagat, T.L., Bowman, B.M., McEachin, R.C., Fredolino, P.L., and Goldstrohm, A.C. (2018). Identification of diverse target RNAs that are functionally regulated by human Pumilio proteins. *Nucleic Acids Res.* **46**, 362–386.

Buenrostro, J.D., Araya, C.L., Chircus, L.M., Layton, C.J., Chang, H.Y., Snyder, M.P., and Greenleaf, W.J. (2014). Quantitative analysis of RNA-protein interactions on a massively parallel array reveals biophysical and evolutionary landscapes. *Nat. Biotechnol.* **32**, 562–568.

Campbell, Z.T., Bhimsaria, D., Valley, C.T., Rodriguez-Martinez, J.A., Menichelli, E., Williamson, J.R., Ansari, A.Z., and Wickens, M. (2012). Cooperativity in RNA-protein interactions: global analysis of RNA binding specificity. *Cell Rep.* **1**, 570–581.

Chen, Y., and Varani, G. (2013). Engineering RNA-binding proteins for biology. *FEBS J.* **280**, 3734–3754.

Cheong, C.G., and Hall, T.M. (2006). Engineering RNA sequence specificity of Pumilio repeats. *Proc. Natl. Acad. Sci. USA* **103**, 13635–13639.

Consortium, E.P.; ENCODE Project Consortium (2012). An integrated encyclopedia of DNA elements in the human genome. *Nature* **489**, 57–74.

Darnell, R.B. (2010). HITS-CLIP: panoramic views of protein-RNA regulation in living cells. *Wiley Interdiscip. Rev. RNA* **1**, 266–286.

Denny, S.K., Bisaria, N., Yesselman, J.D., Das, R., Herschlag, D., and Greenleaf, W.J. (2018). High-throughput investigation of diverse junction elements in RNA tertiary folding. *Cell* **174**, 377–390.e20.

Ding, Y., Tang, Y., Kwok, C.K., Zhang, Y., Bevilacqua, P.C., and Assmann, S.M. (2014). In vivo genome-wide profiling of RNA secondary structure reveals novel regulatory features. *Nature* **505**, 696–700.

Dominguez, D., Freese, P., Alexis, M.S., Su, A., Hochman, M., Palden, T., Bazile, C., Lambert, N.J., Van Nostrand, E.L., Pratt, G.A., et al. (2018). Sequence, structure, and context preferences of human RNA binding proteins. *Mol. Cell* **70**, 854–867.e859.

Elemento, O., Slonim, N., and Tavazoie, S. (2007). A universal framework for regulatory element discovery across all genomes and data types. *Mol. Cell* **28**, 337–350.

Fujioka, A., Terai, K., Itoh, R.E., Aoki, K., Nakamura, T., Kuroda, S., Nishida, E., and Matsuda, M. (2006). Dynamics of the Ras/ERK MAPK cascade as monitored by fluorescent probes. *J. Biol. Chem.* **281**, 8917–8926.

Galgano, A., Forrer, M., Jaskiewicz, L., Kanitz, A., Zavolan, M., and Gerber, A.P. (2008). Comparative analysis of mRNA targets for human PUF-family proteins suggests extensive interaction with the miRNA regulatory system. *PLoS ONE* **3**, e3164.

Gasch, A.P., Spellman, P.T., Kao, C.M., Carmel-Harel, O., Eisen, M.B., Storz, G., Botstein, D., and Brown, P.O. (2000). Genomic expression programs in the response of yeast cells to environmental changes. *Mol. Biol. Cell* **11**, 4241–4257.

Gerber, A.P., Herschlag, D., and Brown, P.O. (2004). Extensive association of functionally and cytotopically related mRNAs with Puf family RNA-binding proteins in yeast. *PLoS Biol.* **2**, E79.

Gerber, A.P., Luschnig, S., Krasnow, M.A., Brown, P.O., and Herschlag, D. (2006). Genome-wide identification of mRNAs associated with the translational regulator PUMILIO in *Drosophila melanogaster*. *Proc. Natl. Acad. Sci. USA* **103**, 4487–4492.

Goldstrohm, A.C., Hall, T.M.T., and McKenney, K.M. (2018). Post-transcriptional regulatory functions of mammalian Pumilio proteins. *Trends Genet.* **34**, 972–990.

Gründemann, D., and Schömig, E. (1996). Protection of DNA during preparative agarose gel electrophoresis against damage induced by ultraviolet light. *Biotechniques* **21**, 898–903.

Guo, J.U., and Bartel, D.P. (2016). RNA G-quadruplexes are globally unfolded in eukaryotic cells and depleted in bacteria. *Science* **353**, aaf5371.

Gupta, Y.K., Nair, D.T., Wharton, R.P., and Aggarwal, A.K. (2008). Structures of human Pumilio with noncognate RNAs reveal molecular mechanisms for binding promiscuity. *Structure* **16**, 549–557.

Hackermüller, J., Meisner, N.C., Auer, M., Jaritz, M., and Stadler, P.F. (2005). The effect of RNA secondary structures on RNA-ligand binding and the modifier RNA mechanism: a quantitative model. *Gene* **345**, 3–12.

Hafner, M., Landthaler, M., Burger, L., Khorshid, M., Hausser, J., Berninger, P., Rothballer, A., Ascano, M., Jr., Jungkamp, A.C., Munschauer, M., et al. (2010). Transcriptome-wide identification of RNA-binding protein and microRNA target sites by PAR-CLIP. *Cell* **141**, 129–141.

- Halstead, J.M., Lionnet, T., Wilbertz, J.H., Wippich, F., Ephrussi, A., Singer, R.H., and Chao, J.A. (2015). Translation. An RNA biosensor for imaging the first round of translation from single cells to living animals. *Science* *347*, 1367–1671.
- Harrow, J., Frankish, A., Gonzalez, J.M., Tapanari, E., Diekhans, M., Kokocinski, F., Aken, B.L., Barrell, D., Zadissa, A., Searle, S., et al. (2012). GENCODE: the reference human genome annotation for The ENCODE Project. *Genome Res.* *22*, 1760–1774.
- Heinz, S., Benner, C., Spann, N., Bertolino, E., Lin, Y.C., Laslo, P., Cheng, J.X., Murre, C., Singh, H., and Glass, C.K. (2010). Simple combinations of lineage-determining transcription factors prime cis-regulatory elements required for macrophage and B cell identities. *Mol. Cell* *38*, 576–589.
- Hogan, D.J., Riordan, D.P., Gerber, A.P., Herschlag, D., and Brown, P.O. (2008). Diverse RNA-binding proteins interact with functionally related sets of RNAs, suggesting an extensive regulatory system. *PLoS Biol.* *6*, e255.
- Hogan, G.J., Brown, P.O., and Herschlag, D. (2015). Evolutionary conservation and diversification of Puf RNA binding proteins and their mRNA targets. *PLoS Biol.* *13*, e1002307.
- Jain, N., Lin, H.C., Morgan, C.E., Harris, M.E., and Tolbert, B.S. (2017). Rules of RNA specificity of hnRNP A1 revealed by global and quantitative analysis of its affinity distribution. *Proc. Natl. Acad. Sci. USA* *114*, 2206–2211.
- Jankowsky, E., and Harris, M.E. (2017). Mapping specificity landscapes of RNA-protein interactions by high throughput sequencing. *Methods* *118–119*, 111–118.
- Jiang, H., Guan, W., and Gu, Z. (2010). Tinkering evolution of post-transcriptional RNA regulons: puf3p in fungi as an example. *PLoS Genet.* *6*, e1001030.
- Johnson, K.A., Simpson, Z.B., and Blom, T. (2009). Global kinetic explorer: a new computer program for dynamic simulation and fitting of kinetic data. *Anal. Biochem.* *387*, 20–29.
- Kedde, M., van Kouwenhove, M., Zwart, W., Oude Vrielink, J.A., Elkon, R., and Agami, R. (2010). A Pumilio-induced RNA structure switch in p27-3' UTR controls miR-221 and miR-222 accessibility. *Nat. Cell Biol.* *12*, 1014–1020.
- Keene, J.D., and Tenenbaum, S.A. (2002). Eukaryotic mRNPs may represent posttranscriptional operons. *Mol. Cell* *9*, 1161–1167.
- Kershaw, C.J., Costello, J.L., Talavera, D., Rowe, W., Castelli, L.M., Sims, P.F., Grant, C.M., Ashe, M.P., Hubbard, S.J., and Pavitt, G.D. (2015). Integrated multi-omics analyses reveal the pleiotropic nature of the control of gene expression by Puf3p. *Sci. Rep.* *5*, 15518.
- Kivioja, T., Vähärautio, A., Karlsson, K., Bonke, M., Enge, M., Linnarsson, S., and Taipale, J. (2011). Counting absolute numbers of molecules using unique molecular identifiers. *Nat. Methods* *9*, 72–74.
- Lambert, N., Robertson, A., Jangi, M., McGeary, S., Sharp, P.A., and Burge, C.B. (2014). RNA Bind-n-Seq: quantitative assessment of the sequence and structural binding specificity of RNA binding proteins. *Mol. Cell* *54*, 887–900.
- Lapointe, C.P., Wilinski, D., Saunders, H.A., and Wickens, M. (2015). Protein-RNA networks revealed through covalent RNA marks. *Nat. Methods* *12*, 1163–1170.
- Lee, S., Kopp, F., Chang, T.C., Sataluri, A., Chen, B., Sivakumar, S., Yu, H., Xie, Y., and Mendell, J.T. (2016). Noncoding RNA NORAD regulates genomic stability by sequestering PUMILIO proteins. *Cell* *164*, 69–80.
- Li, X., Quon, G., Lipshitz, H.D., and Morris, Q. (2010). Predicting in vivo binding sites of RNA-binding proteins using mRNA secondary structure. *RNA* *16*, 1096–1107.
- Lin, S.Y., and Riggs, A.D. (1972). Lac repressor binding to non-operator DNA: detailed studies and a comparison of equilibrium and rate competition methods. *J. Mol. Biol.* *72*, 671–690.
- Livesey, F.J. (2003). Strategies for microarray analysis of limiting amounts of RNA. *Brief. Funct. Genomics Proteomics* *2*, 31–36.
- Lorenz, R., Bernhart, S.H., Höner Zu Siederdissen, C., Tafer, H., Flamm, C., Stadler, P.F., and Hofacker, I.L. (2011). ViennaRNA Package 2.0. *Algorithms Mol. Biol.* *6*, 26.
- Lu, G., and Hall, T.M. (2011). Alternate modes of cognate RNA recognition by human PUMILIO proteins. *Structure* *19*, 361–367.
- Lu, G., Dolgner, S.J., and Hall, T.M. (2009). Understanding and engineering RNA sequence specificity of PUF proteins. *Curr. Opin. Struct. Biol.* *19*, 110–115.
- Marinov, G.K., Williams, B.A., McCue, K., Schroth, G.P., Gertz, J., Myers, R.M., and Wold, B.J. (2014). From single-cell to cell-pool transcriptomes: stochasticity in gene expression and RNA splicing. *Genome Res.* *24*, 496–510.
- Martin, L., Meier, M., Lyons, S.M., Sit, R.V., Marzluff, W.F., Quake, S.R., and Chang, H.Y. (2012). Systematic reconstruction of RNA functional motifs with high-throughput microfluidics. *Nat. Methods* *9*, 1192–1194.
- Miller, M.A., and Olivas, W.M. (2011). Roles of Puf proteins in mRNA degradation and translation. *Wiley Interdiscip. Rev. RNA* *2*, 471–492.
- Miller, M.T., Higgin, J.J., and Hall, T.M. (2008). Basis of altered RNA-binding specificity by PUF proteins revealed by crystal structures of yeast Puf4p. *Nat. Struct. Mol. Biol.* *15*, 397–402.
- Mitchell, S.F., and Parker, R. (2014). Principles and properties of eukaryotic mRNPs. *Mol. Cell* *54*, 547–558.
- Morris, A.R., Mukherjee, N., and Keene, J.D. (2008). Ribonomic analysis of human Pum1 reveals cis-trans conservation across species despite evolution of diverse mRNA target sets. *Mol. Cell Biol.* *28*, 4093–4103.
- Müller-McNicoll, M., and Neugebauer, K.M. (2013). How cells get the message: dynamic assembly and function of mRNA-protein complexes. *Nat. Rev. Genet.* *14*, 275–287.
- Nagaraj, N., Wisniewski, J.R., Geiger, T., Cox, J., Kircher, M., Kelso, J., Pääbo, S., and Mann, M. (2011). Deep proteome and transcriptome mapping of a human cancer cell line. *Mol. Syst. Biol.* *7*, 548.
- O'Leary, N.A., Wright, M.W., Brister, J.R., Ciufu, S., Haddad, D., McVeigh, R., Rajput, B., Robbertse, B., Smith-White, B., Ako-Adjei, D., et al. (2016). Reference sequence (RefSeq) database at NCBI: current status, taxonomic expansion, and functional annotation. *Nucleic Acids Res.* *44* (D1), D733–D745.
- Ray, D., Kazan, H., Cook, K.B., Weirauch, M.T., Najafabadi, H.S., Li, X., Gueroussov, S., Albu, M., Zheng, H., Yang, A., et al. (2013). A compendium of RNA-binding motifs for decoding gene regulation. *Nature* *499*, 172–177.
- Riordan, D.P., Herschlag, D., and Brown, P.O. (2011). Identification of RNA recognition elements in the *Saccharomyces cerevisiae* transcriptome. *Nucleic Acids Res.* *39*, 1501–1509.
- Rouault, T.A. (2006). The role of iron regulatory proteins in mammalian iron homeostasis and disease. *Nat. Chem. Biol.* *2*, 406–414.
- Rouskin, S., Zubradt, M., Washietl, S., Kellis, M., and Weissman, J.S. (2014). Genome-wide probing of RNA structure reveals active unfolding of mRNA structures in vivo. *Nature* *505*, 701–705.
- Schneider, T.D., and Stephens, R.M. (1990). Sequence logos: a new way to display consensus sequences. *Nucleic Acids Res.* *18*, 6097–6100.
- Schwahnhauser, B., Busse, D., Li, N., Dittmar, G., Schuchhardt, J., Wolf, J., Chen, W., and Selbach, M. (2013). Corrigendum: Global quantification of mammalian gene expression control. *Nature* *495*, 126–127.
- She, R., Chakravarty, A.K., Layton, C.J., Chircus, L.M., Andreasson, J.O., Damaraju, N., McMahon, P.L., Buenrostro, J.D., Jarosz, D.F., and Greenleaf, W.J. (2017). Comprehensive and quantitative mapping of RNA-protein interactions across a transcribed eukaryotic genome. *Proc. Natl. Acad. Sci. USA* *114*, 3619–3624.
- Singh, G., Pratt, G., Yeo, G.W., and Moore, M.J. (2015). The clothes make the mRNA: past and present trends in mRNP fashion. *Annu. Rev. Biochem.* *84*, 325–354.
- Sinha, R.P., and Häder, D.P. (2002). UV-induced DNA damage and repair: a review. *Photochem. Photobiol. Sci.* *1*, 225–236.
- Spitale, R.C., Flynn, R.A., Zhang, Q.C., Crisalli, P., Lee, B., Jung, J.W., Kuchelmeister, H.Y., Batista, P.J., Torre, E.A., Kool, E.T., and Chang, H.Y. (2015). Structural imprints in vivo decode RNA regulatory mechanisms. *Nature* *519*, 486–490.



- Stormo, G.D. (2000). DNA binding sites: representation and discovery. *Bioinformatics* *16*, 16–23.
- Sugimoto, Y., König, J., Hussain, S., Zupan, B., Curk, T., Frye, M., and Ule, J. (2012). Analysis of CLIP and iCLIP methods for nucleotide-resolution studies of protein-RNA interactions. *Genome Biol.* *13*, R67.
- Taliaferro, J.M., Lambert, N.J., Sudmant, P.H., Dominguez, D., Merkin, J.J., Alexis, M.S., Bazile, C., and Burge, C.B. (2016). RNA sequence context effects measured in vitro predict in vivo protein binding and regulation. *Mol. Cell* *64*, 294–306.
- Tang, F., Lao, K., and Surani, M.A. (2011). Development and applications of single-cell transcriptome analysis. *Nat. Methods* *8*, S6–S11.
- Thul, P.J., Åkesson, L., Wiking, M., Mahdessian, D., Geladaki, A., Ait Blal, H., Alm, T., Asplund, A., Björk, L., Breckels, L.M., et al. (2017). A subcellular map of the human proteome. *Science* *356*, eaal3321.
- Tome, J.M., Ozer, A., Pagano, J.M., Gheba, D., Schroth, G.P., and Lis, J.T. (2014). Comprehensive analysis of RNA-protein interactions by high-throughput sequencing-RNA affinity profiling. *Nat. Methods* *11*, 683–688.
- Ule, J., Jensen, K.B., Ruggiu, M., Mele, A., Ule, A., and Darnell, R.B. (2003). CLIP identifies Nova-regulated RNA networks in the brain. *Science* *302*, 1212–1215.
- Vaidyanathan, P.P., AlSadhan, I., Merriman, D.K., Al-Hashimi, H.M., and Herschlag, D. (2017). Pseudouridine and  $N^6$ -methyladenosine modifications weaken PUF protein/RNA interactions. *RNA* *23*, 611–618.
- Valley, C.T., Porter, D.F., Qiu, C., Campbell, Z.T., Hall, T.M., and Wickens, M. (2012). Patterns and plasticity in RNA-protein interactions enable recruitment of multiple proteins through a single site. *Proc. Natl. Acad. Sci. USA* *109*, 6054–6059.
- Van Nostrand, E.L., Pratt, G.A., Shishkin, A.A., Gelboin-Burkhart, C., Fang, M.Y., Sundararaman, B., Blue, S.M., Nguyen, T.B., Surka, C., Elkins, K., et al. (2016). Robust transcriptome-wide discovery of RNA-binding protein binding sites with enhanced CLIP (eCLIP). *Nat. Methods* *13*, 508–514.
- Wang, X., McLachlan, J., Zamore, P.D., and Hall, T.M. (2002). Modular recognition of RNA by a human pumilio-homology domain. *Cell* *110*, 501–512.
- Wang, Y., Opperman, L., Wickens, M., and Hall, T.M. (2009). Structural basis for specific recognition of multiple mRNA targets by a PUF regulatory protein. *Proc. Natl. Acad. Sci. USA* *106*, 20186–20191.
- Wheeler, E.C., Van Nostrand, E.L., and Yeo, G.W. (2018). Advances and challenges in the detection of transcriptome-wide protein-RNA interactions. *Wiley Interdiscip. Rev. RNA* *9*, e1436.
- Wiliński, D., Qiu, C., Lapointe, C.P., Nevil, M., Campbell, Z.T., Tanaka Hall, T.M., and Wickens, M. (2015). RNA regulatory networks diversified through curvature of the PUF protein scaffold. *Nat. Commun.* *6*, 8213.
- Wiliński, D., Buter, N., Klocko, A.D., Lapointe, C.P., Selker, E.U., Gasch, A.P., and Wickens, M. (2017). Recurrent rewiring and emergence of RNA regulatory networks. *Proc. Natl. Acad. Sci. USA* *114*, E2816–E2825.
- Williams, R., Peisajovich, S.G., Miller, O.J., Magdassi, S., Tawfik, D.S., and Griffiths, A.D. (2006). Amplification of complex gene libraries by emulsion PCR. *Nat. Methods* *3*, 545–550.
- Xue, Y., Zhou, Y., Wu, T., Zhu, T., Ji, X., Kwon, Y.S., Zhang, C., Yeo, G., Black, D.L., Sun, H., et al. (2009). Genome-wide analysis of PTB-RNA interactions reveals a strategy used by the general splicing repressor to modulate exon inclusion or skipping. *Mol. Cell* *36*, 996–1006.
- Zerbino, D.R., Achuthan, P., Akanni, W., Amode, M.R., Barrell, D., Bhai, J., Billis, K., Cummins, C., Gall, A., Girón, C.G., et al. (2018). Ensembl 2018. *Nucleic Acids Res.* *46* (D1), D754–D761.

## STAR★METHODS

## KEY RESOURCES TABLE

REAGENT or RESOURCE	SOURCE	IDENTIFIER
<b>Bacterial and Virus Strains</b>		
BL21(DE3) competent cells	Agilent	Cat#200131
BL21-CodonPlus (DE3)-RIPL competent cells	Agilent	Cat#230280
<b>Chemicals, Peptides and Recombinant Proteins</b>		
SNAP-hPUM2	This paper	N/A
hPUM1-SNAP	This paper	N/A
hPUM1 MUT3-1-SNAP	This paper	N/A
His-TEV Protease	This paper	N/A
cOmplete, Mini, EDTA-free Protease Inhibitor Cocktail	Sigma-Aldrich	Cat#11836153001
Cy3B NHS ester	GE Healthcare	Cat#PA63100
BG-NH2	New England Biolabs (NEB)	Cat#S9148S
Agencourt AMPure XP beads	Beckman Coulter	Cat#A63881
SYBR Green I Nucleic Acid Stain	Lonza	Cat#50513
SYBR Gold Nucleic Acid Gel Stain	Invitrogen	Cat#S11494
Phusion High-Fidelity DNA Polymerase	Thermo Fisher Scientific	Cat#F530S
Phusion Hot Start II DNA Polymerase	Thermo Fisher Scientific	Cat#F549
Klenow fragment (3'-5' exo(-))	NEB	Cat#M0212L
Streptavidin	PROzyme	Cat#SA10
D-Biotin	Thermo Fisher Scientific	Cat#B20656
<i>E. coli</i> RNA polymerase holoenzyme	NEB	Cat#M0551S
Low Molecular Weight DNA Ladder	NEB	Cat#N3233S
T4 Polynucleotide Kinase	Thermo Fisher Scientific	Cat#EK0031
Gamma-32P ATP	Perkin Elmer	Cat#NEG035C
Bovine Serum Albumin	NEB	Cat#B9000S
<b>Critical Commercial Assays</b>		
MiSeq Reagent Kit v3 (150-cycle)	Illumina	Cat#MS-102-3001
PhiX Control V3	Illumina	Cat#FC-110-3001
QIAquick Gel Extraction Kit	QIAGEN	Cat#28704
MinElute PCR Purification Kit	QIAGEN	Cat#28004
QIAquick PCR Purification Kit	QIAGEN	Cat#28106
Zeba Spin Desalting Columns 7K MWCO, 5 mL	Thermo Fisher Scientific	Cat#89892
Amicon Ultra-4 Centrifugal Filter Unit, 3KDa	Millipore Sigma	Cat#UFC800324
Amicon Ultra-0.5 Centrifugal Filter Unit, 10KDa	Millipore Sigma	Cat#UFC501024
<b>Oligonucleotides</b>		
DNA oligonucleotide library, see <a href="#">Table S5</a>	CustomArray, this Study	N/A
DNA oligonucleotides used for library assembly and RNA array preparation, see <a href="#">Table S7</a>	IDT	N/A
RNA oligonucleotides used in gel-shift measurements, see <a href="#">STAR Methods</a>	IDT	N/A
<b>Deposited data</b>		
RNA-seq expression data for K562 cell lines	ENCODE project (Consortium, 2012)	<a href="https://www.encodeproject.org/files/ENCFF272HJP/@download/ENCFF272HJP.tsv">https://www.encodeproject.org/files/ENCFF272HJP/@download/ENCFF272HJP.tsv</a> , <a href="https://www.encodeproject.org/files/ENCFF471SEN/@download/ENCFF471SEN.tsv">https://www.encodeproject.org/files/ENCFF471SEN/@download/ENCFF471SEN.tsv</a>

(Continued on next page)

**Continued**

REAGENT or RESOURCE	SOURCE	IDENTIFIER
eCLIP data for PUM2 protein in human K562 cells	(Consortium, 2012; Van Nostrand et al., 2016)	<a href="https://www.encodeproject.org/files/ENCFF786ZZB/@download/ENCFF786ZZB.bam">https://www.encodeproject.org/files/ENCFF786ZZB/@download/ENCFF786ZZB.bam</a> , <a href="https://www.encodeproject.org/files/ENCFF732EQX/@download/ENCFF732EQX.bam">https://www.encodeproject.org/files/ENCFF732EQX/@download/ENCFF732EQX.bam</a> , <a href="https://www.encodeproject.org/files/ENCFF231WHF/@download/ENCFF231WHF.bam">https://www.encodeproject.org/files/ENCFF231WHF/@download/ENCFF231WHF.bam</a> <a href="https://www.encodeproject.org/files/ENCFF141SVY/@download/ENCFF141SVY.bed.gz">https://www.encodeproject.org/files/ENCFF141SVY/@download/ENCFF141SVY.bed.gz</a> <a href="https://www.encodeproject.org/files/ENCFF141SVY/@download/ENCFF141SVY.bed">https://www.encodeproject.org/files/ENCFF141SVY/@download/ENCFF141SVY.bed</a>
Refseq annotations for human genome assembly GRCh38 (hg38)	(O'Leary et al., 2016)	<a href="https://www.ncbi.nlm.nih.gov/refseq/">https://www.ncbi.nlm.nih.gov/refseq/</a>
Protein-coding transcript sequences, genome release GRCh38.p12	(Harrow et al., 2012)	<a href="https://www.encodegenes.org/human/release_28.html">https://www.encodegenes.org/human/release_28.html</a>
RNA Bind-N-Seq data for PUM1	(Consortium, 2012; Dominguez et al., 2018)	<a href="https://www.encodeproject.org/files/ENCFF894MLG/">https://www.encodeproject.org/files/ENCFF894MLG/</a> <a href="https://www.encodeproject.org/files/ENCFF761JAF/(input)">https://www.encodeproject.org/files/ENCFF761JAF/(input)</a>
<b>Software and Algorithms</b>		
RNAfold, v2.1.8, v2.1.9	(Lorenz et al., 2011)	<a href="https://www.tbi.univie.ac.at/RNA/RNAfold.1.html">https://www.tbi.univie.ac.at/RNA/RNAfold.1.html</a>
Bedtools		<a href="https://bedtools.readthedocs.io/en/latest/">https://bedtools.readthedocs.io/en/latest/</a>
HOMER (v4.8.3)	(Heinz et al., 2010)	<a href="http://homer.ucsd.edu/homer/">http://homer.ucsd.edu/homer/</a>
Ensembl Biomart	(Zerbino et al., 2018)	<a href="http://ensembl.org">http://ensembl.org</a>
Samtools (v0.1.19-96b5f2294a)		<a href="http://www.htslib.org/">http://www.htslib.org/</a>
pyatac ins		<a href="https://nucleoatac.readthedocs.io/en/latest/pyatac/">https://nucleoatac.readthedocs.io/en/latest/pyatac/</a>
Global fitting scripts to determine PUM2 thermodynamic model parameters	This paper	<a href="https://github.com/pufmodel/PUM2_global_fitting">https://github.com/pufmodel/PUM2_global_fitting</a>
Pipeline for comparing <i>in vivo</i> to <i>in vitro</i> occupancy across genomic sites	This paper	<a href="https://github.com/GreenleafLab/pufflibs/blob/master/analyze_clip_data.py">https://github.com/GreenleafLab/pufflibs/blob/master/analyze_clip_data.py</a>
Pipeline for fitting thermodynamic constants from fluorescence data	This paper	<a href="https://github.com/GreenleafLab/array_fitting_tools/">https://github.com/GreenleafLab/array_fitting_tools/</a>

**CONTACT FOR REAGENT AND RESOURCE SHARING**

Further information and requests for resources and reagents should be directed to and will be fulfilled by the Lead Contact, Daniel Herschlag ([herschla@stanford.edu](mailto:herschla@stanford.edu)).

**METHOD DETAILS****Library design**

Summary of library designs and complete sequence information is provided in [Table S5](#).

**Library preparation and sequencing****Ordering**

DNA constructs consisting of the PUF library and short constant regions for subsequent PCR assembly ([Figure S1D](#) & [Table S7](#); 5'-TGATGGAAGACGTTCCCTGGATCC-[Variable region]-AGATCGGAAGAGCGGTTTCAG-3') were ordered from CustomArray, Inc. as part of a 90,000 oligo pool of 130 nt sequences. Each of the 34,927 unique sequences in the library (including variants not discussed herein) was included at least in duplicate to increase the probability of error-free generation. In cases where the designed sequence was shorter than 130 nt, the construct was "padded" at the 3' end with a random sequence that was eliminated during PCR assembly. Primers and DNA oligonucleotides used in the RNA-MaP protocol were ordered from Integrated DNA Technologies (IDT).

**Emulsion PCR**

The oligonucleotide pool was amplified using emulsion PCR (ePCR) ([Williams et al., 2006](#)), allowing us to decrease length and other biases during PCR amplification of our highly diverse library (lengths of 64–130 nt, variable structure content). We closely followed a MYcroarray adaptation of the ePCR protocol from ([Williams et al., 2006](#)), as detailed below. Flat-bottom glass vials (1 mL) were

cleaned with sterile water, dried, covered with parafilm, and frozen in a Petri dish filled with sterile water. The oil phase was prepared from 4% (v/v) ABIL EM-90, 0.05% (v/v) Triton X-100 and 96% (v/v) mineral oil. The 50  $\mu$ L aqueous phase consisted of 1.45 ng/ $\mu$ L of the CustomArray oligo pool, 0.2 mM dNTPs, 1  $\mu$ L of Phire Hot Start II DNA Polymerase (Thermo Fisher Scientific), 1x Phire II buffer, 0.5 mg/mL bovine serum albumin (BSA), and 2  $\mu$ M of each of *RNAPstall* and *Read2* primers (Table S7 and Figure S1D). A 300  $\mu$ L aliquot of the vortexed, pre-chilled oil phase was added to the glass vial embedded in the ice-filled Petri dish and stirred on a stir plate with a sterile magnetic bar at 1000 rpm for 5 min. The aqueous phase was then added in five 10  $\mu$ L aliquots and stirred for another 10 min. The emulsion was divided between seven PCR tubes and amplified for 40 cycles of 98°C for 10 s, 65°C for 10 s, and 72°C for 30 s. Completed PCR reactions were pooled in a 1.7 mL Eppendorf tube, and 1  $\mu$ L of gel loading dye was added to visualize the aqueous phase. Mineral oil (100  $\mu$ L) was added and the mix was vortexed for 30 s, followed by centrifugation for 10 min at 13,000 g. The oil was discarded and 1 mL diethyl ether was added, the mixture was vortexed in a fume hood for 3 min and centrifuged for 1 min at 13,000 g. Diethyl ether was discarded, 1 mL ethyl acetate was added, and the mixture was vortexed in a fume hood for 3 min and centrifuged for 1 min at 13,000 g. Ethyl acetate was removed and the diethyl ether extraction step was repeated, followed by discarding the diethyl ether. The tube was incubated for 5 min at 37°C with an open cap to allow residual diethyl ether to evaporate. Water (40  $\mu$ L) and Agencourt AMPure XP beads (Beckman Coulter; 72  $\mu$ L) were added and incubated for 15 min at room temperature; the supernatant was removed, the beads were washed with 70% ethanol (2  $\times$  100  $\mu$ L), dried, and the DNA was eluted in 10.5  $\mu$ L water.

### Size fractionation

To further prevent bias toward short oligonucleotides during the subsequent PCR assembly steps, the ePCR-amplified library was fractionated by length on an 8% polyacrylamide gel. Following SYBR Green staining (1x; Lonza), the library-containing lane was covered with aluminum foil to prevent UV-induced damage (Gründemann and Schömgig, 1996; Sinha and Häder, 2002), and divided into 6 fractions based on UV visualization of marker lanes. The cut-out bands were frozen on dry ice and eluted overnight in TE buffer (10 mM Tris·HCl, pH 8.0, 1 mM Na<sub>2</sub>EDTA) on a rotating platform at 8°C. The DNA was purified using the QIAGEN Gel Extraction Kit (using a protocol adapted for PAGE purification: <http://www.qiagen.com/kr/resources/resourcedetail?id=1426dbb4-da09-487c-ae01-c587c2be14c3&lang=en>, with QIAGEN MinElute columns). To remove residual co-purified short fragments, each fraction was re-purified on an 8% denaturing gel (8 M urea). For denaturing PAGE, the samples and a Low-MW DNA ladder (New England Biolabs; NEB) were heated in loading buffer (84% (v/v) formamide, 50 mM Na<sub>2</sub>EDTA, 0.04% Xylene cyanol, 0.04% Bromophenol blue (BPB); 2.8  $\mu$ L loading buffer per 5  $\mu$ L sample) at 90°C for 3 min immediately before loading. The gel was stained with SYBR Gold, the library-containing lanes were covered with aluminum foil and fractions were cut out based on UV visualization of marker lanes. (Additional lanes with 83 nt and 129 nt DNA oligonucleotides were used to facilitate alignment of the NEB low-MW marker with desired lengths.) The DNA was extracted from the gel as above and eluted in QIAGEN EB buffer with 0.1% Tween-20. Purified fractions were re-amplified using the *Read2* and *RNAPstall\_adapt* primers (Table S7). The PCR reactions (25  $\mu$ L) consisted of 2.5  $\mu$ L of the purified library fractions, 0.5  $\mu$ M of each primer, 0.2 mM dNTPs, 3% DMSO, 0.02 U/ $\mu$ L Phusion HF Polymerase (Thermo Fisher Scientific), and 1x Phusion HF buffer. The reactions proceeded for 15–23 cycles of 98°C for 10 s, 63°C for 20 s, and 72°C for 20 s and were purified using QIAGEN MinElute PCR Purification Kit. In all cases here and below, the number of PCR cycles was determined by quantitative PCR (qPCR), using the same primer and template concentrations as in preparative PCR, but in the presence of 0.2–0.5x SYBR Green. To prevent accumulation of by-products, cycle numbers corresponding to about one-third saturation ( $C_t$  value) were used in preparative PCR reactions. Each library fraction was amplified for two to three different numbers of cycles around the  $C_t$  value, and only reactions lacking high-molecular weight byproducts were propagated to the next step.

### PCR assembly

Each purified length fraction was assembled into the final RNA array construct with the *C\_read1\_bc\_RNAP*, *D\_read2*, *OligoC* and *OligoD* primers, as illustrated in Figure S1D (see Table S7 for primer sequences). The *C\_read1\_bc\_RNAP* primer contained a randomized 15 nt 'barcode' region that served as a unique molecular identifier (UMI) and allowed high-confidence sequence mapping during subsequent steps (Buenrostro et al., 2014). The PCR reactions consisted of 0.5 nM of the amplified library fractions, 1.5 nM of *C\_read1\_bc\_RNAP* primer, 1.5 nM of *D\_read2* primer, 0.5  $\mu$ M of *Oligo C* and *Oligo D* primers, 0.2 mM dNTPs, 3% DMSO, 1x Phusion HF buffer, and 0.01 U/ $\mu$ L Phusion HF Polymerase. The reactions proceeded for 18 cycles of 98°C for 10 s, 63°C for 30 s, and 72°C for 30 s, and the PCR products were purified using QIAquick PCR purification kit (QIAGEN).

### Bottlenecking

To ensure that multiple copies of each UMI were present on the RNA array, the library was bottlenecked to  $\sim$ 700,000 total molecules (Buenrostro et al., 2014; Denny et al., 2018; Kivioja et al., 2011). UMI redundancy allows distinguishing between sequencing errors and real sequence differences, as errors are unlikely to co-occur in both the UMI and the variable region (see **Computational analyses** below). To bottleneck, the PCR products were quantified by qPCR relative to the PhiX standard (Illumina). As noted above, the six 'sublibraries', corresponding to the different oligonucleotide lengths in our library, were kept separate during all pre-sequencing PCR steps to minimize bias in the final library assayed by RNA-Map. Dilutions of 1000-fold and 10,000-fold for each fraction were prepared in 0.1% Tween-20. The PhiX standard (Illumina) was diluted to 200 pM and seven serial dilutions were prepared in 0.1% Tween-20. The DNA was then added to a PCR master mix containing 500 nM *OligoC* and *OligoD* primers, 200  $\mu$ M dNTP mix, 0.5x SYBR Green, 3% DMSO, 0.02 U/ $\mu$ L Phusion DNA Polymerase, and 1x Phusion buffer. The PCR reactions proceeded for 35 cycles of 98°C for 10 s, 63°C for 30 s, and 72°C for 30 s. The library concentrations were determined based on the PhiX standard curve of  $C_t$  values over concentration (determined in duplicate). The volumes corresponding to a total of 700,000 molecules across

all sublibraries were calculated, and each sublibrary was amplified with *OligoC* and *OligoD* primers. The PCR reactions contained 1.1–5.3 fM of individual sublibraries (in 0.1% Tween-20), 500 nM *OligoC* and *OligoD* primers, 200  $\mu$ M dNTP mix, 3% DMSO, 1x Phusion buffer, and 0.01 U/ $\mu$ L Phusion DNA Polymerase. The reactions proceeded for 23 cycles of 98°C for 10 s, 63°C for 30 s, and 72°C for 30 s, and the PCR products were purified with QIAquick PCR cleanup kit (QIAGEN). Concentrations of 1000-fold dilutions were quantified by qPCR, and the different sublibraries were combined for sequencing. Due to a short *OligoD* byproduct detected as dominant species in the initial sequencing of our library, the bottlenecked library fractions were re-purified on a denaturing 8% acrylamide gel and amplified using Phusion Hot Start II DNA Polymerase (Thermo Fisher Scientific) instead of regular Phusion, which eliminated the primer byproduct. This library was sequenced and used in all RNA-MaP experiments reported herein.

#### **Fiduciary marker preparation**

To facilitate RNA array image alignment and quantification, we included a fiduciary marker oligonucleotide in our RNA array library sample prior to sequencing (see below). This oligonucleotide resembled the library constructs, except for lacking the barcode, RNAP promoter and RNAP start/stall regions and was PCR-assembled separately using an analogous series of steps. The final sequence of the fiduciary oligo consisted of [C\_adapter][Read1] CTT GGG TCC ACA GGA CAC TCG TTG CTT TCC [Read2][D'\_adapter] (*Fiducial\_chip*, Table S7).

#### **Sequencing**

The bottlenecked, qPCR-quantified library fractions were combined and sequenced using MiSeq Reagent Kit v3 (150-cycle; 56 nt in Read 1, 96 nt in Read 2). To ensure appropriate density of RNA clusters in the RNA-MaP experiments, our library constituted 9%–15% of the total 6–9.6 fmol DNA. The remaining DNA consisted of 84%–90% PhiX DNA and 1% of the fiduciary marker oligonucleotide (*Fiducial\_chip*, Table S7). The final numbers of transcribable clusters were  $3.6 \times 10^5$ – $6.5 \times 10^5$  on the sequencing chips used in this study.

#### **Protein expression and purification**

The RNA-binding domains of *H. sapiens* PUM1 (828-1176; isoform 2), PUM2 (706-1059; isoform 1), and mutant PUM1 (MUT3-1 in (Cheong and Hall, 2006)) (828-1176) were cloned into a custom pET28a-based expression vector in frame with an N-terminal His-tag and a SNAP tag (New England Biolabs) at either the N- (PUM2) or C terminus (hPUM1 and hPUM1 MUT3-1; primers and plasmid sequences available upon request). Constructs were sequenced and transformed into *E. coli* protein expression strains BL21 (DE3) or RIPL BL21 CodonPlus (Agilent). Protein expression was induced at an OD600 of between 0.6–0.8 with 0.5–1 mM IPTG at 18–20°C for 18–20 h. Cell pellets were lysed four times using an Emulsiflex (Avestin) in Buffer A containing 20 mM Na-HEPES, pH 7.4, 500 mM potassium acetate (KOAc), 5% glycerol, 0.2% Tween-20, 10 mM imidazole, 2 mM dithiothreitol (DTT), 1 mM phenylmethylsulfonyl fluoride (PMSF) and 2X Complete Mini protease inhibitor cocktail (Roche). The lysate was centrifuged at 20,000 g for 20 min to remove membranes and unlysed cells. Nucleic acids in the lysate were precipitated with dropwise addition of Polyethylene Imine (Sigma) to a final concentration of 0.21% (v:v) with constant stirring at 4°C and pelleted by centrifugation at 20,000 g for 20 min. Cleared lysates were then loaded on a Nickel-chelating HisTrap HP column (GE), washed extensively, and His-tagged proteins were eluted over a 10–500 mM imidazole gradient. Protein fractions were pooled and desalted into Buffer B (20 mM Na-HEPES, pH 7.4, 50 mM KOAc, 5% glycerol, 0.1% Tween-20, 2 mM DTT) using a HiPrep 26/10 desalting column. The His-tag was removed by incubation with TEV protease for 13–16 h at 4°C, and the protein solution was loaded for a second time on the HisTrap HP column. The flow-through containing cleaved protein was collected and subsequently desalted into Buffer B. The protein was then loaded on a Heparin or HiQ column and eluted over a linear gradient of KOAc from 50 to 1000 mM. Fractions were pooled and desalted into Buffer C containing 20 mM Na-HEPES, pH 7.4, 100 mM KOAc, 5% glycerol, 0.1% Tween-20 and 2 mM DTT, concentrated using Amicon Ultra-0.5 10KDa filters and diluted two-fold with Buffer C containing 80% glycerol for final storage at –20°C. SDS-PAGE gels of final purified protein constructs are shown in Figure S7K.

#### **Cy3B-labeling of SNAP-tagged proteins**

Cy3B-labeled SNAP tag substrate was prepared by coupling Cy3B NHS ester (GE Healthcare, 0.75  $\mu$ mol) with 1.5-fold excess (1.13  $\mu$ mol) of amine-terminated benzylguanine (NH<sub>2</sub>-BG; New England BioLabs) in the presence of 1.13  $\mu$ mol triethylamine in dimethylformamide. The reaction (103  $\mu$ L) was incubated overnight on a rotating platform at 30°C. The Cy3B-BG product was purified by reverse phase HPLC on an Agilent ZORBAX Eclipse Plus 95Å column and dried by speed-vac evaporation (46% yield).

SNAP-tagged PUF proteins were labeled by incubating 5–10  $\mu$ M of purified protein with 20  $\mu$ M of Cy3B-BG in Buffer C. The tube was covered with aluminum foil and rotated at 4°C for 12–14 h. Unincorporated dye was removed with Zeba Spin Desalting Columns (Thermo Fisher Scientific) equilibrated with Buffer C; the protein was concentrated using Amicon Ultra 10KDa filters and diluted two-fold with Buffer C containing 80% glycerol for final storage at –20°C. The labeling efficiencies (based on total protein concentration and Cy3B absorbance at 559 nm; Cy3B extinction coefficient:  $130,000 \text{ M}^{-1}\text{cm}^{-1}$ ) were 60% (PUM2-SNAP), 53% (SNAP-PUM1) and 36% (mutant SNAP-PUM1).

#### **RNA-MaP measurements**

##### **Imaging station setup**

The RNA-MaP imaging platform was built out of a repurposed Illumina GAIIX instrument with custom-designed additions as described in (Buenrostro et al., 2014; Denny et al., 2018; She et al., 2017). Briefly, the custom additions included a fluidics

adaptor interface to pump reagents to the MiSeq flow cell, a Peltier-based temperature-controlled platform to house the flow cell, an autosampler with 96-well cooling block for RNA-MaP reagents, and a dual-color laser excitation system. Two lasers were employed: a 660 nm ‘red’ laser with a 664 nm long pass filter and a 530 nm ‘green’ laser with a 590 nm band pass filter. MATLAB scripts developed in-house were used to control the fluidics, temperature, position, and imaging of the flow cell. Flow cell images were acquired with 400 ms exposures at 200 mW laser power. Camera focal distances were determined through iterative rounds of imaging of the flow cell and adjustment of the camera’s z-position.

### **RNA transcription in the flow cell**

Using the imaging station fluidics system, the flow cell was washed with 5 mM Na<sub>2</sub>EDTA in formamide to remove hybridized DNA (250 μL flowed at 100 μL/min, 55°C), followed by Reducing buffer (100 mM Tris·HCl, 125 mM NaCl, 0.05% Tween-20, 100 mM Tris[2-Carboxyethyl]phosphine-HCl (TCEP), pH 7.4) to remove any residual fluorescence from the sequencing reaction (390 μL, 10 min at 60°C). A fluorescent probe complementary to the RNA Polymerase stall sequence (*Fluorescent\_stall'*; sequences of oligonucleotides used in the RNA-MaP protocol are indicated in [Table S7](#)) was then annealed to the library and imaged to determine the efficiency of the cleaning steps (500 nM *Fluorescent\_stall'* in Annealing buffer: 1x SSC buffer, 7 mM MgCl<sub>2</sub>, 0.01% Tween-20; 11 min at 37°C). After imaging, the fluorescent probe was removed by washing with 250 μL of 100% formamide (55°C). The flow cell was washed with Wash buffer between steps (290 μL; 10 mM Tris·HCl, pH 8.0, 5 mM Na<sub>2</sub>EDTA, pH 8.0, 0.05% Tween-20). Henceforth, wash steps were performed with a 250 μL volume of the specified buffer, unless otherwise noted.

To prepare double-stranded DNA (dsDNA), 5′-biotinylated primer (*Biotin\_D\_Read2*, 500 nM) was annealed to the library in Hybridization buffer (5x SSC buffer, 5 mM Na<sub>2</sub>EDTA, 0.05% Tween-20) for 15 min at 60°C followed by a 10 min incubation at 40°C. The fluorescent oligonucleotide complementary to the fiducial marker (*Fiducial\_flow*) was also included in the hybridization mixture at 250 nM. After washing the flow cell with Annealing buffer, an additional 500 nM of *Biotin\_D\_Read2* (and 250 nM *Fiducial\_flow*) was annealed to the library in Annealing buffer at 37°C for 8 min. The flow cell was then washed with Klenow buffer (1x NEB buffer 2 (NEB B7002S), 250 μM each dNTP, 0.01% Tween-20). Double-stranded DNA was generated by pumping 130 μL of 0.1 U/μL Klenow fragment (3′-5′ exo(-); NEB M0212L) into the flow cell in three stages separated by 10 min intervals each. The flow cell was maintained at 37°C for this period. Unextended single-stranded DNA templates were subsequently blocked by annealing a non-fluorescent version of the stall probe (*Dark\_stall'*) in a process identical to the one described above.

After dsDNA generation, 1 μM streptavidin in Annealing buffer was pumped into the flow cell and allowed to bind to the biotinylated primer for 5 min at 37°C. Excess streptavidin was then washed out of the flow cell with Annealing buffer. Unbound biotin binding sites in the streptavidin tetramer were saturated by incubating the flow cell for 5 min with 5 μM free biotin in Annealing buffer. Excess unbound biotin was washed out with Annealing buffer.

RNA transcription proceeded in two stages, initiation/stall and extension. In the initiation/stall phase, 130 μL of 0.06 U/μL *E. coli* RNA polymerase holoenzyme (RNAP; NEB M0551S) was allowed to initiate transcription for 20 min at 37°C on the dsDNA templates in Initiation buffer, which lacked CTP (20 mM Tris·HCl pH 8.0, 7 mM MgCl<sub>2</sub>, 20 mM NaCl, 0.1% 2-Mercaptoethanol (BME), 0.1 mM Na<sub>2</sub>EDTA, 1.5% glycerol, 0.02 mg/mL BSA, 0.01% Tween-20, and 2.5 μM each of ATP, GTP, and UTP). Upon encountering the first cytosine (C27), the polymerase stalls, thereby sterically preventing the loading of additional enzymes on the same template ([Buenrostro et al., 2014](#)). Excess RNAP was washed out of the flow cell with Initiation buffer. Subsequently, Extension buffer was added, which contained all 4 ribonucleotides (20 mM Tris·HCl pH 8.0, 7 mM MgCl<sub>2</sub>, 20 mM NaCl, 0.1% BME, 0.1 mM Na<sub>2</sub>EDTA, 1.5% glycerol, 0.02 mg/mL BSA, 0.01% Tween-20, and 1 mM each of ATP, GTP, UTP and CTP). The Extension buffer also contained 500 nM each of *Fluorescent\_stall'* and *Dark\_read2* oligonucleotides, which were intended to block the regions flanking the variable region in the nascent RNA transcript ([Figure 1C](#)) and to prevent undesired intramolecular interactions, as well as to allow visualization of the transcript. Transcription was allowed to proceed for 10 min at 37°C. RNA polymerase eventually stalls at the streptavidin roadblock at the end of the DNA template, exposing the nascent RNA molecules for binding experiments ([Figure 1C](#)).

To ensure complete blocking of RNA regions flanking the variable sequence, transcription was followed by further hybridization of *Fluorescent\_stall'* and *Dark\_read2* oligonucleotides (500 nM) for 10 min at 37°C in Annealing buffer. Finally, the flow cell was washed with Binding buffer (20 mM Na-HEPES, pH 7.4, 100 mM KOAc, 0.1% Tween-20, 5% glycerol, 0.1 mg/ml BSA, 2 mM MgCl<sub>2</sub> and 2 mM DTT), the temperature was lowered to 25°C (except for 37°C experiments), and the flow cell was imaged to quantify the fluorescence from the RNA-annealed *Fluorescent\_stall'* probe.

### **RNA-MaP equilibrium binding experiments**

To determine PUM1 and PUM2 binding affinities, the RNA library was sequentially equilibrated with increasing concentrations of Cy3B-labeled PUM proteins, and the amount of Cy3B fluorescence colocalized with each RNA cluster was determined at each concentration. Two-fold serial protein dilutions (15–17) were prepared in 1x Binding buffer and were stored in light-protected tubes on ice or in the 4°C autosampler chilling block until the incubation. Protein solution (460 μL) was pumped into the flow cell at each concentration and incubated for times ranging from 33 min for the lowest concentrations to 19 min for the highest protein concentrations (25°C; 15–23 min at 37°C). These incubation times were established to be sufficient for equilibration by association and dissociation time courses (half-time ≤ 5.3 min; see also ([Vaidyanathan et al., 2017](#))). The incubation temperature was 25 or 37°C, as indicated for the individual experiments.

### HPLC purification of RNA oligonucleotides for competition binding measurements

Desalted RNA oligonucleotides were ordered from IDT and purified by reverse-phase HPLC (XBridge Oligonucleotide BEH C18 Prep column or Agilent ZORBAX Eclipse Plus C18 column), using an acetonitrile gradient in the presence of 0.1 M triethylamine acetate. Following purification, the solvent was exchanged into MilliQ water with Amicon Ultra 3KDa concentrators.

### $[\gamma\text{-}^{32}\text{P}]$ -labeling of RNA oligonucleotides

RNA oligonucleotides for direct binding measurements were ordered from IDT and 5' labeled with  $[\gamma\text{-}^{32}\text{P}]$  ATP (Perkin Elmer) using T4 polynucleotide kinase (T4 PNK, Thermo Fisher Scientific). The 5  $\mu\text{L}$  reactions contained 1x PNK buffer (Thermo Fisher Scientific), 5  $\mu\text{M}$  oligonucleotide, 5  $\mu\text{M}$   $[\gamma\text{-}^{32}\text{P}]$  ATP and 1  $\mu\text{L}$  of T4 PNK. The reactions were incubated at 37°C for 30 min and purified by non-denaturing gel electrophoresis (20% acrylamide).

### Gel-shift binding measurements

#### Competition binding measurements

To obtain PUM2 binding affinities in the absence of potential structure formation and alternative sites, and to compare the affinities determined by different approaches, we performed competition gel shift binding measurements with 8-mer oligonucleotides carrying a subset of single mutations in the UGUAUUA background. PUM2 (0.68 nM) was combined with trace labeled "S1a" RNA (UCUCUUUGUAUUAUCUCUU, <0.08 nM) in binding buffer (2 mM DTT, 100 mM KOAc, 0.2% Tween-20, 20 mM sodium HEPES, pH 7.4, 5% glycerol, 0.1 mg/mL BSA, 2 mM  $\text{MgCl}_2$ ), and diluted two-fold into solutions containing varying concentrations of unlabeled competitor RNAs (3-fold serial dilution series; 7–8 concentrations per oligonucleotide; final concentrations were 0.34 nM PUM2, < 0.04 nM labeled S1a RNA, 0.17–3330 nM competitor RNA, depending on the oligonucleotide). Binding reactions were incubated at 25°C for at least 1 h; equilibration was established by measuring binding after 1 h and 4.5 h incubations, which gave consistent results. We also performed controls for titration effects, by incubating the most tightly bound oligonucleotides (consensus, 5G and 7G variants) with 0.16 or 0.32 nM PUM2 (final concentration), giving consistent affinities. Following equilibration, 7.5  $\mu\text{L}$  aliquots were transferred to 7.5  $\mu\text{L}$  ice-cold loading buffer (5% Ficoll PM 400 (Sigma), 0.03% BPB, and 2  $\mu\text{M}$  unlabeled S1a RNA in binding buffer). The low temperature and unlabeled consensus RNA in the loading buffer prevented changes due to potential re-equilibration during sample loading (Vaidyanathan et al., 2017). The samples were carefully and immediately loaded on a continuously running 20% native acrylamide gel (5°C, 750 V, 0.5x Tris/Borate/EDTA (TBE) running buffer: 44.5 mM Tris-borate, 1 mM  $\text{Na}_2\text{EDTA}$ , pH 8.3; DANGER: extreme caution is required in this step due to high voltage; <https://ehs.stanford.edu/reference/electrophoresis-safety>). Gels were dried, exposed to phosphorimager screens and scanned with a Typhoon 9400 Imager.

Binding affinity for the labeled S1a oligonucleotide was measured in parallel by incubating 0.0038–81 nM PUM2 (3-fold serial dilutions) with trace labeled S1a RNA (<0.04 nM) in binding buffer for at least 1 h at 25°C. Samples were analyzed by gel electrophoresis as above. Measurements with three labeled RNA concentrations across a 9-fold range (upper limits of 13–120 pM) gave consistent results, indicating no titration effects. Sufficient equilibration time was established by measuring the dissociation rate (0.011  $\text{s}^{-1}$ , corresponding to 5.25 min upper limit of equilibration time—i.e., five half-lives; see below (Vaidyanathan et al., 2017)).

The gels were quantified with TotalLab Quant and fitting was performed with KaleidaGraph 4.1 (Synergy). The affinity for the labeled S1a RNA was determined by fitting to a single-site binding equation:

$$\theta = A \times \frac{[P]}{K_D + [P]} + b \quad (\text{Eq. 1})$$

where  $\theta$  is fraction bound RNA, A is amplitude, [P] is PUM2 concentration,  $K_D$  is the equilibrium dissociation constant and b is background. Competitor affinities ( $K_{D,\text{comp}}$ ) were determined using the equation by Lin & Riggs (Lin and Riggs, 1972):

$$K_{D,\text{comp}} = \frac{2 \times K_D^* \times [R_{\text{comp}}]_{1/2}}{2 \times [P]_{\text{total}} - [R^*]_{\text{total}} - 2 \times K_D^*} \quad (\text{Eq. 2})$$

where  $K_D^*$  is the dissociation constant of the labeled S1a RNA;  $[R_{\text{comp}}]_{1/2}$ , the competitor concentration at which half of the labeled RNA is bound;  $[P]_{\text{total}}$ , the protein concentration; and  $[R^*]_{\text{total}}$  the labeled RNA concentration. To determine the fraction of competitor RNA at which half of labeled RNA was bound, the competition binding curves were normalized by the fraction of labeled S1a RNA bound at saturation with no competitor (0.94).  $[R^*]_{\text{total}}$  was the upper limit of the labeled RNA concentration based on the total input and elution volume in the labeling reaction (<0.04 nM). Using the lower limit based on scintillation measurements of the  $^{32}\text{P}$  label (~0.004 nM) did not affect relative affinity calculations and affected absolute affinities by <10%. The values shown in Figure 2F, S3F are averages and 95% CIs from two replicate measurements.

For determination of flanking sequence effects, CUUGUAUUAU oligonucleotides (N = A/C/G/U) were ordered from IDT, 5' end labeled with  $[\gamma\text{-}^{32}\text{P}]$  ATP, and binding was measured as described for the S1a RNA above.

To compare single mutant effects determined by gel-shift to those determined by RNA-MaP,  $\Delta\Delta\text{G}$  values for the 8-mer oligonucleotides were calculated relative to the UGUAUUA consensus. For position 9 variants,  $\Delta\Delta\text{G}$  values were determined relative to the most tightly bound residue ('G'; Figure S2D).

### Dissociation rate constant measurements

PUM2 dissociation rate constant from S1a RNA was measured by incubating 3.8 nM PUM2 with labeled S1a RNA (<0.5 nM) in binding buffer at 25°C for 50 min, followed by addition of 2.5-fold volume excess of unlabeled RNA chase in binding buffer (final concentrations: 1 nM PUM2, <0.14 nM labeled S1a RNA, 1 μM unlabeled S1a RNA). At various time points, 7.5 μL aliquots were moved to 7.5 μL ice-cold loading buffer (5% Ficoll PM 400 (Sigma), 0.03% BPB in binding buffer) and immediately loaded on continuously running 20% native acrylamide gel. The dissociation curve was fit to a single exponential in Kaleidagraph:

$$\theta = (A - b) \times e^{-k_{\text{off}}t} + b \quad (\text{Eq. 3})$$

where  $\theta$  is fraction bound RNA,  $A$  is the fraction bound before adding the chase ( $A = 0.90$ ),  $b$  is the fraction bound at the completion of the dissociation reaction ( $b = 0.02$ ),  $k_{\text{off}}$  is the dissociation constant, and  $t$  is time after adding chase.

### Determination of active protein fraction by titration

Saturating concentration of unlabeled consensus RNA (10–200 nM; S1a or UCUUGUAUAUAUA for wild-type PUM1 and PUM2, UCUUGUAUUUAUA for mutant PUM1) was mixed with trace  $^{32}\text{P}$ -labeled RNA of the same sequence (<0.15 nM) and incubated with protein concentrations at least 4-fold below and above the RNA concentration for 45 min – 1 h (25°C). Following native gel electrophoresis, active protein fraction was determined from the intersection of lines fit through protein concentrations below and above the breakpoint. Throughout, the protein concentrations and absolute affinities reflect active protein concentrations (SNAP-Cy3B-PUM2: 57%, PUM1-SNAP-Cy3B: 61%, mutPUM1-SNAP-Cy3B: 20%, unlabeled SNAP-PUM2 used for gel-shift experiments: 38%–45%).

## QUANTIFICATION AND STATISTICAL ANALYSIS

### Computational analyses

#### Processing sequencing data

Illumina MiSeq sequencing data were computationally processed to extract the tile identifier and the x- and y-locations of each sequenced cluster from the fastq file output (Denny et al., 2018; She et al., 2017). Sequence clusters were divided into three categories: (1) clusters encoding our RNA library, (2) clusters containing the fiducial sequence, and (3) inert “background” sequence clusters lacking the RNAP initiation site or the fiducial sequence. This assessment was based on alignment of the read1 sequence to (1) the RNA polymerase initiation site and stall sequence “TTTATGCTATAATTATTCATGTAGTAAGGAGGTTGTATGGAAGACG TTCCTGGATCC,” or to (2) the fiducial sequence “CTTGGGTCCACAGGACTCGTTGCTTTCC,” or (3) neither, respectively.

While every cluster was fit during the 2D Gaussian fitting (described below), only clusters containing the fiducial sequence were used during the cross-correlation of the images to the sequencing data.  $K_D$  fitting was only performed on RNA-encoding clusters (described below).

#### Fitting images

To attribute fluorescent binding events to individual sequence variants, the images taken during the RNA array experiment were mapped to the sequencing data output from the Illumina MiSeq. Each image had a set of fiducial clusters, which were visualized with a fluorescently labeled complementary oligo (see *RNA transcription in the flow cell* above). The x- and y-locations of each fiducial cluster were cross-correlated with each fluorescent image in an iterative fashion to determine a smooth function of x and y that represents the location-dependent offset between the image and the sequencing data locations. This “registration offset map” enabled correlation between image and sequencing locations at sub-pixel resolution, as described in (She et al., 2017). Once this map was determined, each image was fit to the sum of 2D Gaussians, with each Gaussian centered at each of the cluster locations from the registered sequencing data output. The quantified fluorescence of each cluster was thus the integrated fluorescence within the fit 2D Gaussian ( $f = 2\pi a\sigma^2$  where  $f$  is the integrated fluorescence and  $a$  and  $\sigma$  are the fit amplitude and standard deviation, respectively).

#### Identifying library variants from sequencing data

Incorporation of a 15-nt unique molecular identifier (UMI) in our library allowed us to minimize the effect of sequencing errors when associating each sequenced cluster with its underlying sequence variant, as described in (Buenrostro et al., 2014). Prior to sequencing, the library was bottlenecked and reamplified (see *Library preparation* above), resulting in increased representation of each UMI that survived the bottlenecking. We assumed that all sequences associated with the same UMI came from the same molecular variant, so that any variation between these sequences was the result of sequencing error. To resolve sequencing errors, a consensus sequence of the associated library variant was determined for each UMI with a per-base voting strategy. Only UMIs with a significant fraction of variants matching the consensus sequence were used, as evaluated by a binomial null model. For each UMI, a p value was calculated based on the number of associated sequences that matched the consensus sequence and the total number of sequences, assuming a rate of success under the null model of 25%. UMIs with a higher rate of matching than expected by chance under the null model (i.e., with p value <0.01) were defined as successfully associating with a consensus sequence. Clusters were then associated to a designed library variant based on the cluster’s UMI.

#### Fluorescence normalization

To account for inter-cluster variation in maximum fluorescence, we normalized the amount of protein bound at a given cluster by the total amount of transcribed RNA in that cluster. This normalization was performed by dividing the integrated fluorescence of



the cluster in the green channel (i.e., the channel imaging the bound protein) by the integrated fluorescence of the same cluster in the red channel (i.e., the channel imaging the fluorescent oligo annealed to the transcribed RNA). To prevent dividing by small numbers and inflating the normalized signal toward infinity, values of the red channel fluorescence below the threshold of the first percentile of the distribution of the red channel fluorescence across clusters were set to the value of the threshold.

### Determining the free energy of binding

The normalized fluorescence values of bound protein across different solution protein concentrations were used to determine the equilibrium dissociation constant ( $K_D$ ) between the protein and each RNA variant. The fitting procedure was split into several steps to allow robust fitting across a range of affinities, and the binding model accounted for observed non-specific binding events. In brief, the normalized fluorescence values for each individual cluster were fit to a binding curve to obtain best-fit values for  $K_D$  and other fit parameters (see *Single cluster fitting* below). These best-fit values for individual clusters were used to determine distributions for fit parameters that we expect to be variant-independent — i.e.,  $K_{D,NS}$ ,  $f_{min}$ , and  $f_{max}$ , which are each defined below. The distributions of these common values across library variants were used to refine the  $K_D$  value for each RNA variant.

### Single cluster fitting

Initially, fluorescent values for each cluster were fit to a binding curve. This binding model incorporated a nonspecific binding term, as follows:



where R is RNA, P is protein,  $K_D$  is the dissociation constant ( $K_D = e^{\Delta G/RT}$ ) and  $K_{D,NS}$  is the non-specific dissociation constant for a second protein monomer that binds to the RNA-protein complex ( $K_{D,NS} = e^{\Delta G_{NS}/RT}$ ).

The normalized fluorescence of a cluster at protein concentration [P] can be defined as:

$$f = f_{min} + f_{max} \frac{[P]}{[P] + K_D} \left( 1 + \frac{[P]}{[P] + K_{D,NS}} \right) \quad (\text{Eq. 5})$$

where  $f_{min}$  is the background fluorescence in the absence of bound protein,  $f_{max}$  is the fluorescence signal at saturation, and [P] is the concentration of the protein in solution (here,  $[P] \approx [P]_{total}$ ). This model was used to account for an observed increase in fluorescence at high concentrations of protein after apparent saturation (Figure 1D). We did not observe a corresponding increase in fluorescence for non-binding variants, and the extent of ‘non-specific’ binding increased with greater specific binding affinity. Together, these observations support the model that a second protein monomer binds to the RNA-protein complex on chip (as opposed to non-specific binding to the DNA or unbound RNA, which would be independent of bound protein).

Least-squares fitting was performed using the Python package lmfit (v0.8.3). The initial estimates and constraints are as follows:  $f_{min}$  was initialized to the median fluorescence across clusters in the images with no protein applied, and was constrained to be not less than zero during the fitting;  $f_{max}$  was initialized at the maximum fluorescence observed at any concentration of protein for that cluster, and was similarly constrained to not be less than zero;  $K_D$  was initialized at the highest concentration of the protein; and  $K_{D,NS}$  value was initialized at five-fold the highest concentration of the protein.

### Finding common values for $K_{D,NS}$ , $f_{min}$ , and $f_{max}$ across variants

Allowing all four free parameters ( $f_{min}$ ,  $f_{max}$ ,  $K_D$ , and  $K_{D,NS}$ ) to float during the fitting process led to some spurious effects. In particular, variants with low affinity that do not achieve saturation within the probed protein concentration range can be fit approximately equally well with different values for  $f_{max}$  and  $K_{D,NS}$ , ultimately leading to uncertainty in the fit value for  $K_D$ . For example, a variant that does not achieve saturation may be fit equally well with lower values for  $K_D$  and  $f_{max}$ , higher values for  $K_D$  and  $f_{max}$ , or a higher value for the  $K_{D,NS}$  and lower value for  $K_D$ . On the other hand, the library contains numerous tightly bound variants which have achieved saturation and from which we can extract most likely values for the sequence-independent parameters  $f_{min}$ ,  $f_{max}$ , and  $K_{D,NS}$ . These values are largely constant across different molecular variants that did achieve near-saturation (Figure S1E,F), allowing us to reasonably assume that the same values are applicable to all molecular variants, i.e., even those that did not achieve saturation, and applying these well-defined estimates for  $f_{min}$ ,  $f_{max}$ , and  $K_{D,NS}$  allows more confident fitting of the  $K_D$  values. To limit noise, the estimates for  $f_{min}$ ,  $f_{max}$ , and  $K_{D,NS}$  were determined based on the per-variant values of each fit parameter, where per-variant values are the median of the single-cluster values associated with the same molecular variant.

### Estimating $f_{min}$

The value for  $f_{min}$  was largely consistent across variants (Figure S1E); thus, the estimate for this fit parameter was simply the median value across variants.

### Estimating the distribution of $f_{max}$

To define the distribution of  $f_{max}$  values across molecular variants, a subset of variants with low and precisely measured  $K_D$  values was used, based on the single cluster fits. Variants used to define this distribution had  $K_D$  values less than 5% of the highest concentration of protein. In addition, the precision of the per-variant values of  $K_D$  was evaluated based on the proportion of the variant’s single cluster fits having a goodness-of-fit ( $R^2$ ) greater than 0.5, the standard error on  $\Delta G$  ( $\Delta G = RT \ln(K_D)$ ) less than 1 kcal/mol, and the standard error on the fit  $f_{max}$  less than  $f_{max}$ . If a significant fraction of the clusters associated with this variant passed these filters, then the variant was considered to have a “precise” measurement of  $K_D$ . Significance was assessed based on rejecting the null

hypothesis that 25% of clusters would pass all these filters by chance alone (binomial p value < 0.01). For variants that did not achieve saturation the  $f_{\max}$  was undefined, so the distribution of  $f_{\max}$  values across the tightly bound molecular variants was used to find error estimates on the  $K_D$  values that reflect this uncertainty.

The  $f_{\max}$  distribution across these variants was fit to a gamma distribution with fixed mean for the entire experiment, but whose standard deviation was dependent on the number of clusters per molecular variant (i.e., standard deviation should be proportional to  $1/\sqrt{n}$ , where  $n$  is the number of clusters per variant). This distribution reflects the fact that as the number of clusters increases, we can obtain more precise estimates of  $f_{\max}$  and thus  $K_D$ . The mean  $f_{\max}$  value was obtained by fitting the per-variant  $f_{\max}$  values to a gamma distribution, and obtaining the mean of the distribution,  $\mu_{\text{global}}$ . To obtain the standard deviation of the  $f_{\max}$  distribution at each value of  $n$  (where  $n$  is the number of clusters per variant), the distribution of per-variant  $f_{\max}$  values of variants with  $n$  clusters was fit to the gamma function  $f(x)$ , for every normalized fluorescence value  $x$ :

$$f(x - k_n, a_n, \theta_n) = \left(\frac{x - k_n}{\theta_n}\right)^{a_n - 1} \exp\left(-\frac{x - k_n}{\theta_n}\right) / \Gamma(a_n) \quad (\text{Eq. 6})$$

where  $k_n$  is a free parameter,  $a_n \cdot \theta_n \equiv \mu_{\text{global}}$ , and the resulting standard deviation is  $\sigma_n = \sqrt{a_n \theta_n^2}$ . Allowing  $k$  to float resulted in better estimates of the standard deviation when distributions were more asymmetric, as often occurred for variants with small  $n$ . The value of  $k_n$  was initialized at 0, and  $\sigma_n$  was initialized at the standard deviation of the  $f_{\max}$  values.

The values for  $\sigma_n$  may be subject to noise, given that some values of  $n$  had many more variants associated with that number of clusters than others did. To smooth these values, the  $\sigma_n$  values were used to fit the expected analytical function that defines the relationship between number of measurements and standard error,  $\sigma(n) = (\sigma_1/\sqrt{n}) + \sigma_0$ , where  $\sigma_0$  and  $\sigma_1$  are free parameters.  $\sigma_1$  is the standard deviation on the estimate of  $f_{\max}$  with only one measurement, and  $\sigma_0$  represents the standard deviation of  $f_{\max}$  among different molecular variants if all variants were measured an infinite number of times. We expect this term to be nonzero in the case that the  $f_{\max}$  depends on the molecular variant: e.g., if certain variants are trapped in stable secondary structures that do not unfold on the timescale of the binding experiment.

The estimator for  $f_{\max}$  for each molecular variant with  $n$  clusters per variant is then the gamma distribution:

$$f(x, a_n, \theta_n) = \left(\frac{x}{\theta_n}\right)^{a_n - 1} \exp\left(-\frac{x}{\theta_n}\right) / \Gamma(a_n) \quad (\text{Eq. 7})$$

where  $a_n = (\mu_{\text{global}}/\sigma(n))^2$  and  $\theta_n = \sigma(n)^2/\mu_{\text{global}}$ , which depends only on  $\mu_{\text{global}}$  and  $\sigma(n)$ , and the number of clusters per variant  $n$ .

### Estimating $K_{D,NS}$

The value for  $K_{D,NS}$  was determined by taking the median value across the subset of variants with low and precisely measured  $K_D$  values, based on the single cluster fits, as described above for determining the distribution of  $f_{\max}$  values. The  $\Delta G_{NS}$  terms (=  $RT \log(K_{D,NS})$ ) for each protein were similar, with the following values: PUM2:  $-8.98$  and  $-8.87$  kcal/mol for replicates 1 and 2, respectively (25°C),  $-8.65$  kcal/mol (37°C); WT PUM1:  $-8.46$  kcal/mol; mutant PUM1:  $-8.19$  kcal/mol.

### Applying common values for $K_{D,NS}$ , $f_{\min}$ , and $f_{\max}$ to refine estimates for $K_D$

Binding isotherms were refined for all variants using the variant-independent values for  $f_{\min}$ ,  $K_{D,NS}$ , and, for the cases in which the variant did not achieve near-saturation,  $f_{\max}$ . To perform this refinement, clusters associated with each variant were resampled to obtain median fluorescence values across resampled clusters. This vector of median fluorescence values was fit to a binding isotherm with the values for  $f_{\min}$  and  $K_{D,NS}$  fixed to the variant-independent values obtained above. For the cases where the variant did not reach near-saturation the value for  $f_{\max}$  was also fixed. Not achieving near-saturation was defined as the median fluorescence value at the highest concentration of protein being less than the lower bound of the 95% confidence interval on  $f_{\max}$ . In this case, the value for  $f_{\max}$  was sampled from the variant-independent distribution of  $f_{\max,n}$  (with  $n$  equal to the number of clusters associated with this variant) (Equation 7). To obtain uncertainty estimates on the fit  $f_{\max}$  and  $K_D$  values, this resampling procedure was repeated 100 times. In the case that the variant did not achieve saturation, a different value for  $f_{\max}$  was sampled for each iteration.

The 95% confidence intervals on  $K_D$  were obtained using these 100 values. The median fit  $K_D$  obtained from the initial single cluster fits was used as the initial value in the least-squares fitting of each fitting iteration. For variants where  $f_{\max}$  was allowed to float, the median fit  $f_{\max}$  was used as the initial value.

### Fitting background clusters to determine maximum measurable $\Delta G$

To obtain a reasonable estimation of the highest  $K_D$  that can be measured by this method, we applied this fitting procedure to a set of “background” variants—i.e., variants on the chip lacking an RNAP initiation site. To normalize the bound fluorescence in the green channel to a similar scale as those clusters that do transcribe RNA, the fluorescence values were divided by the median fluorescence value in the red channel across clusters that do have RNAP initiation sites. Background clusters were randomly assigned to a “variant ID,” such that the set of “background variants” had a similar number of associated clusters as our library members. Finally, fitting was carried out as described in “Applying common values for  $K_{D,NS}$ ,  $f_{\min}$ , and  $f_{\max}$  to refine estimates for  $K_D$ ,” with the variant-independent values for  $f_{\min}$ ,  $f_{\max}$ , and  $K_{D,NS}$  applied. The reliable  $\Delta G$  threshold determined by this analysis for PUM2 was approximately  $-8.5$  kcal/mol (Figure S1F), and only variants with  $\Delta G$  values less than this threshold (corrected for active protein fraction) were included in the high-confidence affinity data reported herein.

### Data filtering

Variants were included in our analyses if they met the following criteria (unless otherwise indicated): (1) observed  $\Delta G$  values lower than  $-8.5$  kcal/mol; this range was established as clearly distinguishable from background of non-transcribed clusters (see *Fitting background clusters to determine maximum measurable  $\Delta G$*  in the [Computational analyses](#) section above); (2) five or more clusters in at least one replicate experiment, to allow robust cluster statistics; in cases where one of the replicates contained fewer than five clusters, only the  $\Delta G$  value from the replicate with five or more clusters was used; (3) 95% bootstrap confidence interval of the  $\Delta G$  value (or the weighted error of replicate  $\Delta G$  values for PUM2 measurements at  $25^\circ\text{C}$ ) less than 1 kcal/mol; all 95% CI values were corrected to account for inter-experimental error, as described in (Denny et al., 2018). The numbers of variants passing each filter are indicated in [Table S5](#).

Given the overall weaker binding of mutant PUM1 and to allow more comprehensive comparisons of single-mutant binding by wild-type and mutant protein ([Figure 5D](#)), we relaxed the affinity filter for mutant PUM1 data. Rather than applying a  $\Delta G < -8.5$  threshold, we included variants with at least 15% of RNA bound by PUM1 mutant at the highest probed protein concentration.

In comparisons of PUM2 replicate experiments ([Figure 1D](#)), and of PUM1 versus PUM2 affinities ([Figure 5A](#)), the entire oligonucleotide library was used, including sublibraries that will be fully addressed in future manuscripts. In these comparisons, an additional filter was applied to exclude any oligonucleotides with more than one binding site, defined as two UGUA sites separated by at least four bases.

### Assessing reproducibility and combining experimental replicates

Two replicate experiments of PUM2 binding were combined by calculating the error-weighted mean:

$$\Delta G_{\text{comb}} = \left( \frac{\Delta G_1}{\sigma_1^2} + \frac{\Delta G_2}{\sigma_2^2} \right) \left( \frac{1}{\sigma_1^2} + \frac{1}{\sigma_2^2} \right)^{-1} \quad (\text{Eq. 8})$$

where the  $\Delta G_1$  and  $\Delta G_2$  are  $\Delta G$  values from each replicate and  $\sigma_1$  and  $\sigma_2$  are 95% confidence intervals of the respective  $\Delta G$  values. Weighted propagated error was calculated as:

$$\sigma_{\text{comb}} = \left( \sqrt{\frac{1}{\sigma_1^2} + \frac{1}{\sigma_2^2}} \right)^{-1} \quad (\text{Eq. 9})$$

The observed small systematic offset ([Figure 1E](#)) was subtracted from Replicate 2 values before averaging to prevent distortions in cases where a variant was only present in one replicate. The offset (0.28 kcal/mol) was derived from mean replicate difference between highest affinity variants ( $\Delta G < -9.8$  kcal/mol).

### Assessing the significance of scaffold differences

The significance of single mutant scaffold differences before and after accounting for structure was assessed via a false discovery rate (FDR) approach. For each single mutant and consensus sequence, the deviation of the  $\Delta G$  value (weighted replicate average, [Equation 8](#)) from the scaffold average ( $\Delta G_{\text{avg}}$ ) was determined and converted into a z-score:

$$z = \frac{\Delta G - \Delta G_{\text{avg}}}{\sigma_{\Delta G}} \quad (\text{Eq. 10})$$

where  $\sigma$  is the weighted replicate error ([Equation 9](#)). The distribution of resulting z-scores was then compared to a null distribution, where the z-scores are normally distributed around a zero mean with a standard deviation of 1. For each z-score, the number of false discoveries was determined from the probability of obtaining a value more extreme than this z-score given the null distribution (two tailed; value =  $2 * \text{CDF}(-|z|)$ ), multiplied by the total number of variants. The total number of discoveries corresponded to the sum of the number of false discoveries (above) and the number of actual z-scores whose absolute values were greater than or equal to that z-score threshold. Scaffold differences were considered significant if the respective z-score had  $\text{FDR} \leq 10\%$ . Asterisks in [Figures 2A, D](#) and in [Figure S2C](#) indicate mutants where at least one scaffold showed a significant deviation from the scaffold mean.

To assess the contributions of RNA secondary structure to the scaffold variance, the above analysis was repeated using structure-corrected affinities (see [Accounting for RNA structure](#) below; 'Structure-corrected' in [Figures 2B, S2A](#)), as well as affinities of variants that lacked significant predicted structure ( $\Delta G_{\text{fold}} > -0.5$  kcal/mol; 44 of 65 total variants, including the UGUUAUA consensus).

### Accounting for RNA structure

We used Vienna RNAfold (v. 2.1.9) (Lorenz et al., 2011) to predict ensemble stabilities for RNA structures in which the protein binding site is accessible versus occluded due to base pairing ([Figure 2C](#)). The effect of accessibility on protein binding was defined as follows (see model in [Figure S3B](#)):

$$K_D^{\text{obs}} = K_D \times \frac{1 + K_{\text{fold}}}{1 + K_{\text{fold,accessible}}} \quad (\text{Eq. 11})$$

where  $K_D^{\text{obs}}$  is the measured dissociation constant,  $K_D$  is the intrinsic dissociation constant (for accessible RNA),  $K_{\text{fold}}$  is the folding equilibrium constant that represents the ensemble of RNAs that are structured (accessible + occluded) and  $K_{\text{fold,accessible}}$  is the folding equilibrium constant representing RNA structures in which the protein binding site is accessible. Accessible binding sites were defined as lacking base-pairing in the 8-mer core binding site (for the purpose of structure predictions) (Figure 2C). Folding equilibrium constants were based on ensemble stabilities predicted by RNAfold (RNAfold -p0 -T 25 C or RNAfold -p0 -T 37 C); stabilities of accessible RNA structures were predicted by including the constraint flag (RNAfold -p0 -T 25 C -C) and constraining the 8-mer binding site to a single-stranded state, e.g.:

```
UCUCUUUGUAUAUAUCUCUU
.....XXXXXXXXX.....,
```

where 'x' indicates unpaired residues. Structure effects were considered if they exceeded 0.5 kcal/mol, except as noted.

### Assessing alternative binding registers in single mutant variants

To determine potential alternative binding registers in our single mutant constructs, we computationally scanned the full RNA sequence (including scaffold and variable region) with the additive consecutive model, wherein the predicted relative affinity (expressed as  $\Delta\Delta G$ ) at each 8-mer site corresponds to the sum of effects of each individual residue:

$$\Delta\Delta G^{\text{pred}} = \sum_{b=1}^8 \Delta\Delta G_b^X \quad (\text{Eq. 12})$$

$b$  is the position in the 8-mer RNA binding sequence and  $X$  is the identity of the residue at position  $b$ . The  $\Delta\Delta G_b^X$  values were derived from weighted scaffold averages for each single mutant relative to the weighted average of consensus affinities, after accounting for structure effects as described in Accounting for RNA structure. In calculating the predicted affinities for each register, structure effects were estimated by individually constraining the respective 8-mer site to the single-stranded state.

Figure S2D,E and Table S1 show the results of the initial assessment of register shifting, based on scaffold averages of mutant effects in the 5U background. No additional variants with shifted registers within less than 1 kcal/mol from the designed register were identified when the analysis was repeated for single mutants across 5A/C/U backgrounds, using mutant effects averaged across scaffolds and 5A/C/U backgrounds in Equation 12 (Figure S3A,B).

### Development, testing and evaluation of thermodynamic binding models

To ensure the highest accuracy of model testing and global fitting, the library was filtered to only include variants without significant predicted secondary structure ( $\Delta G_{\text{fold}} > -0.5$  kcal/mol). For variants in the S1a and S1b scaffolds, we considered the ensemble structure of the entire RNA construct; for S2a and S2b scaffolds, only the stability of structures within the hairpin loop was considered, due to the high stability of the stem. The ensemble stability of structures involving the loop region was determined as the difference between RNAfold-predicted stabilities with and without the loop region constrained to the single-stranded state ( $\Delta G_{\text{fold,loop}} = \Delta G_{\text{fold}} - \Delta G_{\text{fold,ss}}$ ). Only the loop sequences were used for binding predictions in global fitting.

To reduce potential systematic bias in the  $\Delta\Delta G$  values ( $\Delta\Delta G = \Delta G - \Delta G_{\text{WT}}$ ) that may affect the fit, we did the following. The  $\Delta\Delta G$  values (observed and predicted) were defined relative to the UGUUAUAUAU reference sequence rather than the slightly more stable UGUUAUAUAG sequence (Figures 2E, S2F), because UGUUAUAUAU was more highly represented in our library and was predicted to have less residual structure ( $n = 183$  for  $\Delta G_{\text{fold}} > -0.2$  kcal/mol). To determine the median consensus affinity, we applied the more stringent structure cutoff of  $-0.2$  kcal/mol (versus  $-0.5$  kcal/mol) due to the greater, asymmetric spread of values observed when the  $-0.5$  kcal/mol threshold was used, consistent with residual structure effects. The variants used for global fitting and their affinities and  $\Delta\Delta G$  values measured for PUM2, PUM1 and mutant PUM1 are indicated in Table S5.

Importantly, in testing and globally fitting the models below, we accounted for all possible binding modes and registers, because the strongest binding can arise from a site downstream of or partially overlapping with the original designed site, and these altered registers become more probable the larger the destabilization from mutations within the original consensus site (see Figure 4A). The presence of multiple binding modes of similar affinity will also increase the overall observed affinity.

*Testing the additive consecutive model.* Additive consecutive model predictions were calculated using the equation in Figure 3A for every 9-mer register in each oligonucleotide in the library, based on measured single mutant penalties (Table S2). The ensemble affinity for a given oligonucleotide was determined as illustrated in Figure 4A ('Consecutive'; top left):

$$\Delta\Delta G_{\text{ensemble}} = -RT \ln \left( \sum_{r=1}^n e^{-\frac{\Delta\Delta G_r}{RT}} \right) \quad (\text{Eq. 13})$$

where  $n$  is the length of the oligonucleotide variant,  $r$  is the index of an individual 9-mer register,  $\Delta\Delta G_r$  is the predicted penalty for binding in register  $r$ ,  $R$  is the gas constant and  $T$  is temperature (25°C).

For direct comparison of the performance of the additive consecutive and additive nonconsecutive models (with and without coupling), data for all unstructured variants ( $n = 5206$ ) were plotted in Figure 3A, including the single mutants ( $n = 113$  across the four scaffolds and 5A/C/U backgrounds); excluding the single mutants did not significantly alter the fit values (RMSE = 1.04 kcal/mol;  $R^2 = 0.73$ ).

Global fitting to the additive consecutive model (Figure S4B,C) was performed as described in the *Global fitting* section below, using terms for bound residues only.

### Base flipping analysis

For the initial assessment of the additive nonconsecutive model that permits base-flipping, we focused on oligonucleotides in our library that contained C-insertions at various positions of the consensus sequence (UGUAUUAU). For comparisons to the additive consecutive model predictions in Figure 3C,D, we used variants without predicted register shifts to favorable sites involving flanking sequences, as this allowed for the most accurate estimation of the lower limit of the flipping penalty at the indicated site. The construct sequences used are indicated in Table S3.

### Global fitting

To fit the final model (additive nonconsecutive with coupling; Figure 3F), the  $\Delta\Delta G$  values for all registers with no flips, all registers with single flips, all registers with double flips, and all registers with two single nucleotide flips were included when computing the partition function for binding (see Figure 4A). Registers with more than two flipped residues were not included in the partition function calculation because their predicted affinity was low enough that it minimally affected the overall binding affinity of the ensemble of bound states. The  $\Delta\Delta G$  values for individual registers were used to compute the partition function and the overall  $\Delta\Delta G$  for the ensemble of bound states for each RNA variant ( $\Delta\Delta G(\text{ensemble}) = -RT \ln(\sum e^{-\Delta\Delta G_i/RT})$ , where  $i$  is the register number (Figure 4A)). This ensemble  $\Delta\Delta G$  was compared to the experimentally observed  $\Delta\Delta G$  values during fitting. The model assumed a single protein bound to each RNA variant, which was supported by the tight distribution of  $f_{\text{max}}$  values and our ability to detect binding of multiple bound protein monomers based on proportional increase in fluorescence (Figure S1E; Becker et al., 2019b, in preparation). The additive consecutive and additive nonconsecutive models (Figure 3A,E) were fit analogously, but with the flipping and coupling terms (additive consecutive model) or coupling terms (additive nonconsecutive) excluded from the model.

During fitting, the only values that were not allowed to vary were the bound parameters for the consensus 'UGUAUUAU' residues, which were set to a penalty of 0 kcal/mol. The other bound parameters for non-consensus residues were allowed to vary within the higher of the 95% confidence interval determined from the individual single mutant measurements or  $\pm 0.4$  kcal/mol from the median  $\Delta\Delta G$  values from the individual single mutant measurements (Figure 2E, Table S2). Single and double flip parameters were essentially unconstrained during fitting and were allowed to vary between 0 and 7 kcal/mol. The coupling terms were constrained to between  $-4$  and 0 kcal/mol. The coupling terms were included in both consecutive and flipped registers, with the condition that no flips interrupted the series of flipped residues. The script used for global fitting can be found on <https://github.com/pufmodel>.

All models were initially trained on a randomly selected subset of half the data and tested on the remainder of the data to prevent overfitting. In all cases, the model performed nearly identically on the training and test sets. To compute the final parameters, the model was fit with all sequences meeting the structure cutoff. All models described in the text were fit by minimizing the sum of the squared error between the predicted and measured  $\Delta\Delta G$  values for each sequence. To help ensure that the fit was finding a global minimum, both the BFGS and differential evolution algorithms implemented in the *lmfit* module in Python were used for fitting. Additionally, fits with flipping parameters were initialized to different values between 1 and 4 kcal/mol and led to the same fit parameters, providing additional support for convergence to a global minimum.

We assessed the stability of the final fit parameters (additive nonconsecutive including coupling model; Table 1, Figure 3F) by performing multiple fits with bootstrapping and a parameter sensitivity analysis. Bootstrapping was performed as follows: the 5206 sequences were sampled with replacement and the model parameters were fit to each resampled dataset. The 95% confidence intervals from the bootstrapping analysis are reported in Table S4. To examine how well bounded the model parameters were, we computed the sensitivity of the RMSE of predicted versus observed affinities to variations in each individual parameter while holding all others constant at their fit values (Figures S5, S6). Each value varied within the constraints that were applied during fitting. For some flipping parameters, the same RMSE value resulted from all parameter values greater than a given value, implying that for these parameters the penalty must be larger than a certain value so that it will not occur in the most stable register in any of our constructs, but because the parameter is so destabilizing we can only say that it must be at least as perturbative as the minimum value resulting in a constant RMSE. As a result, we reported the lower bound for these parameters (Table 1, 'Term II').

### Coupling analysis

To assess positional coupling, we tested double mutants of the UGUA[A/C/U]UAU reference sequence for systematic deviations from predictions by the additive consecutive model. To obtain the library variants for this analysis, we filtered our mutant library for all sequences that featured a single dominant consecutive register (i.e., with less than twofold, or 0.4 kcal/mol, further stabilization provided by other consecutive or flipped registers, as predicted by the additive nonconsecutive model in Figure 3E). Variants deviating from the consensus sequence at two positions were identified and their predicted affinities were calculated by adding the respective experimentally determined single mutation penalties ( $\Delta\Delta G^{\text{pred}} = \Delta\Delta G_1 + \Delta\Delta G_2$ ; Figure 2E, Table S2). We used the experimentally derived instead of globally fit single mutant penalties in this analysis, as coupling may affect the fit values. Qualitatively, the conclusions were not affected by the fit parameters, as in both cases the strongest coupling was observed between positions 7 and 8, with negligible deviations at other positions. Only double mutant combinations represented by more than one variant in our library were considered. Deviations between the observed and predicted  $\Delta\Delta G$  value were determined and averaged across all mutants with mutations at a given pair of positions (Figure S4D).

The double mutant analysis indicated coupling between mutated positions 7 and 8, with negligible deviations from additivity at other positions for which data were available. Because of the highly destabilizing effects of mutations in the 5' half of the binding

site, these mutations were strongly underrepresented among double mutants, as they generally lead to alternative registers being preferred or fall outside the reliably measurable affinity range. For the same reasons, any couplings involving 5' mutations are unlikely to be biologically relevant.

To determine the sequence dependence of position 7 and 8 couplings, including potential longer-range couplings, we next extended the analysis to varying combinations of residues flanking each position 7 and 8 residue. Specifically, and recognizing that coupling is most likely to occur between neighboring residues, we assessed the following combinations for systematic deviations from predicted values: 1) residue of interest flanked by two consensus residues; 2) only the 5' neighboring base mutated; 3) only the 3' neighboring base mutated; 4) both neighboring residues mutated. In this analysis, we included all variants that contained the indicated combination in the best predicted consecutive register (as predicted by additive nonconsecutive model; Figure 3E); any sequence was permitted outside the indicated combination.

Only 7G and 7C showed strong systematic deviations from predicted affinity for the indicated neighbor combinations (Figure S4E,F), and to a lesser extent—the 9G residue, which showed systematically tighter binding when preceded by the consensus residue 8A as opposed to residue 8 mutations (Figure S4G). Further inspection of 7G coupling indicated an additional bifurcation based on position 5 identity, indicating longer-range coupling (Figure S4E). The previously observed structural differences in purine and pyrimidine recognition at position 5, with dramatic effects on backbone configuration and in some structures—on position 6 recognition provide a potential structural rationale for this longer-range coupling (Lu and Hall, 2011).

### Analysis of *in vivo* crosslinking data

#### Determining a set of position weight matrices to find putative binding sites

The analysis of *in vivo* crosslinking data was carried out in two stages: first, we identified the transcriptome sites predicted to be bound by PUM2 ( $\Delta\Delta G^{\text{pred}} \leq 4$  kcal/mol) by using a set of position weight matrices (PWMs) that approximate our thermodynamic model to efficiently identify binding sites. Second, we applied the full thermodynamic model, as described in Figure 3F and Figure 4A, to this set of putative binding sites. Using PWMs for genome-wide searches is supported with currently available software and can computationally obtain matches to the whole transcriptome within a reasonable amount of time. In contrast, genome-wide application of the full thermodynamic model was prohibitively computationally expensive.

Each PWM is a matrix with rows representing different positions within the binding sequence and columns representing the four bases that could be at that position. The value of the PWM for each position and base is the probability of observing that base at that position in a set of binding sequences, wherein the probability is proportional to the  $\Delta\Delta G$  terms from our thermodynamic model, as detailed below:  $p_{i,j} = \sum_j \exp(\Delta\Delta G_{i,j}/RT) / \exp(\Delta\Delta G_{i,j}/RT)$  for position  $i$  and base  $j$ . For the simplest binding configuration (i.e., 9 bound positions with no flipped residues),  $\Delta\Delta G_{i,j}$  values corresponded to the binding terms in Table 1 ( $\Delta\Delta G_b^X$ ; 'Term I'). Each genomic sequence was compared with the PWM to determine a log-odds score:  $s = \sum_i l_{i,j} \log(p_{i,j}/0.25)$ , where  $l_{i,j} = 1$  if the sequence at position  $i$  has base equal to  $j$ , otherwise  $l_{i,j} = 0$ . A log-odds score of  $\geq 2$  was found to capture the large majority of variants with  $\Delta\Delta G < 4$  kcal/mol, and so this value was applied as the threshold above which a sequence was considered as a putative binding site.

To account for binding registers with a single flipped residue, a row was inserted at the flipped position, with values derived from the base flipping penalties ( $\Delta\Delta G_f^Y$ , Table 1, 'Term II'). Our thermodynamic model found that flipping is accommodated only in four positions; thus, a PWM was determined for each of these four binding registers. In practice, for a given sequence, flips between positions 4/5 and 5/6 had very similar PWMs, and so a single PWM was derived to search for both of these binding configurations, using the average values. On average, an inserted residue penalized the overall affinity by  $\sim 1.5$  kcal/mol. To account for this overall destabilization, the threshold log-odds score for these three flipped PWMs was increased to 4 (i.e., a sequence had to have log odds score  $\geq 4$  for the sequence to be considered as a putative binding site).

A set of four additional PWMs were derived to account for having two flipped residues at each of the four flipped positions. Once again positions 4/5 and 5/6 produced very similar PWMs and were averaged, resulting in three distinct PWMs. For these PWMs, the threshold for log-odds score was increased to 5 to account for the additional destabilization of having two flipped residues.

The PWM for no flipped residues and with one flipped residue had two or one fewer positions to account for, respectively, than the PWM for two flipped residues. Thus, all PWMs were brought to the same length of 11 rows (corresponding to 11 bound or flipped positions) by padding at the 3' end with rows that do not contribute to the log odds score of any sequence (values were set equal to 0.25 for all bases).

Finally, these seven PWMs and their respective threshold values were saved in a single file, with format defined by the program HOMER, as described: <http://homer.ucsd.edu/homer/motif/creatingCustomMotifs.html>.

#### Determining binding sites within the transcriptome

The seven PWMs described above were used to determine putative binding sites across the transcriptome for subsequent quantitative analysis with our full thermodynamic model. Initially, a set of genome locations was determined from the Gencode v24 annotation file, obtained from the ENCODE project:

wget [https://www.encodeproject.org/files/gencode.v24.primary\\_assembly.annotation/@@download/gencode.v24.primary\\_assembly.annotation.gtf.gz](https://www.encodeproject.org/files/gencode.v24.primary_assembly.annotation/@@download/gencode.v24.primary_assembly.annotation.gtf.gz).

These genome annotations were converted to a bed file format, and any overlapping regions were merged, using the program bedtools merge (v2.25.0). The package HOMER (v4.8.3) was used to search for matches to the PWMs within these genome locations, with the command:

```
annotatePeaks.pl ${genome_locations} hg38 -m ${pwm_file} -mbed {output_motif_locations} -noann -nogene.
```

The set of output motif locations, corresponding to putative binding sites, was subsequently filtered to remove any overlapping regions (bedtools merge), and if two regions overlapped, only the site with the lowest log odds score was kept. This set of motif sites was annotated again using HOMER to map each site to a gene, mRNA location (i.e., 5' UTR, CDS, 3' UTR), and gene type (i.e., protein-coding, noncoding RNA, etc.), each of which come from the default Refseq annotations for human genome assembly GRCh38 (hg38) (O'Leary et al., 2016).

```
annotatePeaks.pl ${motif_locations} hg38 > ${output_annotations}
```

These annotations were used to filter motif locations based on: (1) Being part of a protein-coding gene in the 5' UTR, CDS, 3' UTR; (2) Being on the same strand as its annotated gene. This filtering resulted in a final set of 640,675 binding motif locations around which PUM2 binding was assessed.

In addition to this set of filtered motif locations, a set of "random" sites were determined, which served as controls throughout. These sites were obtained by choosing 5,000,000 random start sites within the original set of genome locations. These random sites spanned the same number of nucleotides as the putative binding sites (11 nt). These 5 million sites were subsequently annotated and filtered exactly as the putative binding sites were, resulting in 76,137 "random" locations.

#### **Using the thermodynamic model to predict $\Delta\Delta G$ values of each putative binding site**

The 11-nt sequence of all motif locations ("binding" or "random") were each assessed for their predicted  $\Delta\Delta G$  using the full thermodynamic model (Figure 4A; 37°C). The sequence within each motif location was determined using the bedtools getfasta command and the hg38 genome build in fasta format.

This 11-nt window has three possible binding registers if no residues are flipped ( $\Delta\Delta G_{consecutive,1}$ ,  $\Delta\Delta G_{consecutive,2}$ ,  $\Delta\Delta G_{consecutive,3}$ ), in addition to other binding registers with one or two residues flipped (see Figure 4A). Each sequence was also assessed for the  $\Delta\Delta G_{noflip}$ , which represents the ensemble energy of the three  $\Delta\Delta G_{consecutive}$  values, with no contribution from any of the flipped binding registers.

#### **Determining expression of putative PUM2 binding sites**

RNA-seq expression data for K562 cell lines was obtained from the ENCODE project (Consortium, 2012). These data consisted of transcript-per-million (TPM) values for each ENSEMBL transcript across two replicates (<https://www.encodeproject.org/files/ENCFF272HJP/@@download/ENCFF272HJP.tsv> and <https://www.encodeproject.org/files/ENCFF471SEN/@@download/ENCFF471SEN.tsv>). The TPM values for each transcript were averaged across the two replicates, and the value for each Refseq transcript identifier was then determined using Ensembl Biomart for hg38. The TPM value for each Refseq transcript gave the relative expression of motif sites within that transcript, as assessed using the annotations from HOMER described above.

Only motif sites on transcribed genes (TPM > 0 in K562) were included in certain subsequent analyses, resulting in further filtering of the number of motif sites examined to 396,578 total sites.

#### **Obtaining eCLIP signal around putative PUM2 binding sites**

Enhanced UV crosslinking and immunoprecipitation (eCLIP) data for PUM2 protein in human K562 cells was obtained from ENCODE (Van Nostrand et al., 2016). Sequencing read alignments (in the form of a BAM file) were obtained for two replicate pulldown samples and one input sample which did not undergo antibody pulldown for PUM2 but was otherwise experimentally processed identically (<https://www.encodeproject.org/files/ENCFF786ZZB/@@download/ENCFF786ZZB.bam>, <https://www.encodeproject.org/files/ENCFF732EQX/@@download/ENCFF732EQX.bam>, <https://www.encodeproject.org/files/ENCFF231WHF/@@download/ENCFF231WHF.bam>). The published eCLIP data had already been processed to exclude PCR duplicates by collapsing sequencing reads with identical barcodes (Van Nostrand et al., 2016). Only alignments corresponding to the second sequencing read (read2) were kept, as the 5' end of this read corresponds to the nucleotide immediately following the putative crosslinking site (Van Nostrand et al., 2016). The alignments were obtained using the package samtools (version 0.1.19-96b5f2294a):

```
samtools view -bh -f 128 ${input_bam} > ${output_R2_bam}
```

This set of filtered alignments was used to determine the number of observed crosslinks (i.e., read2 start sites) on each strand at any position within the genome, using the package bedtools:

```
bedtools genomecov -ibam {R2_bam} -strand + -bg -5 > {output_bedgraph_plus}
```

```
bedtools genomecov -ibam {R2_bam} -strand - -bg -5 > {output_bedgraph_minus}
```

The number of crosslink sites (from eCLIP data) at each nucleotide position within each motif location was determined using the package pyatac ins (<https://nucleoatc.readthedocs.io/en/latest/pyatac/>). Only crosslink sites on the same strand as the motif were included in the total count. The number of reads starting 55 nt upstream and extending to 25 nt downstream of the motif location center (80 nt total; Figure S7L) were summed for each sample, corresponding to the motif site's eCLIP read count; this window accounted for the asymmetrical observed distribution of crosslink sites around PUM2 consensus motifs. eCLIP signal for each motif site was determined as the sum of eCLIP read count for the two replicates, divided by the relative expression of that motif site. Similarly, eCLIP input for each motif site was the eCLIP read count for the input sample, divided by the relative expression of that motif site.

The median eCLIP signal and input around sites identified as ‘background’ sites was determined from sites with predicted  $\Delta\Delta G > 4.5$  kcal/mol, regardless of whether the site originated from the “binding” or “random” motif locations. The eCLIP signal (or input) values were divided by the ‘background’ signal (or input) value to obtain the eCLIP signal (or input) enrichment above the background expectation.

To assess the eCLIP occupancies of sites with and without flipped residues (Figure 6B), sites were defined as containing flipped residues if their predicted  $\Delta\Delta G$  value using the full thermodynamic model (Figure 3F) was lower than the  $\Delta\Delta G$  value predicted by the additive consecutive model by more than 0.5 kcal/mol.

While the eCLIP data (Van Nostrand et al., 2016) enabled us to perform initial tests of thermodynamic predictions for PUM2 *in vivo*, future tests will be needed to assess factors that lead to occupancy variation at the level of individual RNAs and to confidently distinguish variation caused by biological factors versus technical artifacts (Wheeler et al., 2018). Whereas median eCLIP occupancies are well predicted by thermodynamics, there is wide variation in eCLIP read coverage between sites of identical sequence or predicted affinity (Figure S7M), either because of crosslinking bias or yet-to-be-identified biological and methodological factors. Improvements in individual-RNA signal intensity and quantitative controls will allow dissection of these factors.

#### Assessing secondary structure around motif sites

Consensus motif sites ( $\Delta\Delta G^{\text{pred}} < 0.5$  kcal/mol), comprising 4,816 non-overlapping sites, were assessed for local secondary structure occluding the binding site. The sequence around each motif site was determined using bedtools getfasta. Multiple different lengths of flanking regions were included in this assessment (10 nt, 20 nt, or 80 nt on either side of the motif site). An additional line within the sequence fasta file gives the constraint that the binding site (i.e., the first 8 nt of the motif site, given the weak interaction at position 9) remains unpaired. Using the program RNAfold (v2.1.8 (Lorenz et al., 2011)), the ensemble energy was determined for each sequence:

```
cat ${input_fasta} | RNAfold-noPS -p0 -C -T37 > ${output_values_wconstraint}
cat ${input_fasta} | RNAfold-noPS -p0 -T37 > ${output_values_noconstraint}
```

The difference in ensemble free energy with and without the constraint gives the accessibility of that site:  $\Delta\Delta G_{\text{ss}} = \Delta G_{\text{no\_constraint}} - \Delta G_{\text{constraint}}$  (see also Accounting for RNA structure above). Note that the thermodynamic linkage between RNA folding and RBP binding, depicted in Figure 2C, applies fundamentally to any RBP, as the effects of RNA structure on binding only depend on the relative free energies of the accessible and occluded RNA states (see, e.g., (Hackermüller et al., 2005; Li et al., 2010; Taliaferro et al., 2016) for examples of structure effects on other RBPs). Thus, the weaker than predicted structure effects on PUM2 binding *in vivo* must reflect cellular factors that destabilize RNA structure, rather than properties specific to PUM2. Current limitations of eCLIP-based structure analysis include that, in the presented case, the analysis only provides insight into local structural context around PUM2 sites (i.e., cytosolic and primarily located in 3'UTRs), under the conditions of an eCLIP experiment; further, the analysis relies on structural predictions by nearest-neighbor algorithms, which have limited accuracy (Becker et al., 2019a).

#### Enrichment of PUM2 sites within 3'UTRs

Sites derived from the PUM2 PWMs (described in Analysis of *in vivo* crosslinking data above; not filtered for being expressed in K562 cells) were divided into bins based on the predicted  $\Delta\Delta G$ , and the fraction of motifs within each bin that were annotated as 5' UTR, CDS, or 3' UTR was determined as described above (i.e., using HOMER), and are shown in Figure 6D. Enrichment for transcript annotations of motif sites (Figure 6E) was determined relative to the annotation frequencies of “random” locations.

#### Modeling the cellular PUM2 binding landscape

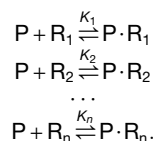
To assess the distribution of PUM2 across cellular RNA sites, we determined the numbers of each 9-mer, 10-mer and 11-mer sequence in the human transcriptome (representing consecutive sites and sites containing one or two flipped residues). For simplicity, here we assumed equal expression of all protein-coding transcripts, with sequences obtained from GENCODE (genome release GRCh38.p12; ‘Protein-coding transcript sequences’ fasta file) (Harrow et al., 2012). Absolute numbers of each binding site were determined by normalizing the nucleotide count in the above transcriptome file to match the estimated mRNA nucleotide count in a single human cell ( $8.9 \times 10^8$  nucleotides, corresponding to  $\sim 0.5$  pg mRNA per cell) (Livesey, 2003; Marinov et al., 2014; Tang et al., 2011). These numbers can be adjusted to account for cell-specific variation in total mRNA levels and differential expression based on publicly available RNaseq data (Consortium, 2012).

The number of PUM2 molecules per cell was estimated at 10,000, based on published numbers of 2,000 and 18,000 in HCT116 and HeLa cells, respectively (Lee et al., 2016; Nagaraj et al., 2011).

To calculate the distribution of cellular protein bound across the different mRNA sequences, we first calculated PUM2 relative affinities for each 9–11-mer site using our thermodynamic model. The affinities for consecutive 9-mer sites were calculated using the binding and coupling terms in Table 1; to determine affinities for sites containing flipped residues, we calculated the ensemble affinities of the four possible registers with one single-nucleotide flip (Figure 4A; 10-mer sites); and the ensemble of the four possible registers with a two-nucleotide flip and six possible registers of two single-nucleotide flips (11-mer sites), using the terms in Table 1.



PUM2 occupancies for each RNA species were calculated using an equilibrium competition model, where the occupancy of a given RNA species ( $P \cdot R_i$ ) is a function of protein abundance ( $P$ ), and the affinities and abundances of all RNA ( $R$ ) sites:



The fraction of total protein bound to RNA sequence  $R_1$  equals:

$$\frac{[P \cdot R_1]}{[P]_{\text{total}}} = \frac{K_1 [P] [R_1]}{[P] + K_1 [P] [R_1] + K_2 [P] [R_2] + \dots + K_n [P] [R_n]} = \frac{K_1 [R_1]}{1 + K_1 [R_1] + K_2 [R_2] + \dots + K_n [R_n]} = \frac{K_1 [R_1]}{1 + \sum_{i=1}^n K_i [R_i]} \quad (\text{Eq. 14})$$

We used affinities predicted for each RNA by our thermodynamic model:

$$K_i = e^{-\Delta G_i / RT} \quad (\text{Eq. 15})$$

where  $\Delta G_i = \Delta G_{WT} + \Delta \Delta G_i$ ;  $\Delta G_{WT}$  is the measured affinity for the UGUUAUUAU reference sequence at 37°C (−12.1 kcal/mol), and  $\Delta \Delta G_i$  is the relative free energy for binding to sequence  $R_i$  ( $\Delta \Delta G_i$ ) predicted by our thermodynamic model.

To convert the sequence counts into concentrations, we used the cell volume of  $10^{-12}$  L (Fujioka et al., 2006). Given the much greater number of RNA sites than the number of cellular PUM2 molecules (78,000 consensus UGUA[ACU]AUAN sites alone versus 10,000 PUM2 molecules), we assume that most RNA sites are unbound, i.e., that  $[R_i] \approx [R_i]_{\text{total}}$ . [This assumption will not hold at very high protein concentrations or for certain RBPs with very high specificity; these alternate regimes can be readily simulated using KinTek Explorer or similar software (Johnson et al., 2009).]

The occupancies plotted in Figure 6H correspond to the amount of PUM2 bound to each RNA species (i.e., fractional protein occupancy from Equation 14 multiplied by the total amount of protein):

$$[P \cdot R_1] = [P]_{\text{total}} \times \frac{K_1 [R_1]}{1 + \sum_{i=1}^n K_i [R_i]} \quad (\text{Eq. 16})$$

Concentrations of occupied sites were converted into the number of protein-bound sequences as follows:  $[P \cdot R_1] \times N_A \times V_{\text{cell}}$ , where  $N_A$  is Avogadro's number and  $V_{\text{cell}}$  is the cell volume.

The bars in Figure 6H denote the sum of occupancies for all 9-mer RNA species containing the indicated numbers of nonconsensus residues (blue) and 10–11-mer species with flipped residues (green).

Fractional occupancies of each RNA sequence were determined (using the definition of the amount of bound RNA from Equation 14), as follows:

$$\frac{[P \cdot R_1]}{[R_1]_{\text{total}}} = \frac{[P]_{\text{total}} \times K_1 [R_1]}{[R_1]_{\text{total}} \times \left(1 + \sum_{i=1}^n K_i [R_i]\right)} \approx \frac{[P]_{\text{total}} \times K_1}{1 + \sum_{i=1}^n K_i [R_i]} \quad (\text{Eq. 17})$$

The fractional occupancy of consensus sequences calculated using Equation 17 and the published cellular amounts of PUM2 and mRNA (see above) was 3.4%. We emphasize that these binding predictions are based on 'typical' expression levels, which suggest a large excess of consensus RNA sites over the cellular PUM2 level and over the  $K_D$ . As a result, none of the RNA sites are predicted to be saturated with PUM2 and the occupancies should linearly scale with predicted affinity; this concentration regime is supported by the linear relationship between predicted affinities and eCLIP occupancies (Figure 6A). Nonetheless, given the changes in PUM1 and PUM2 expression across tissues and during development (reviewed in (Goldstrohm et al., 2018)), as well as cellular changes in expression and accessibility of RNA, PUM1 and PUM2 expression may in some cell types reach saturating levels. This saturating binding to consensus sites would lead to poorer discrimination between consensus and nonconsensus sites and an even greater fraction of PUM2 being bound to nonconsensus sites (not shown).

### Occupancy prediction algorithm

A script for predicting PUM2 occupancy on any RNA sequence (see Figure 6G) can be found on <https://github.com/pufmodel>. The script accepts any RNA sequence in fasta format and predicts PUM2 occupancies relative to the UGUUAUUAU consensus at each site along the sequence based on our thermodynamic model. The algorithm currently assumes a linear relationship between affinity and occupancy, as explained above in Modeling the cellular PUM2 binding landscape, as we do not expect saturating binding *in vivo* in the presence of the large excess of tight RNA binding sites over cellular protein. Currently the script provides normalized occupancies relative to the consensus sequence; to determine fractional RNA occupancies within the cell, experimental PUM2 and RNA concentrations will need to be considered. The fractional occupancies in the example shown in Figure 6G have been calculated based on our landscape model and the estimated amounts of PUM2 and mRNA in a typical cell (see Modeling the cellular PUM2 binding landscape).

### Predicting PUM1 and PUM2-mediated regulation

To assess how predicted PUM1 and PUM2 occupancies related to regulation of mRNA abundance, we analyzed a previously published dataset that measured gene expression changes in response to simultaneous siRNA knockdown of PUM1 and PUM2 in human HEK293 cells (Bohn et al., 2018). This study labeled each gene as significantly upregulated, downregulated, or unchanged (Table S4 of (Bohn et al., 2018); 19219 genes total). Different entries with the same gene name were aggregated by only keeping the first entry with that gene name (19135 genes). Predicted relative occupancies were determined by identifying all putative PUM2 binding sites within the 3' UTR, CDS and 5' UTR regions of each mRNA (using labels from *Determining binding sites within the transcriptome* in the [Analysis of in vivo crosslinking data](#) section) and integrating the occupancies across all sites in a given region:

$$\text{Relative occupancy} = \sum_i^N e^{-\Delta\Delta G_i/RT} \quad (\text{Eq. 18})$$

Here, occupancy is calculated relative to the UGUUAUUAU consensus, and assumes subsaturating binding (see [Modeling the cellular PUM2 binding landscape](#)). Genes with no putative PUM2 binding sites in any part of the mRNA were not included in the analysis ( $n = 3886$ ).

To assess if PUM1 and PUM2 binding to different mRNA regions contributed differently to the regulation of mRNA expression, Receiver Operating Characteristic (ROC) plots were generated (Figure S7E). The true positive and false positive rates were assessed for each predicted occupancy value; predicted positives were those genes with occupancy greater than or equal to that occupancy value within the indicated region (3' UTR versus CDS/5' UTR), and true positives were those that were significantly upregulated with PUM1 and PUM2 depletion (i.e., repressed by PUM1 and PUM2).

To compare the thermodynamics-based predictions to those based on eCLIP data in K562 cells, two additional ROC plots were generated, in which predicted positives are those genes with 1) at least a certain number of eCLIP peaks, or 2) at least a certain number of eCLIP reads, normalized for expression in K562 cells. Each is described in more detail below.

To determine if the number of eCLIP peaks in the 3' UTR region was predictive of regulation, the two replicate datasets of PUM2 eCLIP peak locations were downloaded from ENCODE, concatenated and sorted (Van Nostrand et al., 2016). HOMER was used to identify the gene and region associated with each peak (i.e., intron, exon, 3' UTR, etc.). Genes with no peaks were included in the analysis.

To determine if the number of eCLIP reads per 3' UTR was predictive of regulation, eCLIP reads were summed within any putative binding site of a gene's 3' UTR, as described in the [Analysis of in vivo crosslinking data](#) section (*Obtaining eCLIP signal around putative PUM2 binding sites*). The reads in each of the two eCLIP replicates were summed, and the number of eCLIP reads per 3'UTR was divided by the expression of that gene in K562 cells (in TPM, as described in [Analysis of in vivo crosslinking data](#) (*Determining expression of putative PUM2 binding sites*)). Genes with no associated putative PUM2 binding site were not included in the analysis. The number of normalized CLIP reads per gene was shown to be a moderate predictor of the gene expression change with PUM1 and PUM2 knockdown, comparable to thermodynamics-based predictions (Figure S7F). Note that eCLIP and PUM1 and PUM2 knockdown experiments were performed in different cell types (K562 and HEK293, respectively), which may affect these comparisons.

### RNA Bind-n-Seq analysis

To independently test the thermodynamic model using a large dataset of sequences not present in our library, we analyzed enrichments of all 11-mer sequences in the publicly available RNA Bind-n-Seq (RBNS) dataset for human PUM1 (Consortium, 2012; Dominguez et al., 2018). We focused on the data for the lowest PUM1 concentration, 5 nM, which provided the greatest dynamic range of enrichments over the no-protein input. Analysis of data obtained at higher PUM1 concentrations (20–1300 nM) indicated declining enrichments for representative single mutants, suggesting saturating PUM1 binding at the low RBNS experimental temperature of 4°C. Enrichments of 11-mer sequences were calculated over the no-PUM1 input as follows:

$$\text{Enrichment}_i = \frac{\text{frequency of } 11\text{mer}_i(5 \text{ nM PUM1})}{\text{frequency of } 11\text{mer}_i(\text{input})} \quad (\text{Eq. 19})$$

where frequency indicates the number of occurrences of each 11-mer in the dataset divided by the total number of 11mers in the dataset. 99.98% of all possible 11mers ( $n = 4,193,377$ ) were represented in both input and PUM1 samples.

The log10 enrichments were compared to the relative affinities predicted for each 11-mer sequence by our thermodynamic model at 4°C (Figure 4A). Analysis of median enrichments across 0.5 kcal/mol bins revealed above-background enrichments for 11-mer sequences with predicted  $\Delta\Delta G$  values of up to 3.5 kcal/mol. Thus, further quantitative comparisons were based on 11mers within this range (Figure S7D).

To compare the performance of the thermodynamic model for 11mers that were versus were not present in our RNA-MaP library, we calculated the coefficients of determination ( $R^2$ ) between predicted  $\Delta\Delta G$  values and log10 RBNS enrichments for each set. The RNA-MaP variants were defined as those 11mers that were present in the set of the 5206 unstructured library variants used for global fitting of the thermodynamic model. Given the non-uniform distribution of 11mers across the affinity bins (e.g., 50.3% of the RBNS 11mers with  $\Delta\Delta G^{\text{pred}} \leq 3.5$  kcal/mol were in the 3.0–3.5 kcal/mol bin, while the RNA-MaP variants were distributed more evenly; Table S6), we randomly subsampled the data to have the same number of 11mers in each  $\Delta\Delta G^{\text{pred}}$  bin (bin size: 0.5 kcal/mol). The sample size ( $n = 101$ ) corresponded to the number of variants in the bin with the fewest variants. 100 rounds of random

subsampling were performed using the pandas DataFrame.sample() function. The median and bootstrapped 95% confidence intervals of the resulting  $R^2$  values were determined using the Python modules scipy.stats and scikits.bootstrap. The bootstrapped 95% confidence intervals were [0.737, 0.743] and [0.747, 0.754] for 11mers that were or were not present in our RNA-MaP library, respectively.

While the RBNS analysis allowed us to assess the performance of the thermodynamic model beyond the library tested by RNA-MaP, there are critical experimental differences that contribute to the observed significant spread between predicted affinities and observed RBNS enrichments. For example, RBNS was performed at 4°C, using long, 65 nt oligonucleotides that are predicted by Vienna RNAfold to form stable structures, and enrichment is expected to be biased against highly structured sequences. Inspection of variants that were systematically less enriched than predicted by thermodynamics revealed that these were dominated by 11mers containing multiple G residues.

In addition to stabilizing RNA structure, the low temperature (4°C) may preclude equilibration in the course of the 2 h experiment, by slowing PUM1 dissociation. (E.g., measurements of PUM2 dissociation from the consensus sequence at 0°C indicate a dissociation half-life of 20 h (Vaidyanathan et al., 2017).) Another key limitation is that RBNS is a disruptive technique, and the washing steps that follow the PUM1-RNA incubation may perturb binding equilibria.

11mers that displayed high enrichment values despite low predicted affinities could be explained by partially overlapping consensus sites present in the same RBNS oligonucleotide. This was supported by a strong enrichment for partial consensus sites among these highly enriched 11mers. E.g., comparison of sequences of 11mers that had predicted  $\Delta\Delta G$  values greater than 2.5 kcal/mol, and that were versus were not enriched >10-fold over input (Figure S7D) revealed that 13.7% of variants with >10-fold enrichment contained the NNNNUGUA[ACU]AU sequence and 20.4% contained the NNNNNUGUA[ACU]A sequence. In contrast, only 0.0030% and 0.050% of sequences with enrichment of <10-fold contained these partial consensus sites. While alternative binding sites within the same RNA oligonucleotide are straightforward to account for in RNA-MaP analysis, accounting for neighboring sites in RBNS data is time- and computationally intensive Lambert et al., 2014. Given the above limitations of available RBNS data for PUM1, this analysis was omitted herein.

## DATA AND SOFTWARE AVAILABILITY

Thermodynamic binding data generated in this study are available for download (Table S5).

Key scripts for analyses reported herein have been deposited to github, as indicated in the Key Resources Table.

**Molecular Cell, Volume 74**

**Supplemental Information**

**A Quantitative and Predictive Model**

**for RNA Binding by Human Pumilio Proteins**

**Inga Jarmoskaite, Sarah K. Denny, Pavanapuresan P. Vaidyanathan, Winston R. Becker, Johan O.L. Andreasson, Curtis J. Layton, Kalli Kappel, Varun Shivashankar, Raashi Sreenivasan, Rhiju Das, William J. Greenleaf, and Daniel Herschlag**

# Supplemental Figures and Tables

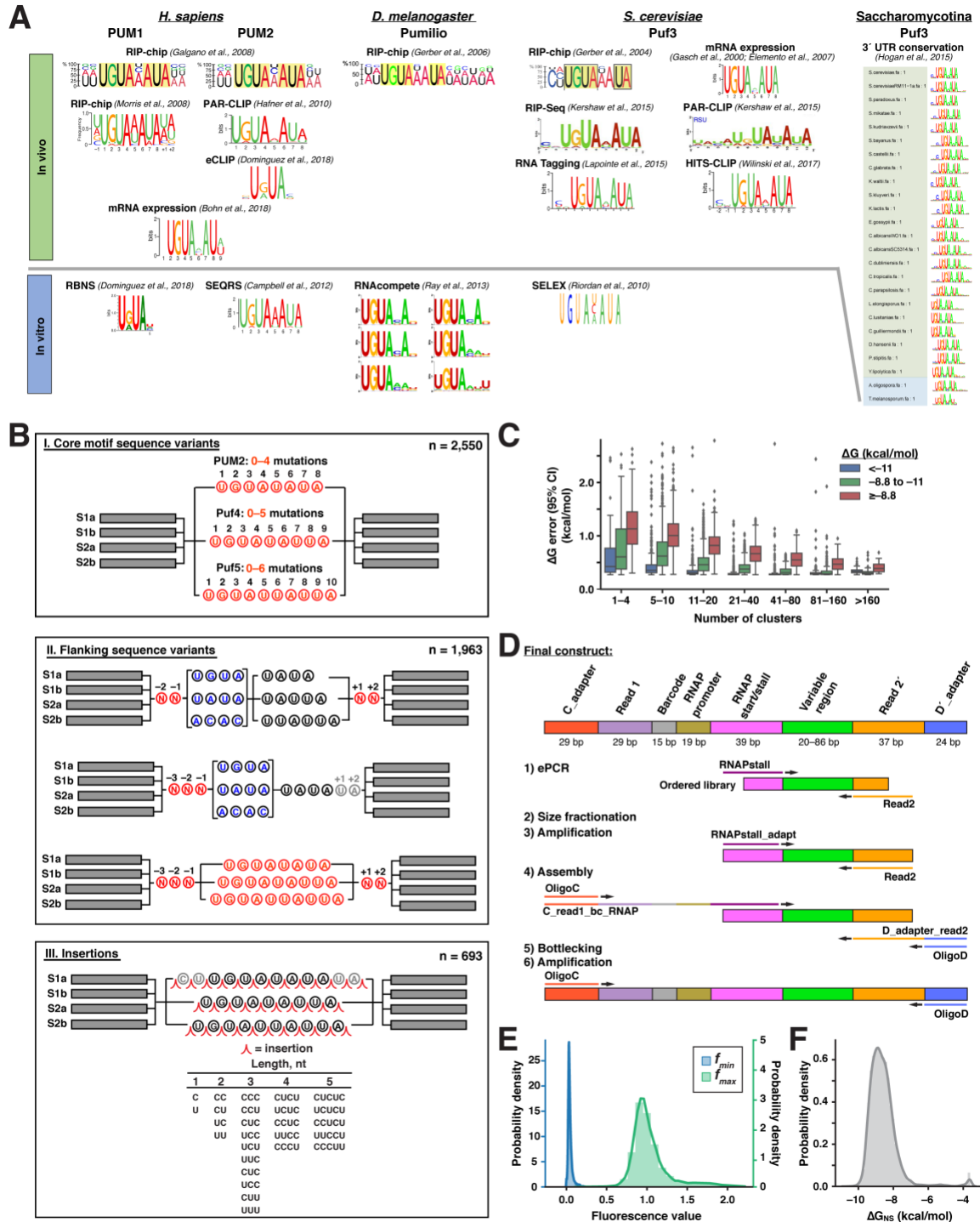


**Figure S1. RNA Array Library Design, Preparation and Experiments, Related to Figure 1 and STAR Methods**

(A) Representative sequence motifs previously identified for human PUM1, PUM2 and orthologous PUF proteins (Bohn et al., 2018; Campbell et al., 2012; Dominguez et al., 2018;

Elemento et al., 2007; Galgano et al., 2008; Gasch et al., 2000; Gerber et al., 2004; Gerber et al., 2006; Hafner et al., 2010; Hogan et al., 2015; Kershaw et al., 2015; Lapointe et al., 2015; Morris et al., 2008; Ray et al., 2013; Riordan et al., 2011; Wilinski et al., 2017). Copyright information for motifs that were reproduced from original figures: Kershaw et al., 2015, Hogan et al., 2015—CC BY 4.0 (<http://creativecommons.org/licenses/by/4.0/>); Gerber et al., 2006—Copyright (2006) National Academy of Sciences. Human PUM1 RBNS motif was obtained from the ENCODE database (Consortium, 2012; Dominguez et al., 2018); *D. melanogaster* Pumilio motifs were obtained from the CISBP-database (Ray et al., 2013).

(B) RNA libraries used in this study. Three broad categories of PUM2 binding site variants were designed: (I) mutations in the core binding site; (II) flanking sequence variants; (III) insertions. Each variant was represented in 2–4 scaffolds (S1a–S2b; Figure 1B). Within each category, the design was based on the previously established consensus motif of PUM2 and its orthologs; substantial additional sequence variation was achieved by applying the same types of perturbations to the consensus motifs of related PUF proteins, *S. cerevisiae* Puf4 and Puf5 (Gerber et al., 2004; Hogan et al., 2008; Hogan et al., 2015; Riordan et al., 2011; Wilinski et al., 2015). To prevent a preponderance of weak binders, in the mutation library (I) no more than two mutations were allowed in the highly conserved UGUA core of the PUF motifs. Numbers of variants in each category that were used for model fitting (Figure 3E,F) are indicated. Total numbers of designed variants and numbers of variants passing each criterion for inclusion in the final, high-quality data set are provided in Table S5.

(C) Affinity and number of clusters per variant affect measurement certainty. Box plots show measurement uncertainties from PUM2 replicate 1, with the box indicating the interquartile range, the whiskers indicating the minimum and maximum values and the points indicating outliers. Only variants with  $\geq 5$  clusters and  $\Delta G$  values below  $-8.8$  kcal/mol were included in subsequent analyses (see STAR Methods).

(D) Preparation of DNA array library. See STAR Methods and Table S7 for detailed sequence information and description of individual steps.

(E, F) Distribution of initial fit parameters for variant-independent parameters  $f_{\min}$ ,  $f_{\max}$ , and  $\Delta G_{\text{NS}}$ . (E) Histogram of the initial per-variant values for  $f_{\min}$  (blue) and  $f_{\max}$  (green) for variants that reached near-saturation of binding ( $>95\%$  bound at highest concentration based on initial per-variant  $K_{\text{D}}$ ) and that met other criteria for high-confidence binders during initial fitting, as defined in STAR Methods. (F) Histogram of the initial per-variant values for  $\Delta G_{\text{NS}}$  ( $= RT \ln K_{\text{D,NS}}$ ; STAR Methods). Values for PUM2 replicate 1 are shown.

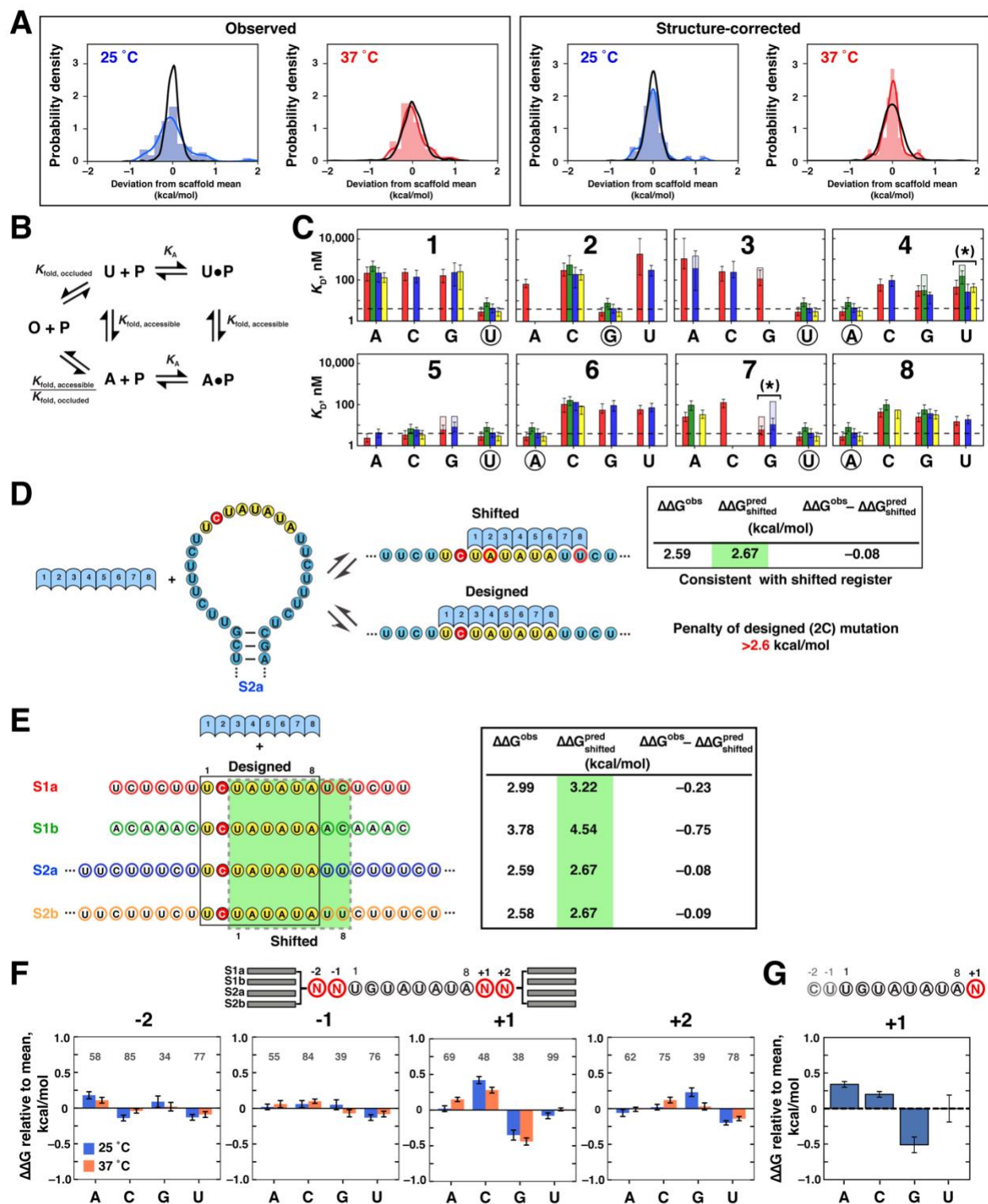


**Figure S2. Analysis of Single-Mutant Variant Binding to PUM2, Related to Figure 2**

(A) Assessing significance of scaffold differences. For each binding site variant (single mutants and UGUAUAUA consensus), we determined the deviations of individual scaffold affinities from

the scaffold mean for that variant. The distribution of these deviations was then compared to the distribution expected from experimental error (black line). The panels show distributions at 25°C (blue) and 37°C (red), before (left) and after (right) accounting for structure effects, as predicted by RNAfold ((Lorenz et al., 2011); see STAR Methods). A summary of the standard deviations of the displayed distributions is shown in Figure 2B.

(B) Model for accounting for RNA structure effects on PUM2 binding. U: unfolded RNA; P: protein; A: accessible RNA (i.e., structured RNA with the PUM2 binding site accessible); O: occluded RNA (i.e., PUM2 binding site occluded by base-pairing). A and O represent ensembles of the respective states; see Figure 2C).  $K_A$ : PUM2 association constant for the unstructured binding site (assumed to be the same for binding to U and A, but no protein binding occurs to O);  $K_{\text{fold,accessible}}$ : equilibrium constant for RNA folding from the unfolded state to the ensemble of structures in which the PUM2 binding site is accessible (determined by constraining the binding site to the single-stranded state in RNAfold;  $K_{\text{fold,accessible}} = e^{-\Delta G_{\text{accessible}}/RT}$ );  $K_{\text{fold,occluded}}$ : equilibrium constant for RNA folding from the unfolded state to the ensemble of structures in which the PUM2 binding site is occluded by structure.

(C) PUM2 affinities for UGUAUAUA single mutants at 37°C. Solid bars indicate mutant affinities after accounting for structure effects, and transparent regions indicate predicted structure effects. Asterisks indicate mutants for which affinities measured in different scaffolds were significantly different (10% FDR) prior to accounting for structure effects (differences between total bar heights). No significant differences remained after accounting for structure effects using RNAfold. Error bars indicate 95% CIs of the measured affinity values.

(D) Assessment of alternative binding registers. Example of preferential binding in an alternative register accompanying a destabilizing mutation in the designed binding site. Affinity effects are shown as  $\Delta\Delta G$  values, relative to the average affinity for the UGUAUAUA consensus across scaffolds. The predicted  $\Delta\Delta G$  for the alternative register corresponds to the sum of the  $\Delta\Delta G$  values for the two nonconsensus residues, 2A and 8U (red outlines), assuming energetic independence. Given that the observed  $\Delta\Delta G$  ( $\Delta\Delta G^{\text{obs}}$ ) matches the prediction for the alternative register, the measurement only establishes a lower limit for the penalty of the intended, 2C, mutation.

(E) Observed and predicted  $\Delta\Delta G$  values for the best alternative register ( $\Delta\Delta G_{\text{shifted}}^{\text{pred}}$ ) in each of the four scaffolds for the 2C variant (other variants with predicted alternative registers are listed in Table S1). The close agreement of alternative register predictions with observed affinities in the S1a, S2a, and S2b scaffolds suggests predominant binding in the shifted register, whereas the 0.75 kcal/mol difference in the S1b scaffold suggests preferential binding in the intended register, such that the observed value of 3.78 kcal/mol reflects the real effect of the 2C mutation.

(F) Flanking sequence effects on PUM2 binding. *Top*: Library design. Two bases upstream and downstream from the UGUAUAUA consensus were randomized ( $N = A/C/G/U$ ;  $n = 256$ ) and the resulting sequences were embedded in 2–4 scaffolds each. *Bottom*: Effects of each base at the indicated positions relative to the average affinity. The effects were determined by calculating the average affinity of variants containing the indicated base (regardless of the identities of other flanking bases) and subtracting the mean of all four bases. Error bars indicate 95% CI of the mean. Only variants with predicted structural effects  $< -0.5$  kcal/mol were included, and the numbers of variants containing each base are indicated above the bars. Blue and orange bars indicate the sequence effects at 25°C and 37°C, respectively. The observed sequence effects at positions -2, -1 and +2 are small and are further dampened at 37°C, suggesting that residual structural effects are responsible for the small observed effect. The strongest effect was observed



at position +1, and the observed preference for G was maintained at 37°C, indicating a weak, base-specific interaction.

(G) Gel-shift measurements of sequence effects at position +1. *Top*: Oligonucleotide design; N = A/C/G/U. *Bottom*: Effects of each base relative to the mean affinity for all four variants. Averages and standard errors from two replicate experiments are shown.

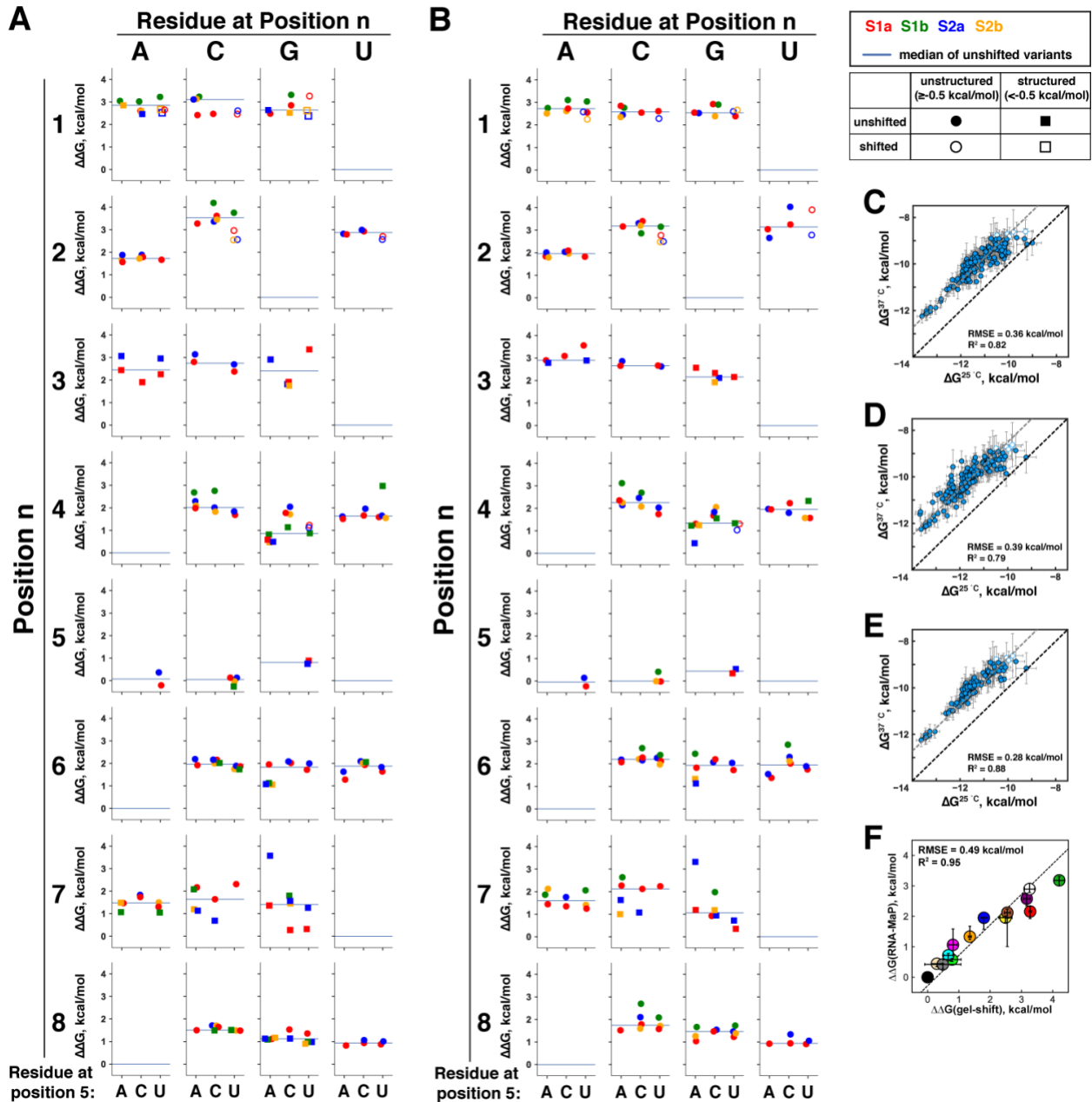


**Figure S3. Determination of Single Mutant Penalties, Related to Figure 2**

(A, B) Single mutation effects on PUM2 binding across backgrounds of different position 5 identities (5 = A/C/U) at 25°C (A) and 37°C (B). Symbols indicate the  $\Delta\Delta G$  values for each mutation relative to the weighted mean of UGUA[A/C/U]AUA affinities across scaffolds (color-coded). As shown in Figure 2D and previously (Lu and Hall, 2011), residues A, C and U are bound with identical affinities at position 5, and other positions show high consistency of mutational penalties measured in 5A/C/U backgrounds, consistent with energetic additivity with respect to position 5. Thus, mutational penalties from all three backgrounds were used for determination of single mutant penalties, with median  $\Delta\Delta G$  values indicated by horizontal lines. Circles indicate unstructured variants, while squares denote variants with predicted structure effects greater than 0.5 kcal/mol, and the displayed values correspond to structure-corrected affinities. Open symbols

indicate variants that have predicted alternative registers within 1 kcal/mol from the observed  $\Delta\Delta G$  value; these variants were not included in determining the median. None of the variants in the 5A/C backgrounds were predicted to have alternative binding registers.

(C–E) Scatterplots of RNA single mutant affinities for PUM2 at 25°C and 37°C. (C) Observed  $\Delta G$  values for single mutants in position 5A/C/U backgrounds ( $n = 161$ ). Open symbols indicate variants with affinities outside the reliable affinity threshold ( $-8.8$  kcal/mol; not included in RMSE and  $R^2$  determination). The grey dashed line indicates the mean offset between values measured at 25°C and 37°C, corresponding to a  $(20 \pm 10)$ -fold decrease in affinity at 37°C. Horizontal error bars indicate weighted errors of replicate measurements at 25°C; vertical error bars indicate 95% CIs of the measured affinities at 37°C. (D)  $\Delta G$  values after accounting for predicted structure (RNAfold). The poorer correlation than observed in part C is likely due to limited accuracy of structure predictions (Becker et al., 2019a). (E) Correlation of observed  $\Delta G$  values at 25°C and 37°C for variants with no predicted structure ( $\Delta G_{\text{fold}} > -0.5$  kcal/mol;  $n = 107$ ). The correlation approaches that of replicate measurements (Figure 1E; RMSE = 0.26 kcal/mol;  $R^2 = 0.96$ ).

(F) Comparison between single mutant affinities determined by gel-shift measurements and by RNA-MaP (similar to Figure 2F, but the RNA-MaP values correspond to 37°C rather than 25°C measurements of PUM2 binding). 1C: purple, 2A: yellow, 2C: green, 3A: white, 3G: red, 4G: orange, 4U: blue, 5G: wheat, 7C: brown, 7G: magenta, 9A: lime, 9C: cyan, 9U: grey. The RNA-MaP values are medians and 95% CIs of individual mutation penalties in 5A/C/U backgrounds, determined after accounting for secondary structure and shifting. The gel-shift values are averages and 95% CIs from 2–4 measurements. The better agreement of gel-shift values with 37°C than with 25°C RNA-MaP values (Figure 2F) is consistent with small structural effects on RNA-MaP-derived values at 25°C.

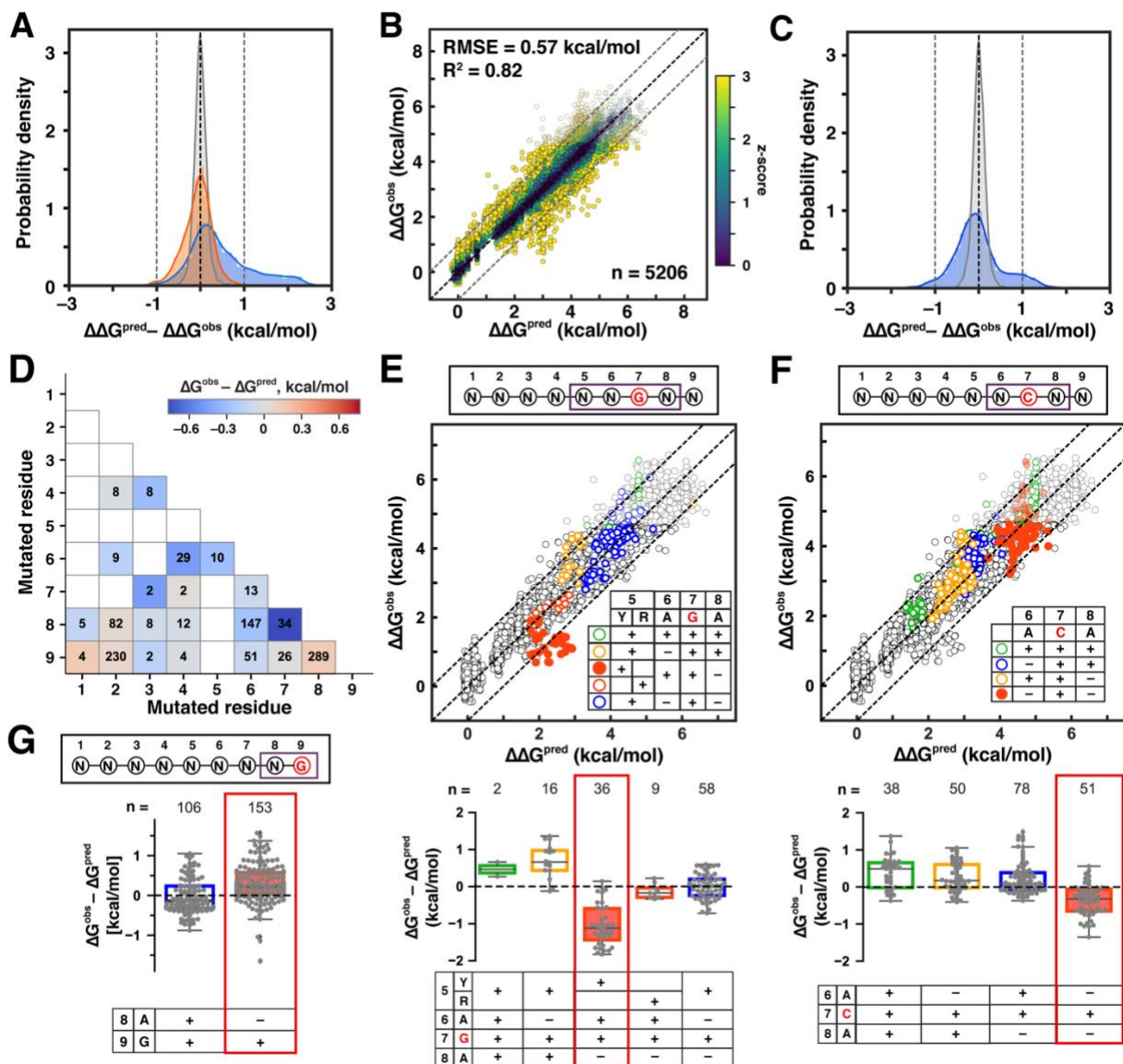


**Figure S4. Developing a Predictive Model for PUM2 Specificity, Related to Figure 3**

(A) Distribution of differences between model predictions and observed affinities through PUM2-binding model development. Blue: additive consecutive model (Figure 3A); orange: final model including flipping and coupling terms (Figure 3F); grey: the distribution of standard errors of measured  $\Delta\Delta G$  values. Coupling did not noticeably affect the distribution, so the additive nonconsecutive model without coupling (Figure 3E) is not displayed.

(B) Global fit to the additive consecutive model. Parameter constraints were identical to those used for fitting the additive nonconsecutive model (Figure 3E) and corresponded to the 95% confidence intervals from single mutant measurements (Figure 2E) or  $\pm 0.4$  kcal/mol, whichever was greater. Scatter plot of the predicted versus observed  $\Delta\Delta G$  values is shown. The points are colored based on their z-scores for the deviation from predicted value (see Figure 3A). The black dashed line indicates perfect agreement with prediction, and dashed grey lines denote 1 kcal/mol deviation from predictions. While the additive consecutive model performed considerably better with globally fit parameters than with experimentally determined single mutant penalties (Figure

3A), there was substantial asymmetry and ten percent of variants had predicted affinities >1 kcal/mol from the observed value (versus 0.00% expected from measurement error); see part C.

(C) Blue: distribution of differences between values predicted by the additive consecutive model (using parameter values determined by global fit; part B) vs. observed values; grey: distribution of standard errors of measured affinities, as in part A.

(D) Double mutant coupling at 25°C. Colors indicate the difference of observed  $\Delta\Delta G$  values ( $\Delta\Delta G_{\text{obs}}$ ) from the sum of  $\Delta\Delta G$  values for the individual mutations ( $\Delta\Delta G_{\text{pred}} = \Delta\Delta G_1 + \Delta\Delta G_2$ ). Double mutants were defined as all sequences differing from the UGUA[A/C/U]AUAU reference sequence at two positions and predicted to be in the most favorable register with no flips (STAR Methods); only variants with predicted structure effects of <0.5 kcal/mol were included. Numbers of variants containing each combination of mutations are shown inside the respective boxes; only mutants represented by more than one variant in our library are shown. White boxes indicate absence of the respective mutants in the best register in our unstructured library: these absences are primarily due to the highly destabilizing effects of mutations in the 5' half of the motif, which in combination with a second mutation lead to binding outside our reliably measurable range and/or to shifting of the preferred binding site to an alternative binding register; low representation of 5G-containing mutants is due to predicted structure.

(E) Coupling between the 7G mutation and adjacent positions, assessed as the extent to which measured affinities for variants with the indicated residue combinations (inset) deviate from predicted values. The predictions are based on the additive nonconsecutive model (Figure 3E). All sequences containing the indicated combination of residues in the predicted best consecutive register were considered. Black residues in the inset table indicate consensus residues. The top panel shows the variants overlaid on the scatterplot of predicted and observed values for the entire library (same as Figure 3E). The box plots in the bottom panel show the distributions of differences from predicted values for each group of variants. The coupling term that was incorporated in the final model is highlighted by solid red circles (top) and red outline (bottom). To avoid overfitting, only most pronounced instances of apparent coupling were included in the final model.

(F) Coupling between the 7C mutation and flanking residues, as in *E*.

(G) Coupling between positions 8 and 9. As in *E* and *F*, coupling was assessed as the extent to which affinities for variants with the indicated residues deviated from predicted values. The panel illustrates the loss of the small stabilizing effect of 9G when position 8 is mutated (i.e., not A).

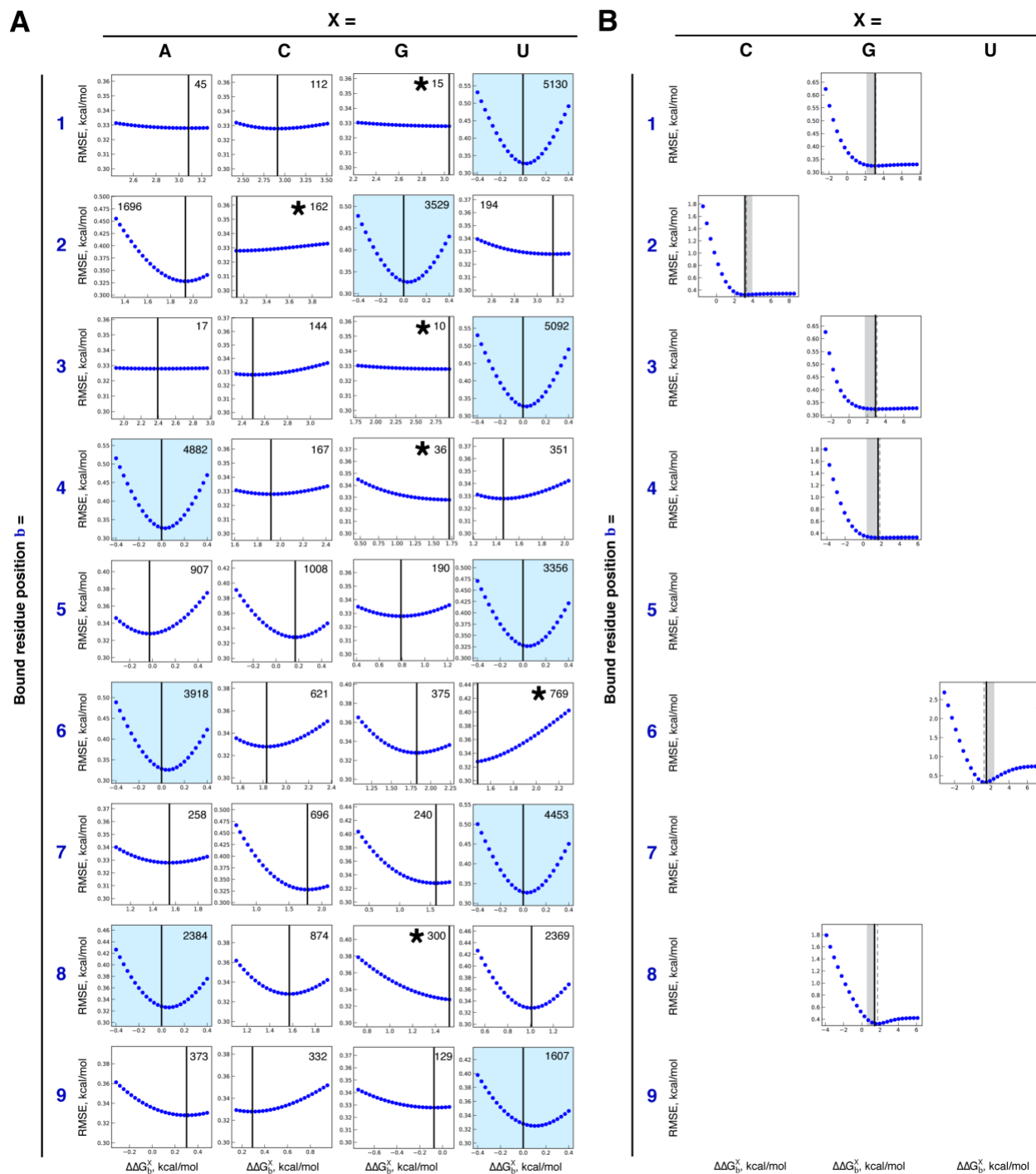


**Figure S5. RMSE Dependence on Individual Fit Parameters in the Additive Nonconsecutive Model Including Coupling (Bound Residue Terms), Related to Figure 3**

(A) Bound residue terms ('b' in Figure 3F; Table 1, 'Term I'). The sensitivity of the global fit to each model parameter was individually assessed by varying the  $\Delta\Delta G$  value across the indicated range, with the values of other parameters kept constant.  $\Delta\Delta G$  values were constrained to measured single mutant penalties (median  $\pm 0.4$  kcal/mol) or to the 95% confidence intervals of the measured median if they exceeded 0.4 kcal/mol (Figure 2E and Table S2). Vertical black lines

indicate the fit values. Asterisks indicate parameters for which the fit value was at the limit of the allowed range (see part B). The number of constructs containing each parameter in the best register (and any additional registers within 0.4 kcal/mol from the best one) is indicated. The slight offset from 0 observed for the consensus residues appears to be due to residual RNA structure (STAR Methods). As expected, the RMSE dependence was shallower for nonconsensus residues than for consensus residues due to the lower representation in the library, and the shallowness was most pronounced for the highly destabilizing 5' mutations, which were only weakly represented in the preferred binding registers.

(B) Six binding terms for which the best fit value was at the limit of the allowed range (asterisks in part A) were refit without constraints on their  $\Delta\Delta G$  value. The gray area indicates the original constraints. The solid lines indicate the original fit value, and the dashed line indicates the fit value after removing the constraints. In all cases, removing the constraints resulted in fit values within 0.2 kcal/mol of the original fit value. The small deviations could originate from small RNA structural effects or additional weak couplings.

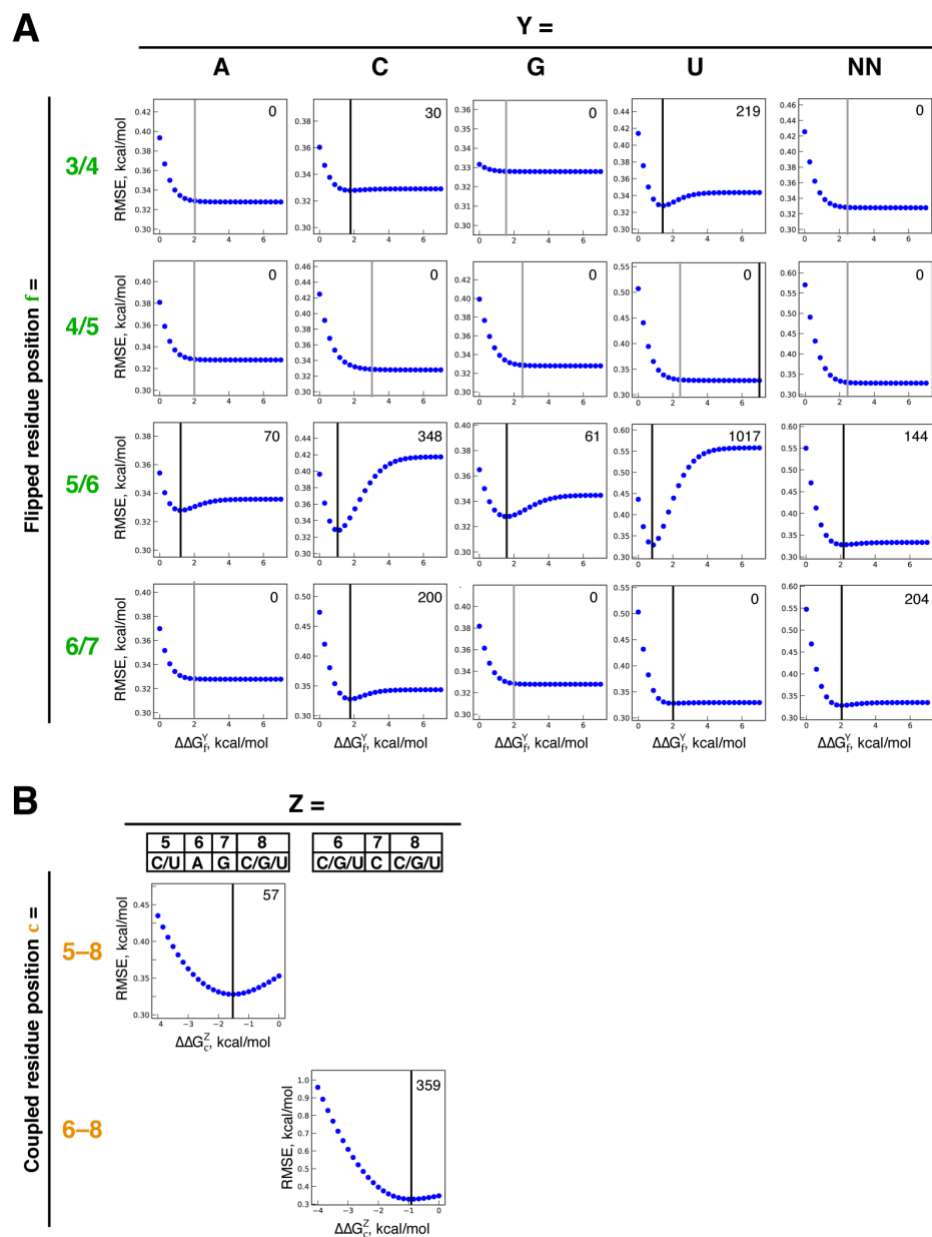


**Figure S6. RMSE Dependence on Individual Fit Parameters in the Additive Nonconsecutive Model Including Coupling (Flipping and Coupling Terms), Related to Figure 3**

(A) Flipping terms ('f' in Figure 3F; Table 1, 'Term II'). As in part A, the sensitivity of the global fit RMSE to each term was assessed by varying the  $\Delta\Delta G$  value across the indicated range, while the values of other parameters were kept constant. Black lines indicate the fit values; gray lines indicate lower limits for terms whose upper limits were undefined because these parameters were never featured in the most stable binding register (largely as a result of energetic redundancy between flipped positions). 'NN' indicates 2-nt flips of any sequence.

(B) Coupling terms. RMSE sensitivity was assessed as in parts A–C. The 8/9 coupling term is not separately shown, as its value is determined by the position 9 binding terms (A; Table 1).



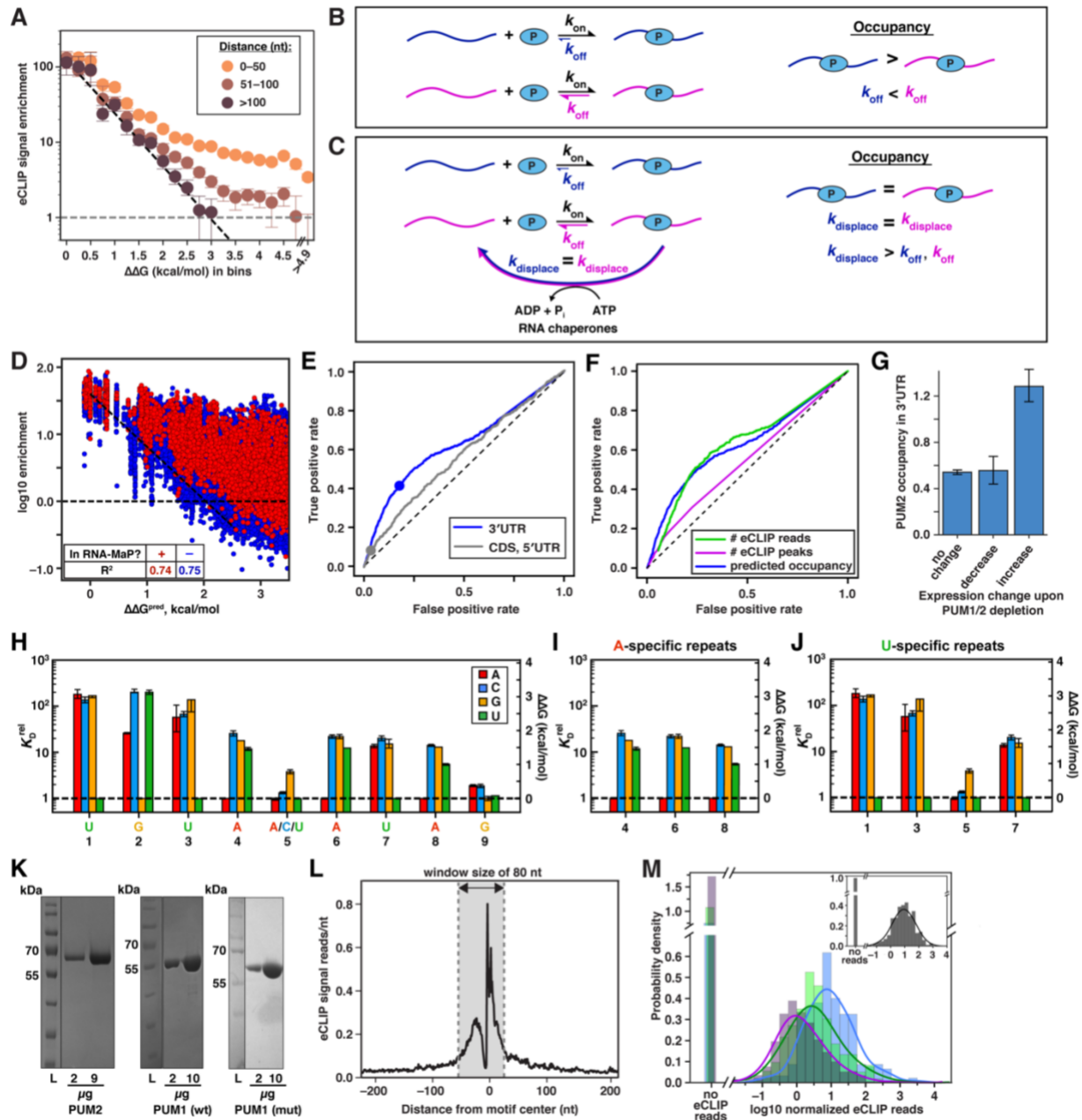


**Figure S7. Assessment of PUM2/RNA Interactions in Vivo, Related to Figure 6**

(A) Scatterplot comparing the median eCLIP enrichment across sites in bins of predicted relative affinity. Colors indicate sites with a nearby UGUA sequence within 50 nt, between 50–100 nt, or greater than 100 nt from the predicted site. The black dashed line indicates the expected change in the eCLIP signal for different predicted  $\Delta\Delta G$  values, relative to the eCLIP signal in the lowest  $\Delta\Delta G$  bin. Grey dotted line indicates expected background enrichment (=1). Error bars indicate the 95% confidence intervals on the median. Numbers of sites per bin are provided in Table S6.

(B,C) Schematic representation of models for RNA occupancy in vivo in which active RBP ('P') displacement in vivo (e.g., by ATP-dependent RNA chaperones) yields identical occupancies for targets with different affinities. (A) Equilibrium model: Two targets with different affinities are

shown, in blue and purple. The association rate constants ( $k_{on}$ ) for RBP binding to the two RNAs are identical, and the affinity difference is reflected in the greater dissociation rate constant ( $k_{off}$ ) for the second target (as is common and is observed for PUM2; data not shown). The occupancy (right) is greater for the first target due to its lower  $K_D$  value ( $K_D = k_{off}/k_{on}$ ). (B) Kinetic model: If the rate constant of active displacement ( $k_{displace}$ ) is greater than either of the intrinsic dissociation rate constants, the occupancies are equal and independent of the affinity for the RNA targets (assuming equal  $k_{on}$  values).

(D) Predicting RBNS enrichments with the thermodynamic model. RBNS enrichments of 11mer sequences from publicly available PUM1 (5 nM) and protein-free input datasets were used (Consortium, 2012; Dominguez et al., 2018), and data are shown for the 3.5 kcal/mol range within which a linear relationship between predicted affinities and RBNS enrichments was observed. Given the uneven distribution of 11mers across the predicted affinity range (Table S6), the  $R^2$  values are based on data subsampled to have the same number of randomly selected points in each 0.5 kcal/mol  $\Delta\Delta G^{pred}$  bin (see STAR Methods for details).

(E) Receiver operating characteristic (ROC) curves for classification of PUM1 and PUM2 targets based on their predicted relative occupancy in their 3'-UTR region (blue) or outside the 3' UTR (grey). True targets are defined as mRNAs that were significantly upregulated upon PUM1 and PUM2 knockdown in (Bohn et al., 2018) (see STAR Methods). Predicted targets are genes that have predicted relative PUM1 and PUM2 occupancy greater than or equal to a variable threshold. Dots correspond to the true positive and false positive rate using a threshold equal to 1 (i.e., occupancy equivalent to one consensus site).

(F) ROC curves for classification of PUM1 and PUM2 targets based on their predicted relative occupancy in the 3'-UTR region (blue) vs. PUM2 eCLIP signal across the 3' UTR (green: number of abundance-normalized eCLIP reads; magenta: number of eCLIP peaks). While eCLIP read counts and thermodynamics-based occupancies predict regulation to a similar degree, note that the number of eCLIP peaks in the 3' UTR (as defined in published eCLIP data (Consortium, 2012; Van Nostrand et al., 2016)) is not predictive of regulation.

(G) Mean predicted relative occupancies across 3' UTRs of mRNAs that are unaffected, downregulated, or upregulated upon PUM1 and PUM2 knockdown (Bohn et al., 2018). Upregulated mRNAs have significantly increased predicted PUM1 and PUM2 occupancy relative to unaffected genes ( $p = 0.001$ , Mann-Whitney U test). Error bars indicate 95% CIs of the mean.

(H) Relative affinities for bound residues 1–9 (corresponding to PUM2 repeats 'R1'–'R9') determined by global fitting to the final model (additive nonconsecutive with coupling; Table 1, 'Term I'; Figure 3F). Error bars indicate 95% confidence intervals of the median, determined by bootstrapping analysis (STAR Methods).

(I) Relative affinities of A-specific PUM2 repeats determined by global fitting.

(J) Relative affinities of PUM2 repeats with conserved U-specific residues.

(K) SDS-PAGE gels showing the purity of final purified PUM1 and PUM2 constructs. *L*: protein ladder.

(L) Average number of eCLIP read stops per nucleotide (nt) around 3,703 PUM2 consensus binding sites ( $\Delta\Delta G_{pred} < 0.5$  kcal/mol) within annotated 3' UTR, CDS, or 5' UTR regions of expressed genes in K562 cells. The grey area indicates the interval relative to the binding site over which any eCLIP read stop was included in the calculation of eCLIP enrichment (80 nt window, offset by 15 nt relative to the center of the binding site).

(M) Distribution of eCLIP signal for representative affinity bins from Figure 6A:  $-0.12$ – $0.12$  kcal/mol (blue),  $0.88$ – $1.12$  kcal/mol (green),  $1.88$ – $2.12$  kcal/mol (magenta). The eCLIP signal is the eCLIP read counts divided by transcript abundance (see STAR Methods). *Inset*: Distribution of eCLIP signal for UGUUAUAU-containing sites ( $n = 745$ ).

**Table S1.** Single mutant variants with alternative registers that have predicted affinities within 1 kcal/mol from the observed affinity, which would lower the apparent  $K_D$  by at least 20%. Related to Figure 2 and STAR Methods.

	Designed site	Shifted site	$\Delta\Delta G^{obs}$	$\Delta\Delta G^{pred}_{shifted}$	$\Delta\Delta G^{obs} - \Delta\Delta G^{pred}_{shifted}$
S1a	<u>A</u> GUAUAUA	UAUAUAUC	2.68	3.22	-0.54
S2a		UAUAUAUU	2.55	2.67	-0.12
S2b		UAUAUAUU	2.70	2.67	0.03
S1a	<u>C</u> GUAUAUA	UAUAUAUC	2.49	3.22	-0.73
S2a		UAUAUAUU	2.64	2.69	-0.03
S1a	<u>G</u> GUAUAUA	UAUAUAUC	3.29	3.22	0.07
S2a		UAUAUAUU	2.42	2.67	-0.25
S2b		UAUAUAUU	2.65	2.67	-0.02
S1a	<u>U</u> AUAUAUA	UUUAUAUA	1.70	2.64	-0.94
S1a	<u>U</u> CUAUAUA	UAUAUAUC	2.99	3.22	-0.23
S1b		UAUAUAAC	3.78	4.54	-0.75
S2a		UAUAUAUU	2.59	2.67	-0.08
S2b		UAUAUAUU	2.58	2.67	-0.09
S1a	<u>U</u> UAUAUA	UAUAUAUC	2.73	3.22	-0.49
S2a		UAUAUAUU	2.60	2.67	-0.07
S1a	UG <u>U</u> GUAUA	UGUAUAUC	1.26	1.53	-0.27
S2a		UGUAUAUU	1.16	0.97	0.19
S1a	UGUAUA <u>C</u> A	UAUACAUC	2.35	3.23	-0.88

**Table S2.** Experimentally determined single mutant penalties. Related to Figure 2.

Bound residue position b =	$\Delta\Delta G_b^X$ (kcal/mol)			
	X =			
	A	C	G	U
1	2.85*	3.11	2.64	0.00
2	1.72	3.53	0.00	2.87
3	2.45	2.75	2.41	0.00
4	0.00	2.01	0.87	1.64
5	0.08	0.05	0.81	0.00
6	0.00	1.96	1.84	1.89
7	1.48	1.64	1.41	0.00
8	0.00	1.51	1.12	0.94
9	0.08	0.52	-0.34	0.00

\* Position 1–8 values correspond to single mutant medians from Figure S3A. Position 9 values are based on measurements of randomized flanking sequences around the UGUUAUA consensus (Figure S2F)

**Table S7.** Oligonucleotide sequences. Related to STAR Methods.

	Name	Sequence (sense)
Components of the RNA array construct (see Figure S1D)	C_adapter	AATGATACGGCGACCACCGAGATCTACAC
	Read1	TCTTTCCCTACACGACGCTCTTCCGATCT
	Barcode*	NNNNNNNNNNNNNNNN
	RNAP promoter	TTTATGCTATAATTATTTTC
	RNAP start/stall sequence**	ATGTAGTAAGGAGGTTGTATGGAAGAC <u>G</u> TTCTCCTGGATCC
	Read2'	AGATCGGAAGAGCGGTTTCAGCAGGAATGCCGAGACCG
	D'_adapter	ATCTCGTATGCCGTCTTCTGCTTG
Primers used in library preparation	RNAPstall	GTAAGGAGGTTGTATGGAAGACGTTCTCCTGGATCC
	Read2	CGGCATTCTGCTGAACCGCTCTTCCGATCT
	RNAPstall_adapt	GTAAGGAGGTTGTATGGAAGACGTTCTCCTGGAT
	C_read1_bc_RNAP	AATGATACGGCGACCACCGAGATCTACACTCTTTCCCTACACGACGC TCTTCCGATCTNNNNNNNNNNNNNNNNNTTTATGCTATAATTATTTTCATG TAGTAAGGAGGTTGTATGGAAGACGTTCTCCTGGAT
	D_read2	CAAGCAGAAGACGGCATAACGAGATCGGTCTCGGCATTCTGCTGAAC CGCTCTTCCGATCT
	OligoC	AATGATACGGCGACCACCGAGATCTACAC
	OligoD	CAAGCAGAAGACGGCATAACGAGAT
DNA oligonucleotides used in RNA array preparation	Fiducial_chip***	AATGATACGGCGACCACCGAGATCTACACTCTTTCCCTACACGACGC TCTTCCGATCTCTTGGGTCCACAGGACACTCGTTGCTTTCCAGATCG GAAGAGCGGTTTCAGCAGGAATGCCGAGACCGATCTCGTATGCCGTC TTCTGCTTG
	Fiducial_flow	/5TYE563/GGAAAGCAACGAGTGTCTGTGGACCCAAG
	Fluorescent_stall'	GGATCCAGGAACGTCTTCCATACAACCTCCTTACTACAT/3AlexF647N/
	Biotin_D_Read2	/5BiosG/CAAGCAGAAGACGGCATAACGAGATCGGTCTCGGCATTCTG CTGAACCGCTCTTCCGATCT
	Dark_stall'	GGATCCAGGAACGTCTTCCATACAACCTCCTTACTACAT
	Dark_read2	CGGCATTCTGCTGAACCGCTCTTCCGATCT

\* Randomized 15mer region.

\*\* Underlined 'C' indicates the RNA polymerase stall site.

\*\*\* Corresponds to 5' – [C\_adapter] [Read1] CTT GGG TCC ACA GGA CAC TCG TTG CTT  
TCC [Read2'] [D'\_adapter].